Doctoral theses at NTNU, 2016:196

Thomas Holm

Microfluidic and high temperaturetechniques for aqueous electrochemistry

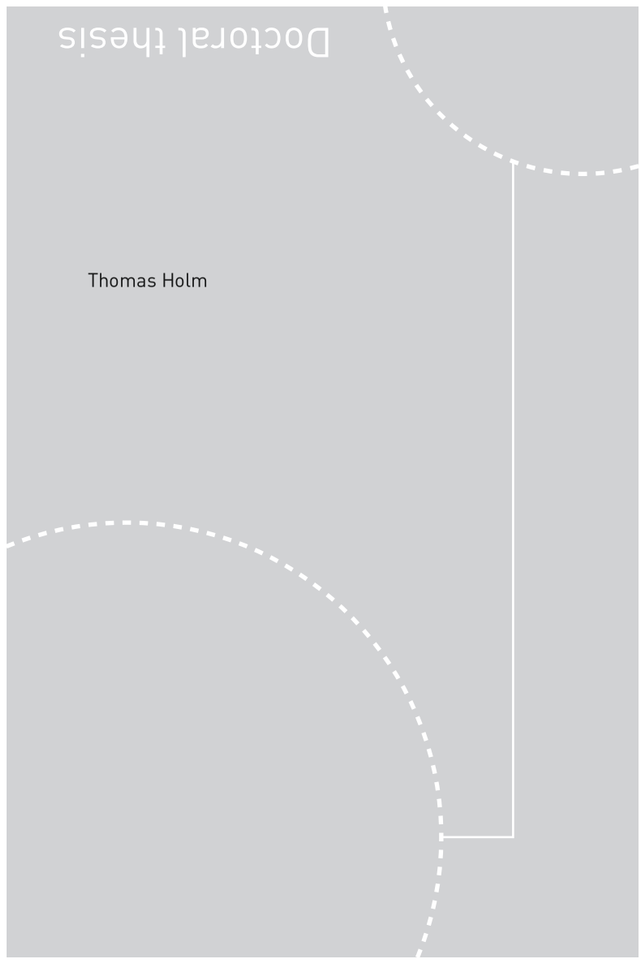

ISBN 978-82-326-1730-2 (printed ver.)
ISBN 978-82-326-1731-9 (electronic ver.)
ISSN 1503-8181

NTNU
Norwegian University of
Science and Technology

NTNU
Norwegian University of
Science and Technology
Thesis for the Degree of
Philosophiae Doctor
Faculty of Natural Sciences and Technology
Department of Materials Science and
Engineering

Doctoral theses at NTNU, 2016:196

NTNU

Thomas Holm

Microfluidic and high temperaturetechniques for aqueous electrochemistry

Thesis for the Degree of Philosophiae Doctor

Trondheim, July 2016

Norwegian University of Science and Technology
Faculty of Natural Sciences and Technology
Department of Materials Science and Engineering

NTNU
Norwegian University of
Science and Technology

NTNU
Norwegian University of Science and Technology

Thesis for the Degree of Philosophiae Doctor

Faculty of Natural Sciences and Technology
Department of Materials Science and Engineering

ISBN 978-82-326-1730-2 (printed ver.)
ISBN 978-82-326-1731-9 (electronic ver.)
ISSN 1503-8181

IMT-report 2016:229

Doctoral theses at NTNU, 2016:196

Printed by NTNU Grafisk senter

Preface

This thesis is the result of experimental and theoretical work done during my time as a PhD student at the Department of Materials Science and Engineering at the Norwegian University of Science and Technology from August 2012 to June 2016. This includes two research stays in Dr. Harrington's lab at the University of Victoria, British Columbia, Canada. The first research stay was from January 2014 to December 2014, and the second research stay was from June 2015 to February 2016.

The thesis consists of nine chapters. The first chapter consists of the background for the work done and the motivation for this work. The second chapter contains a description of the experimental methods used in this work. Chapter three contains a detailed description of the autoclave setup and the challenges related to this setup. Chapters four to eight are written as individual research papers. Two of these are published, one of these is submitted, while the remaining three are intended for publication at a later stage. Chapter nine summarizes and concludes the work of this thesis and suggests some future work in relation to the results obtained here.

My contribution in each of the six research papers are as follows:

Chapter 3, "Using a self-pressurized autoclave for aqueous electrochemical experiments": All experimental work and data analysis was performed by me. The chapter is written with input from the co-authors.

Chapter 4, "Method for studying high temperature aqueous electrochemical systems: Methanol and glycerol oxidation": All experimental work and data analysis was performed by me. The chapter is written with input from the co-authors.

Chapter 5, "Dynamic Electrochemical Impedance Spectroscopy Study of Platinum Oxidation at High Temperatures": All experimental work and data analysis was performed by me. The paper is written with input from the co-authors.

Chapter 6, "A semi-analytical method for simulating mass transport at channel electrodes": All numerical simulation done in Comsol and numerical convergence tests in Maple over a large parameter space is done by me. The development of the semi-analytical method and the implementation in Maple is done by David A. Harrington. The paper is largely written by David A. Harrington with input from me.

Chapter 7, "Mass-transport impedance at channel electrodes: accurate and approximate solutions": All experimental and modeling work was done by me. The paper is written by me with input from the co-authors.

Chapter 8, "Mass transport impedance at channel electrodes: Using a double electrode setup": All experimental work, numerical modeling and data analysis was done by me. The paper was written by me with input from the co-authors.

Acknowledgments

This thesis has been mainly financed by a faculty grant generously awarded to me during the summer of 2012 from the Faculty of Natural Sciences and Technology. In addition, financing has been obtained from the Natural Sciences and Engineering Research Council of Canada (NSERC) and University of Victoria (UVic) through the cooperation with David A. Harrington. Funds to cover travel expenses to international conferences has been provided by the Faculty of Natural Sciences and Technology. The research council of Norway is also acknowledged for the support to the Norwegian Micro and NanoFabrication Facility, NorFab (197411/V30).

Although doing the work for a PhD thesis may feel like a solitary fight to solve small and large challenges, it is never a work done by just the PhD student. I have been lucky to have excellent supervisors, co-workers, family and friends around to guide me and help me whenever needed.

Starting with my main supervisor, Frode Seland. You have been the prime reason that I got this opportunity and I am exceedingly grateful for that chance. You have filled the title of mentor excellently in all meanings of the word and a talk with you has always been a great source of confidence when I have experienced hardship during my work.

To my co-supervisor David A. Harrington. You have been been my de-facto supervisor for long periods of time during my research stays in Victoria, and I am profoundly thankful for this opportunity. You have been an excellent discussion partner that has guided me in the direction of the thesis resulting in many interesting results.

My co-supervisor Svein Sunde. You have always made time for discussions if necessary and I admire your ability to always give constructive advice whenever input is needed.

To my co-workers at NTNU and in Victoria. Espen, Mats, Gurvinder, Geer, and Jonathan, I am thankful for the company and the shared failures and successes during these years.

To the technical and administrative staff in Trondheim and in Victoria. You have been an excellent support giving help quickly whenever needed. I am especially grateful to the technicians in Trondheim, Magnus B. Følstad and Kjell Røkke, the glass blowers in Trondheim, Sebastian Bete and Astrid Salvesen, and the glass blower in Victoria, Sean Adams, for fast expedition and important input. In addition, a special thanks goes to Colin Williams for interesting non-scientific discussions lighting up those late nights in

the lab in Victoria.

To my parents, Lise and Sverre Holm. You have always supported me throughout my life and have given me a great ballast for handling challenges. You offer me an anchoring point of stability at all times if I need it.

To my brothers and your families. It has been a great support and a great way to see perspective when we have been four people doing PhDs simultaneously. You also provide a certain perspective in life when during my work at NTNU, one niece and one nephew has been added to my extended family. Thank you for all good conversations related to all aspects of life.

To my friends and extended family. Thank you all for being in my life. A special thanks to my running club, Rindal IL, for being a source of non-academic joys during all my years in Trondheim.

Last but not least, I am entirely grateful to the love of my life, my fiancée Jessica. You fill me with gratefulness and gives me new perspectives, making me a better person every day. I love you always.

"*We find after years of struggle that we do not make a trip; a trip takes us.*" - J. S.

Thomas Holm
Victoria, B.C., Canada, 8. May 2016

Summary

Liquid organic fuels are highly desired energy carriers as they have a high energy density, simple production, and can benefit directly from existing infrastructure. However, the electrochemical conversion efficiency is low due to slow kinetics. An improved understanding of the reaction mechanism is paramount to make these types of fuels a viable alternative in PEM based fuel cells. In this thesis, we have identified and developed two techniques that allowed us to expand the current knowledge. These were (1) to make a method that could study aqueous electrochemistry at temperatures above the normal boiling point of water, and (2) to find a way to make reproducible microfluidic fuel cells that ultimately can be used as an electroanalytical tool. Both of these methods can potentially be combined with spectroscopic techniques and dynamic electrochemical impedance spectroscopy (dEIS) to expand the scope of a study. Based on current knowledge of reaction kinetics, the main objectives of this thesis were:

1. Develop a robust electrochemical method to study alcohol oxidation and other processes in aqueous solutions at high temperatures.

2. Get a better understanding of the temperature dependence of alcohol oxidation by studying these processes at elevated temperatures.

3. Use dynamic electrochemical impedance spectroscopy to investigate the surface processes at the electrode.

4. Develop numerical and analytical methods for describing microfluidic channel electrodes and employ these for characterization purposes as a step on the way to utilizing microfluidic flow cells as a rotating ring-disc analog for kinetic investigations.

A method for running aqueous temperatures in a self-pressurized autoclave was developed. After solving problems related to solution resistance, seal quality, and temperature expansion, the method was successfully used to do conventional electrochemical experiments at temperatures up to 140°C in aqueous electrolytes.

The self-pressurized autoclave was used to study methanol and glycerol oxidation at platinum electrode for temperatures from room temperature up to 140°C. This allowed for efficient acquisition of kinetic parameters such as onset potentials, Tafel slopes, and activation energies. For methanol oxidation, the dissociative adsorption of either methanol or water was suggested to be the rate-determining step at the relevant potentials for fuel cells. For glycerol oxidation, an apparent change in mechanism was observed at 110°C. At temperatures below this, either dissociative water adsorption or succeeding

reaction step is suggested to be rate-determining. At temperatures above 110°C, dissociative glycerol adsorption was found to be rate-determining, suggesting that the role of water as an oxygen donor was reduced. This indicated that the glycerol reaction to glyceraldehyde was the main reaction occurring, especially at low overpotentials.

The high temperature autoclave method was used to study platinum oxidation as a function of temperature combined with dynamic electrochemical impedance spectroscopy. The oxidation mechanism was found to be similar at all temperatures, while the reduction mechanism was dependent on the thickness of the platinum oxide layer. Little temperature dependence on the fitted impedance parameters were found and it was evident that the surface oxide charge density was a more important factor than the temperature for the value of the fitted parameters.

A semi-analytical method that solved the governing convective-diffusion equation for channel electrodes was developed by using an eigenvalue method implemented in Maple. This method resulted in a semi-analytical solution by assuming that axial diffusion was negligible. This was in contrast to previous derivations assuming both axial diffusion and a linear flow regime. The semi-analytical method showed excellent results when compared to the numerical result for a larger parameter space than the analytical solutions reported in literature.

A method for making microfluidic electrochemical cells of high quality was developed. These microfluidic cells were characterized by using electrochemical impedance spectroscopy at a Pt electrode in an electrolyte with a reversible redox couple. The results were numerically modelled and the model was used to define the zones of validity of previous analytical solutions, where no axial diffusion and Lévêque approximation were assumed.

A new method for performing impedance in a two subsequent channel electrode setup using only a single potentiostat was demonstrated. This method was named downstream impedance, and it gives beautiful spirals. Through numerical modelling and normalization of the experimental data, the qualitative features of the resulting impedance were investigated and potential use of this method was discussed.

Contents

Nomenclature

Notation

Latin letters

a_i	Pre-exponential factor for eigenvalue expansion	1
A	Defined Péclet number $= 6Pe$	1
$A_{\max}$	Maximum defined Péclet number value	1
b_i	Eigenvalue number i	1
b_T	Tafel slope	V
B	Elovich parameter, surface charge constant	$\mathrm{m^2\ C^{-1}}$
B	Dimensionless geometry parameter	1
c	Concentration	$\mathrm{mol\ m^{-3}}$
$\widetilde{c}_i$	ac concentration of species i	$\mathrm{mol\ m^{-3}}$
c_s	Surface concentration	$\mathrm{mol\ m^{-3}}$
C	Non-dimensional concentration	1
C	Potential dependence constant	$\mathrm{V^{-1}}$
C_i	Non-dimensional concentration of species i	1
$\widetilde{C}$	Non-dimensional ac concentration	1
C_ad	Adsorption capacitance	$\mathrm{F\ m^{-2}}$
C_dl	Double layer capacitance	$\mathrm{F\ m^{-2}}$
C	Complex capacitance	$\mathrm{F\ m^{-2}}$
C_Re	Real complex capacitance	$\mathrm{F\ m^{-2}}$
C_Im	Imaginary complex capacitance	$\mathrm{F\ m^{-2}}$
D_i	Diffusion coefficient of species i	$\mathrm{m^2\ s^{-1}}$
E	Electrode potential	V
E_ac	ac contribution to the potential	V
E_dc	dc contribution to the potential	V
$\widetilde{E}$	ac phasor of the potential	V
$\widetilde{E}_i$	ac phasor at electrode i	V
E_onset	Onset potential	V
E^rev	Reversible electrode potential	V
E_A	Activation energy (constant electrode polarization)	$\mathrm{J\ mol^{-1}}$
$E_\mathrm{A,app}$	Apparent activation energy (constant electrode potential)	$\mathrm{J\ mol^{-1}}$
f	Frequency	Hz
f_min	Minimum frequency for the dEIS setup	Hz
f_max	Maximum frequency	Hz

F	Faraday constant	C mol^{-1}
F	F-test parameter, quantification of probability of new circuit elements	1
F	Normalized frequency parameter	m s$^{-1/6}$
$F(x)$	Non-dimensional function of parameter x	1
$G(y)$	Non-dimensional function of parameter y	1
h	Planck constant	J s
h	Channel height	m
i	Imaginary unit, $\sqrt{-1}$	1
$\widetilde{I}$	ac current signal	A
$\widetilde{I}_i$	ac current signal at electrode i	A
j	Current density	A m^{-2}
j_{ave}	Average current density	A m^{-2}
j_{rev}	Reversible portion of current	A m^{-2}
j_{tot}	Total current	A m^{-2}
J	Non-dimensional current density	1
J_{ave}	Non-dimensional average current density	1
k	Rate constant	various
k_i	Rate constant of reaction i	various
K	Non-dimensional rate constant	1
K^0	Quasi-reversible non-dimensional rate constant	1
K_i	Non-dimensional rate constant of reaction i	1
n	Popkirov coefficient, integers	1
n	Number of electrons	1
N	Collection efficiency	1
Pe	Péclet number	1
Q	Capacitive parameter in the CPE	F m^{-2} s$^{-(1-\phi)}$
Q_{dl}	Double layer CPE element	F m^{-2} s$^{-(1-\phi)}$
R	Gas constant	J K^{-1} mol^{-1}
R	Resistance	Ω m^2
R_{ct}	Charge-transfer resistance	Ω m^2
R_{s}	Solution resistance	Ω m^2
S	Non-dimensional product concentration	1
ΔS^0	Entropy	J K^{-1} mol^{-1}
$\Delta S^0_{\mathrm{SHE}}$	Entropy of the standard hydrogen electrode	J K^{-1} mol^{-1}
t	Time	s
T	Temperature	K
T_i	Temperature of component i	K
v	Reaction rate	mol m^{-2} s^{-1}
v	Velocity	m s^{-1}
v_{av}	Average velocity	m s^{-1}
$v_{\max}$	Maximum velocity	m s^{-1}

w	Electrode width	m
W	Non-dimensional electrode width	1
W_{ad}	Adsorption Warburg coefficient	F m^2 s$^{1/2}$
$x_{\max}$	Maximum length of mesh in x direction	m
z	Impedance	Ω m^2
z_{Im}	Imaginary component of the impedance	Ω m^2
z_{Re}	Real component of the impedance	Ω m^2
Z	Non-dimensional impedance	1
Z_0	Impedance coefficient	Ω m^2
Z_{dn}	Electrochemical downstream impedance	Ω m^2
Z_{Im}	Non-dimensional imaginary component of the impedance	1
Z_{Re}	Non-dimensional real component of the impedance	1

Greek letters

α	Transfer coefficient	1
β	Symmetry factor	1
β	F-test parameter, difference of parameters between circuits	1
Γ	Gamma function	1
Γ_i	Surface concentration as charge	mol m^{-2}
δ	Diffusion layer thickness	m
Δ	Non-dimensional diffusion layer thickness	1
ζ	Flow-rate normalized impedance	Ω m s$^{-1/3}$
Θ_i	Surface coverage of species i	1
λ	Non-dimensional y-component	1
ν	Potential sweep rate	V s^{-1}
ν_{new}	F-test parameter, degrees of freedom	1
π	Ratio of a circle's circumference to its diameter	1
ϕ	Coefficient for the CPE	1
ϕ	Phase change for impedance data	rad
χ	Non-dimensional x-component	1
χ^2	Chi-squared fit parameter	1
ω	Angular frequency	rad s^{-1}
Ω	Non-dimensional angular frequency	1

Abbreviations

ac	Alternating current
ADC	Analog-to-digital converter
CE	Counter electrode
CPE	Constant phase element
CV	Cyclic voltammetry
DAC	Digital-to-analog converter
DAFC	Direct alcohol fuel cell

dc	Direct current
dEIS	Dynamic electrochemical impedance spectroscopy
DEMS	Differential electrochemical mass spectrometry
DFT	Density functional theory
EIS	Electrochemical impedance spectroscopy
EQCM	Electrochemical quartz crystal microbalance
FC	Fuel cell
FFT	Fast Fourier transform
FTIR	Fourier transform infrared spectroscopy
IRE	Internal reference electrode
PDMS	Polydimethylsiloxane
PEM	Proton exchange membrane
PTFE	Polytetrafluorethylene (teflon)
RDE	Rotating disc electrode
RE	Reference electrode
RHE	Reversible hydrogen electrode
rms	Root mean square
RRDE	Rotating ring-disc electrode
SE	Sensing electrode
SHE	Standard hydrogen electrode
SIM	Small instrumental module
SRS	Stanford research systems
upd	Underpotential deposition
WE	Working electrode
XPS	X-ray photoelectron spectroscopy

1 Introduction

1.1 Background

The energy utilized today is primarily from non-renewable sources. These are by definition limited sources, and the utilization of fossil energy is known to be a contributor to climate change. Therefore, a transition from sources of non-renewable energy to sources of more sustainable energy is necessary. Several renewable energy sources are available including hydro power, geothermal power, solar power, biomass power and wind power [1]. Renewable energy sources are often intermittent and situated in remote areas and relies on conversion to energy carriers and efficient storage systems for successful integration into the modern society. Successful energy carriers should have a high volumetric energy density, cost efficient production, easy storage, distribution and conversion to useful energy like electricity. For instance, biomass derived liquid fuels possess many of these features.

For transport purposes and portable devices, the most commonly used renewable energy storage is batteries and fuels for fuel cells. Batteries often serve the purpose based on their high cyclic stability, high power density and relatively high capacity [2]. However, battery technology always suffer from the thermodynamic limit of the system which ultimately translates to either limited driving ranges or a large weight increase of the system. In light of this, fuel cells as an energy conversion system for high energy density fuels offer a viable alternative that can potentially offer both efficient energy conversion and high energy density [3]. On the other hand, real fuel cell systems often suffer from sluggish kinetics or low overall system efficiency leaving room for improvement.

Fuel cells are based on the concept of electrochemical oxidation of a fuel by separating the anode process and the cathode process and extracting electrical energy from the process. This has a great advantage over conventional combustion engine, namely that the process is not limited by Carnot's theorem. Therefore, any fuel that can spontaneously oxidize and in some way be separated in an anode and a cathode process is a potential candidate for fuel cells. This leads to a range of fuel candidates including hydrogen, methanol, ethanol, borohydride, and carbon. When treating a single fuel and comparing fuels, factors related to the reaction efficiency such as energy density, reaction kinetics, catalyst demand, and temperature response have an important influence on the system economy. In addition, each fuel has different demands when it comes to storage and handling, and when it comes to necessary affiliated systems such as compressors, humidifiers, and control systems. Therefore, all these factors must be taken into consid-

eration when analyzing a fuel cell system.

In fuel cell systems today, hydrogen is the most commonly utilized energy carrier. Hydrogen has the advantage of fast kinetics, high volumetric energy density, and a high conversion rate to the fully oxidized product, water. However, complicated and costly storage and handling of the fuel combined with low volumetric energy density and strict fuel purity demands for low temperature applications leaves potential for improvement. Therefore, liquid fuels attract interest due to the simplified handling, storage and the high energy density (both volumetric and gravimetric) [4]. However, these fuel suffer from sluggish kinetics that efficiently hinders widespread use. As the cathode processes are similar for most fuels, the understanding of the anode processes and reaction mechanism is the key to make liquid fuels more efficient and ultimately viable in commercial fuel cell systems.

1.1.1 Anode processes in fuel cells

Except for the simplest molecules, the oxidation process at the anode surface is a series of electrochemical and chemical reaction steps with very different properties. The multi-step reaction mechanisms for liquid fuels make rational catalyst design based on a good understanding of each reaction step and its kinetics and ideal condition necessary. Therefore, a general treatment and optimization of a fuel system needs to factor in the influence of several parameters, and find the separate parameter influence to the different reaction steps. Parameters like catalyst type, catalyst dispersion, catalyst surface processes, temperature, concentration of fuel and electrolyte, and pH has been shown to influence the processes in different ways [4].

For the arguably most studied liquid fuel for fuel cells, methanol, much is known about the mechanism and the influence of the named factors. Methanol is a relatively simple alcohol that ideally oxidizes fully to CO_2. It is known to yield formaldehyde and formic acid in addition to CO_2, and that at least two parallel pathways are active [5–7], meaning that there are some selectivity issues as to what pathway is dominating. Higher yield of CO_2 has been shown by increasing the temperature [8]. The oxidation reaction is more efficient in alkaline solution than in acidic solution [9], and electrolytes with less strongly adsorbed anions improve the kinetics [6]. The reaction rate is greatly influenced by the surface state of the catalyst. In particular, surface oxidation of oxide to platinum seems to increase the reaction rate until the surface is fully covered [10]. In addition, alloying the catalyst to another element can greatly influence the kinetics, where Pt-Ru being a good example of greatly enhanced kinetics [11–13].

Even though a good understanding of the methanol oxidation reaction has been obtained, still much is not known about the reaction mechanism and the details of each reaction step and their interdependent relevance. This is also evident in the relatively modest success in making methanol a viable fuel for fuel cells. Therefore, the inherent limitations to any mechanistic study means that much can be obtained by new combinations or new methods to study the oxidation mechanism. This is even more true for less well-studied fuel candidates and fuels with longer carbon chains introducing c-c bond

breaking which complicates the mechanism further. In addition, studies conducted on the more well-known systems can serve as a model for how information about more complex or less studied systems can be found.

1.1.2 Methods and strategies for mechanistic studies of anode processes

Several approaches have been applied to study oxidation of small organic molecules in order to understand the kinetics better. Differential electrochemical mass spectrometry (DEMS) has been used to successfully identify the volatile reaction products [14–16], Fourier transform infrared spectroscopy (FTIR) [17–19] and Raman spectroscopy has been used to find the adsorbed intermediates on the electrode [20], X-ray photoelectron spectroscopy (XPS) has been used to study the composition of the catalyst and the role of oxides [21, 22], electrochemical quartz crystal microbalance (EQCM) has been used to identify adsorbed species [23, 24], electrochemical impedance spectroscopy (EIS) and ac voltammetry has been used to study the adsorption processes [25–30], single-crystal and nanomaterial studies has been used to relate surface sites to oxidation activity [31–34], and studies using first-principle calculations has been used to indicate the energetically favorable reaction pathway [35]. These listed techniques give important insights into the reaction pathways and become powerful tools when combined with conventional voltammetry. However, there are limits to each technique and not all can be combined. Based on the current knowledge, some challenging areas can be highlighted: (1) methods to study temperature dependence in aqueous system above the normal boiling point of water, (2) combination of techniques so that the system can be studied in dynamic mode, and (3) the use of microfluidic flow cells as an electroanalytical tool to study reaction products.

The study of systems at high temperature is important for two reasons: (1) it studies the system at high reaction rates which are more relevant for fuel cell systems, and (2) it allows for studies of temperature dependence and subsequently the calculation of temperature dependent kinetic parameters like activation energy. In the study of liquid fuels, several temperature dependent studies [5, 7, 8, 36] but they are largely limited by the normal boiling point of water. Valuable information have been found in these studies, e.g., activation energy, product distribution, and electrode performance. Therefore, an extended study to temperatures above the normal boiling point of the electrolyte can further expand our knowledge of these systems. To obtain this, pressurization of the system is necessary, and this has been successfully demonstrated for aqueous systems studying corrosion [37], reference electrodes [38–40], pH measurements [41, 42], transport properties [43–45], and nuclear materials [46]. However, only a limited number of studies has been done on oxidation of small organic molecules using such techniques [5, 47–49].

A futher enhancement of electrochemical experiments is to combine it with a technique that allows for dynamic measurements of properties as the surface state changes. This has been demonstrated for systems of product detection like DEMS and FTIR [15, 17]. However, an expansion of the available voltammetric techniques is possible by the use of dynamic electrochemical impedance spectroscopy (dEIS) [50]. This technique allows for simultaneous measurement of impedance as conventional voltammetry

and this allows for simultaneous access to the total reaction rate (current) alongside kinetic parameters relevant to the true surface state [51]. It is a technique that is built on ac voltammetry, and has great potential since it is easily implemented in any system that allows for electrochemical experiments. Subsequently, the dEIS technique can easily be combined with spectroscopic techniques like DEMS, EQCM, and FTIR. Although being well described, the treatment of dEIS data is complicated, and a better framework for interpretation of the results is necessary to reach the full potential of the technique.

Microfluidics, using flow cells to study electrochemical reactions, has obtained an increased interest due to the increasing availability to relatively cheap production methods the last two decades. This method has been used widely in related areas such as sample preparation, separation, sensing, and fluid manipulation [52]. They offer the possibility to conduct experiments with a controlled geometry and mass-transport regime [53]. Due to the flexibility of the production method, the cells can be designed with multiple electrodes and a large variety of electrode materials. The use of multiple electrodes is a method that has potential as a method analogous to rotating ring-disc electrode [54]. This means that downstream detection of electrochemically active products have a potential application when studying many different reaction types [55]. The channel electrode setup has relevance for fuel cell systems when detection of intermediate products is important, e.g., detection of formic acid downstream during methanol oxidation can give information about the potential or temperature dependence on the selectivity of the reaction. Analysis of these systems is simplified by the widespread use of numerical and analytical software like COMSOL Multiphysics [56] and Maple [57]. The combination of numerical simulation and rigorous treatment of the governing equations offer a path for better understanding of the system combined with easier characterization of a physical microfluidic flow cell.

1.2 Motivation

In light of the many challenges making commercially viable fuel cells a real alternative to other energy carrying systems, the work done in this thesis searches to develop the tools to better understand the oxidation processes occurring in such a system. Two strategies are employed to study alcohol oxidation relevant for fuel cells; (1) A method that reliably studies electrochemical reactions at relevant temperatures and allows for combination of conventional voltammetry and dEIS, (2) an electroanalytical microfluidic technique that enhances the understanding of the anode processes.

The work of this thesis was separated into two parts treating each strategy with separate goals. Part I consists of experiments using a self-pressurized autoclave to study high temperature electrochemistry where the objectives were:

- Establish a good experimental procedure for running aqueous electrochemistry above the normal boiling point of water.
- Study methanol and glycerol oxidation at temperatures above the normal boiling

point of water at Pt electrodes.

- Apply dynamic electrochemical impedance spectroscopy to study electrochemical reactions at high temperatures.

Part II consists of experiments using a microfluidic device to study electrochemical reactions where the objectives were:

- Establish a good method for producing microfluidic devices in-house that can be efficiently used to study electrochemical reactions.
- Establish and develop methods to characterize the microfluidic devices using both dc and ac techniques through theoretical and experimental work.

1.3 Outline

This thesis is written as a collection research papers. The thesis is separated in two different parts in addition to introduction and methodology, where part I (Chapter 3-5) is about high temperature measurements of fuel or catalyst reactions. Part II (chapters 6-8) treats the microfluidic experiments and modeling done as a part of this thesis. Since each chapter is written as a separate article intended for publication, some repetition is unavoidable.

First, a brief introduction is given that connects the various chapters presented in the thesis and provides motivation and outline of the thesis. The second chapter describes methodology and all the experimental methods used as a part of this thesis.

Chapter 3 is a detailed description of the setup used in this thesis to run high temperature aqueous electrochemistry. In addition, it consists of a discussion of the problems that have been solved during the thesis work. A modified version of this chapter is intended for publication in ECS Transactions.

Chapter 4 treats high temperature experiments studying oxidation of methanol and glycerol at Pt electrodes in acidic electrolytes. Several kinetic parameters such as activation energy and Tafel slope are derived and affiliated reaction mechanisms are discussed in terms of these kinetic parameters. This work has been submitted to Electrochimica Acta.

Chapter 5 is a study of the dynamic impedance behavior of platinum electrodes in aqueous acidic electrolyte at temperatures up to 140°C. The conventional voltammetry results were used to discuss the temperature dependence of platinum oxidation. DEIS is used to find parameters such as double-layer capacitance and charge-transfer resistance. The temperature, sweep rate and potential dependence of these parameters are reported and discussed. A modified version of this chapter is intended for submission to Electrochimica Acta.

Chapter 6 is a theoretical paper that describes the steady-state mass transport at a channel electrode. This paper introduces a semi-analytical method using an eigenvalue method to derive the resulting concentration when an electrochemical reaction is run at a

channel electrode. It discusses the various assumptions done in previous literature, especially the Lévêque approximation. This work is published in Journal of Electroanalytical Chemistry [58].

Chapter 7 is an experimental work done measuring diffusional impedance at channel electrodes. This paper describes how this can be numerically simulated using COMSOL Multiphysics [59]. The various assumptions such as no axial diffusion and the Lévêque approximations are discussed by comparing the numerical solutions with existing analytical solutions. This work is published in Electrochimica Acta [60].

Chapter 8 is an experimental work describing a new way of measuring impedance called downstream impedance. This method involves performing galvanostatic impedance at an upstream electrode and detecting the frequency dependent concentration change at a downstream electrode through the potential measurements. The method and results are modeled using COMSOL Multiphysics [59], and the parameter dependencies are discussed. The results are combined with a simple qualitative model explaining the phenomena and potential application of this technique are discussed. A modified version of this chapter is intended for publication.

Chapter 9 briefly concludes the thesis and summarizes the main findings. Suggestions for future work are included in this chapter.

2 Methodology

2.1 Autoclave setup for high temperature experiments

A model of the experimental setup used for the high temperature experiments is shown in Fig. 2.1. The setup consists of a commercially available autoclave (Büchi Glas Uster AG) covered with a PTFE lid. In total, three electrodes can be used in this setup allowing for a classical three-electrode electrochemical experimental setup using a working electrode (WE), counter electrode (CE), and a reference electrode (RE). A manometer is also fitted to the system giving the ability to measure pressure. The autoclave is heated by the use of a temperature controlled oil bath. This allows for electrochemistry to be run at temperatures up to 200°C or 10 bar overpressure. In practical cases, the temperature is limited to 140°C by the total pressure in the system or the stability of the reference electrode. High temperature aqueous electrochemistry is challenging and during this work, several problems arising from the high pressure and the nature of the electrolyte were solved. A detailed description and a brief discussion of the challenges arising when conducting high temperature aqueous electrochemical experiments is given in Chapter 3.

2.2 Microfluidic Flow Cells

All the cells made and used for the experimental work in this thesis are made either by Espen V. Fanavoll or Mats Ingdal, and the summarized description is based on Mats Ingdal's procedure [61].

The microfluidic flow cells, Fig. 2.2, were made in the NorFab facilities (Trondheim, Norway). The electrodes were prepared on clean glass slabs that were cleaned in an ultrasonic bath with acetone (5 min) and isopropanol (5 min). The glass slides were dried in N_2 gas, and then cleaned by a plasma cleaner (10 min, 50% O_2, 50W, Diener Electronics Femto) and baked in an oven (10 min, 200°C). The ma-405 (Micro Resist Technology GmbH) photoresist was applied to the glass slides by using a spin coater (30 s, 1000 rpm, 250 rpm s^{-1}) and then was baked for 60 s using a hot plate (100°C). Subsequently, the photoresist was exposed to UV light (400 mJ cm^{-2}, Karl Süss MA6) and developed for approximately 150 s (ma-D331/s, Micro Resist Technology GmbH). Afterwards, the slides were rinsed in water, and cleaned by using a plasma-cleaner (10 min, 50% O_2, 50 W). An evaporator (Pfeiffer Vacuum Classic 500) was used to deposit 10 mm Ti for contact and 190 nm platinum. The excess material was removed by using

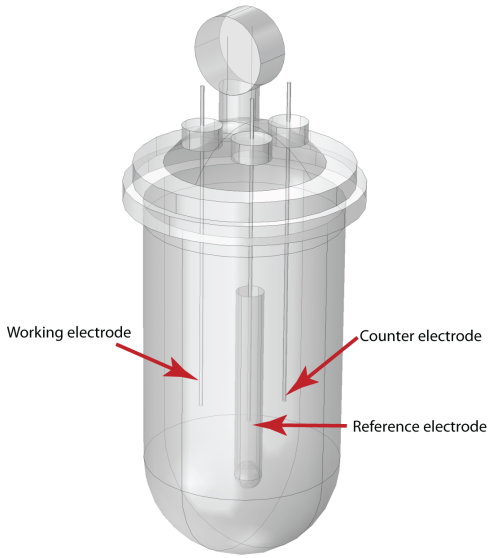

Figure 2.1: Diagram of the setup of for the autoclave experiments.

mr-REM 600 (Micro Resist Technology GmbH).

The PDMS channels were made from a channel master on a Si wafer cleaned in a similar manner to the glass slides used for the electrodes. The master was fabricated by applying photoresist SU8-2100 (MicroChem Corp.) in a two-step process by using a spin coater (10 s, 500 rpm, 100 rpm s^{-1}, then 30 s, 3000 rpm, 300 rpm s^{-1}). After spin coating, the wafer was baked on a hot plate (65°C for 5 min, then 95°C for 25 min). The photoresist was exposed to UV light (250 mJ cm^{-2}) and baked for 11 min (65°C). The photoresist was developed using Mr-DEV 600 (Micro Resist Technology GmbH) for approximately 12 min. The finished channels were baked for 15 min (150°C). The channel master was used to make the channels by mixing silicon elastomer base (25 g) and silicon elastomer curing agent (2 g) (Dow Corning S.A). The mixture was degassed for 25 min and poured on top of the channel master wafer. This was then degassed for 30 min and heat treated for 40 min (80°C). The channels were cut out with a scalpel and the holes for the inlet tube (0.5 mm diameter) and reservoir (2 mm diameter) were made by a hole punch.

The electrode slides and the PDMS channel were mounted together by activating the PDMS surface with a plasma cleaner (24 s, 100% O_2, 20 W). This was followed by a heat treatment step for 40 min (80°C). The inlet tube and the reservoir was fixed to the microfluidic cell by using silicone glue. The wires for the connection to electrochemical equipment were soldered onto the platinum electrodes. The cells produced had four 100 μm wide electrodes in a 100 μm high channel with a depth of 1 mm.

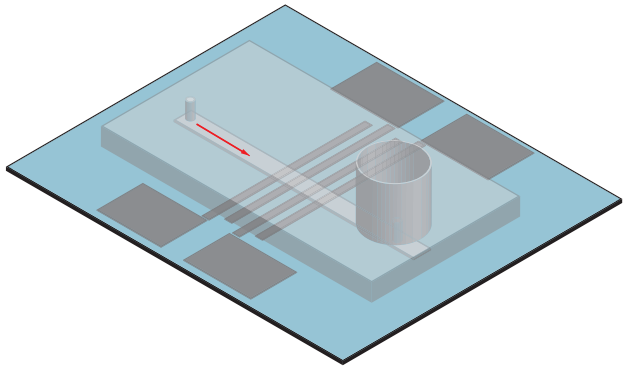

Figure 2.2: Diagram of the cell. The arrow show the direction of the fluid flow from the inlet to the collection reservoir. In total four Pt electrodes were placed perpendicular to the flow.

2.3 Electrochemical methods

The main electrochemical methods used in the work of this thesis are cyclic voltammetry (CV) and electrochemical impedance spectroscopy (EIS). In general, electrochemical methods are well-described in the literature [62–65], so only a brief description is included here.

Cyclic voltammetry is a simple technique that is useful to study the reactions occurring as a function of potential. The potential at the working electrode is controlled as in Fig. 2.3. Here, the potential starts at a start potential, E_s, is swept either upward or downward at a sweep rate, $\nu = \mathrm{d}E/\mathrm{d}t$, to an end potential, E_2, where the sweep direction is reversed and held to the other end potential, E_1. This can go on for a set number of cycles. Cyclic voltammetry is most useful as a preliminary method as it gives a quick overview of relevant potentials that electrochemical reactions occur. In this thesis, cyclic voltammetry is used in Chapter 4 and 5 as a method to find kinetic parameters, and in Chapter 8 to make sure the system has a reversible response.

Electrochemical impedance spectroscopy studies an electrochemical system by measuring the response when a small sinusoidal current or potential perturbation is applied. For the potential perturbation case, a dc potential is set until a steady response is measured. After this, potential perturbations at a given amplitude are run for a set of frequencies and the current responses at the imposed frequencies are measured. From the applied potential, $\widetilde{E}$, and the measured current response, $\widetilde{I}$, the electrochemical impedance can be calculated from Eq. (2.1).

$$Z(\omega) = \frac{\widetilde{E}(\omega)}{\widetilde{I}(\omega)} \tag{2.1}$$

The response of the system can give information about the reactions occurring and the time constants of the system. In general, there are two approaches to the analysis of

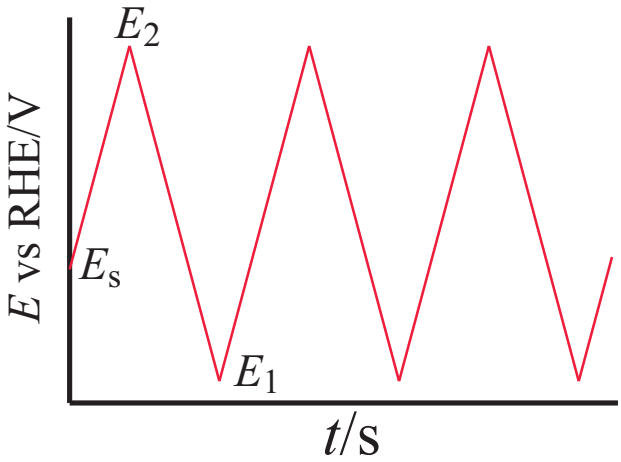

Figure 2.3: The potential vs time diagram of method of cyclic voltammetry. The cycle starts at a potential, E_s, sweeps up at a sweep rate, ν, to maximum potential, E_2, and the sweep direction is reversed and the potential is swept to minimum potential, E_1. This can be repeated for numerous cycles.

electrochemical impedance spectroscopy data. Firstly, one can fit equivalent electrical elements to the resulting response giving parameters that have a more or less equivalent electrochemical significance, this is done in Chapter 5. Secondly, one can model the full system and derive the impedance response from that. This is done for Chapters 7 and 8. The details of each method of data analysis are given in the relevant chapters as they are applied. In addition to conventional potentiostatic electrochemical impedance spectroscopy, a method that runs impedance spectroscopy simultaneously with cyclic voltammetry is used in Chapter 5. This method is described below and commonly referred to as dynamic electrochemical impedance spectroscopy (dEIS).

2.4 Dynamic Electrochemical Impedance Spectroscopy

2.4.1 Basics of the method and the setup

Dynamic Electrochemical Impedance Spectroscopy is a technique that allows EIS to be run simultaneously with a conventional dc electrochemical technique. This allows for experiments where impedance spectroscopy is used to look at processes that are underway and not at steady state as is the requirement for conventional EIS techniques. The dEIS technique is illustrated in Fig. 2.4. The technique is run so that a conventional cyclic voltammetry dc potential signal is produced by a sweep generator (Hokuto Denko HB-111) and combined with an ac signal produced digitally and converted to an analog

signal using an ADC/DAC converter (Keithley KUSB-3116). The signals were combined (SRS SIM900 Mainframe - SIM910, SIM980, and SIM983) and sent to the potentiostat (Gamry Ref. 600) and applied to the cell. The resulting current signal is collected, and the current signal, dc potential signal, and the difference between the measured potential and the input dc signal are sampled sequentially using the ADC/DAC module. The resulting dataset is the post-processed to yield the obtained impedance spectra.

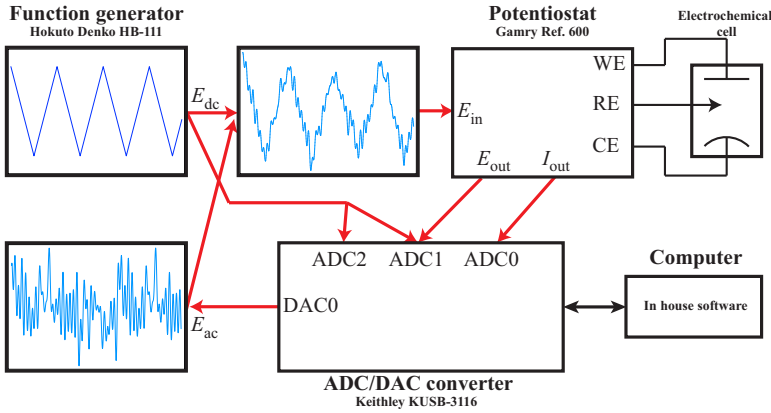

Figure 2.4: Schematics of dEIS setup. The dc and ac signals are combined in a total signal which is then sent to the potentiostat and to the cell. All red arrows indicate a process where a module in the SRS SIM900 Mainframe is involved.

2.4.2 Software and experimental parameters

The software was written in-house and handles the ac waveform generation, data acquisition, fast Fourier transformation, impedance calculation, and file management. This makes it possible to separate out each frequency through a fast Fourier transform algorithm, and hence find the impedance for each frequency. In order for the method to reliably measure the impedance of the system, several restrictions apply to the signal applied. Firstly, for a given minimum frequency, $f_{\min}$, the change of potential during one period $(1/f)$ should be limited so that the impedance response is stable. This results in a criterion for minimum frequency, and it was found for similar systems and given in Eq. (2.2) [25]. 1 Hz was used as the minimum frequency for all dEIS experiments in this thesis. The maximum frequency is limited by the sampling rate of the hardware. This gives a maximum frequency of about 50 kHz for the equipment used in this thesis.

$$\frac{F\nu}{RT} \ll 2\pi f_{\min} \tag{2.2}$$

The frequencies between the minimum and maximum frequency are set as multiples of the minimum frequency, $nf_{\min}$. The value of n were set as suggested by Popkirov and co-workers [66, 67]: 1, 3, 5, 7, 9, 11, 13, 17, 21, 25, 31, 37, 44, 52, 64, 75, 90, 100, 110,... to avoid second and third order harmonics to influence the results. In addition, the phases

of each applied frequency were randomized and the amplitudes were scaled so that an order of magnitude increase in frequency gave a factor of two decrease in amplitude. The total number of frequencies was limited to 50. The total amplitude was scaled so that it was limited to 30 mV.

Part I

High temperature aqueous electrochemistry

3 Using a self-pressurized autoclave for aqueous electrochemical experiments

THOMAS HOLM[a,b], SVEIN SUNDE[a], DAVID A. HARRINGTON[b], FRODE SELAND[a]

[a] *Department of Materials Science and Engineering, Norwegian University of Science and Technology, NO-7491 Trondheim, Norway.*

[b] *Department of Chemistry, University of Victoria, Victoria, British Columbia, V8W 3V6, Canada.*

Abstract

A detailed description of a method using a self-pressurized autoclave to run aqueous electrochemical experiments at temperatures above the normal boiling point of water is given. Relevant challenges with studying electrochemical reactions at high current densities are identified, and potential methods for solving these challenges are provided. The method can be used for aqueous electrochemistry up to 140°C using a three-electrode setup.

3.1 Introduction

The ability to perform reproducible aqueous electrochemistry at temperatures above the normal boiling point of water is an important step to increase the efficiency of processes that are slow at and around room temperature. High temperature aqueous electrochemistry has been reviewed [68–71] and allows for a study of processes at fast reaction rates and allows for derivation of temperature dependent kinetic parameter. High temperature aqueous electrochemistry has relevance for the study of corrosion [37], reference electrodes [38–40], pH measurements [41, 42], transport properties [43–45], and nuclear materials [46], while the particular method used here builds on previous work where pressurized autoclaves have been used to study alcohol oxidation [5, 47, 49].

This work discusses in detail the problems arising when attempting to increase the temperature above the normal boiling point of water. In addition, a full setup consisting of a self-pressurized autoclave is described that has been used successfully in subsequent chapters to study alcohol oxidation and the surface processes on platinum electrodes in 0.5 M sulfuric acid solution.

3.2 Experimental

A three-electrode self-pressurized autoclave system consisted of a 300 mL glass autoclave with a PTFE lid and metal tightening system (all Büchi Glas Uster AG) all shown in Fig. 3.1. This setup had four openings and this made room for three Pt electrodes and one manometer, and could be used for pressures up to 10 bar. The working electrode and counter electrode were glass sealed Pt wire electrodes, where the counter electrode had a Pt mesh welded to the wire. The reference electrode was a reversible hydrogen electrode (RHE) consisting of a platinum mesh that is inside a tube of glass and sealed at the top. This configuration for the reference electrode allowed for easy production of H_2 that can be collected in the tube and create the equilibrium between H^+ in the solution and the hydrogen gas giving the reference potential. The reference electrode was kept in a glass compartment, separating it from the main electrolyte and always kept in a solution of 0.5 M H_2SO_4.

Figure 3.1: The full autoclave setup with three electrodes and manometer.

The electrical connection to the outside of the autoclave was made possible by a twist free piano wire (K&S Engineering 54500 - 6mm). The sealing around this wire was done by a custom-made PTFE seal piece. This seal piece was fitted in a 1/4 inch connection (full set in Nickel-Copper Monel from Swagelok: M-400-1-4). PTFE heat-shrinkable tubing was used to keep the electrode wires separate from the electrolyte. The whole arrangement for one electrode consisted of various parts as displayed in Fig. 3.2.

The heating of the system was done by a hot plate (Torrey Pines Scientific HP61A or IKA C-MAG HP10), and a heating oil handling temperatures up to 210°C was used (Dow

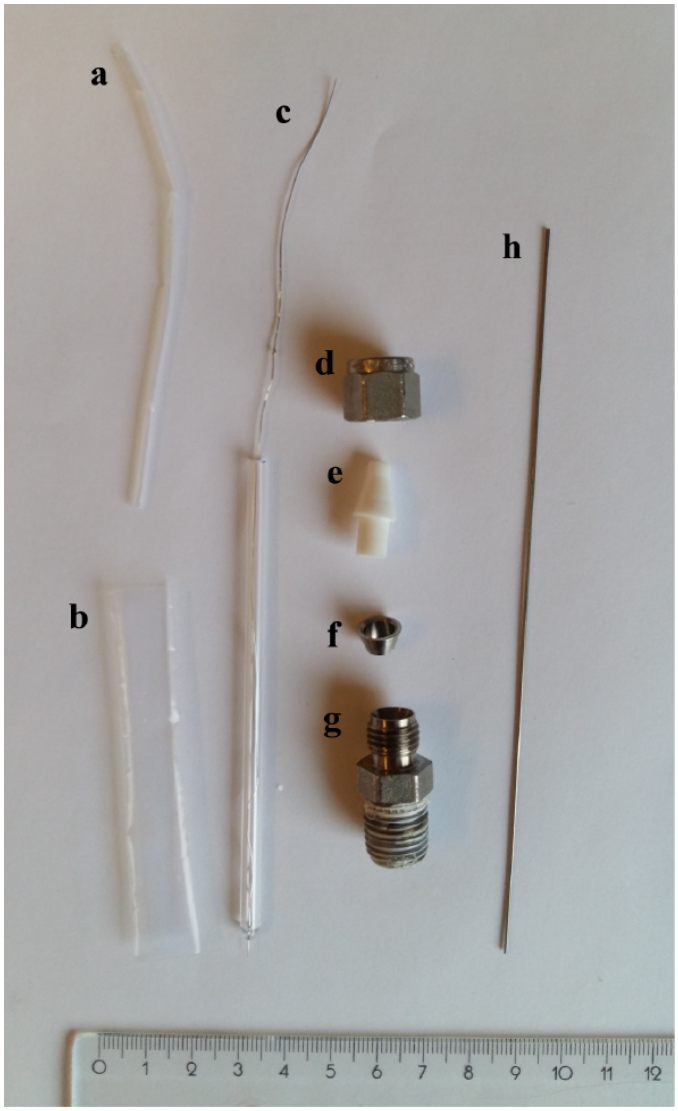

Figure 3.2: An example of the parts making up a full electrode that can be sealed off. The parts are PTFE heat-shrinkable tubing a) 3.2 mm - 1 mm and b) 9.5 mm - 2.4 mm, c) the electrode with platinum wire sealed in 4 mm outer diameter glass, d) top nut, e) PTFE wire seal piece, f) sealing cone, g) bottom nut, and h) twist free piano wire for a proper seal.

Corning 210H Fluid). The system was calibrated before runs because the temperature could only be measured in the oil during experiments. This was done by heating the setup at intervals with the same amount of deionized water (Millipore Milli-Q) as electrolyte in later experiments and recording the temperature in the electrolyte by using a thermometer that was fitted to the connections used (VWR Traceable Dual-Channel Thermometer no 23609-230).

3.3 Results and discussion

3.3.1 Effect of sealing quality

To pressurize an autoclave, it is obvious that a good seal is necessary to obtain a high pressure. However, a poor seal quality can be detrimental to the response over time, as evaporation of the active component can lead to a decline in the response. In particular, this is a problem when using an active component with a higher partial pressure than water at high temperatures. An example of this is methanol, which in pure form has a normal boiling point of 64.7°C, and a partial pressure at 100°C of 3.4 bar. This leads to a selective loss of the electrochemically most active part of the electrolyte and gives a poor result. An example of loss of methanol is shown in Fig. 3.3 where the activity is reduced by about 90% over the duration of the experiment (223 min).

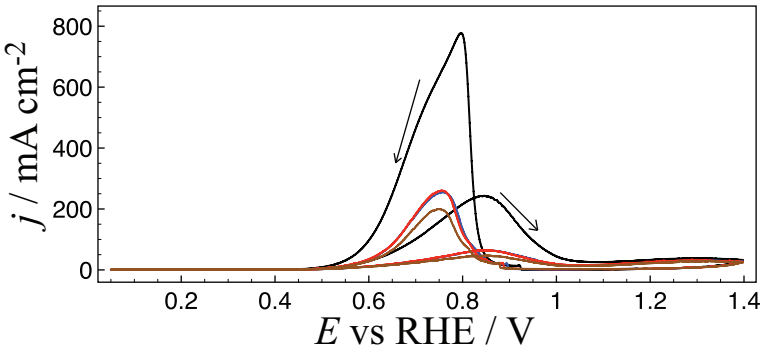

Figure 3.3: A decline in current density over time due to evaporation of methanol from the solution. All cyclic voltammograms are measured using the same setup at different times; t = 0 min (black), t = 180 min (blue), t = 202 min (red), and t = 223 min (brown).

Quantification of the actual loss is not straightforward, so experiments of similar quality as displayed in Fig. 3.3 have not utilized for any analysis. This problem was solved by using the electrode setup in Fig. 3.2, where the key step involved has been to replace the easily dented Pt wired connection through the seal piece with a straight, strong and electrically conducting wire (Fig. 3.2h). This strong wire combined with the PTFE seal piece allowed for an excellent seal of the 1/4 inch connection (Fig. 3.2d,g). This arrangement ensured efficient operation up to 150°C with a stable internal pressure

without notable loss of electrolyte.

3.3.2 Ohmic resistance effects

Ohmic resistance is an important parameter in all electrochemical setups and should normally be found and compensated for. This effect is related to the potential drop due the ohmic resistance between the working electrode and the reference electrode. On the other hand, in high temperature experiments we observed ohmic resistance that could not be compensated as this was related to the actual potential drop between the working electrode and the counter electrode. This will only matter at very high currents and thus when the electrodes are too large. The effect is seen in Fig. 3.4, where (a) has a small electrode size and a reasonable result, while (b) has a large electrode (3 cm^2 [72]). The larger electrode leads to a linearized current response due to the total current between the working and the counter electrode will reach the limit of the electrolyte. Similar behaviour was observed by Umeda et al. [73] and Bokach et al. [48] studying organic fuel oxidation in acidic electrolyte at Pt catalysts at elevated temperatures and high concentrations of organic fuel. It is likely that the high area of the catalyst electrodes leads to erroneous voltammetric responses. This is hinted at by Bokach et al. who also performed experiments with low concentration of methanol, resembling the familiar voltammogram expected for methanol at Pt electrodes.

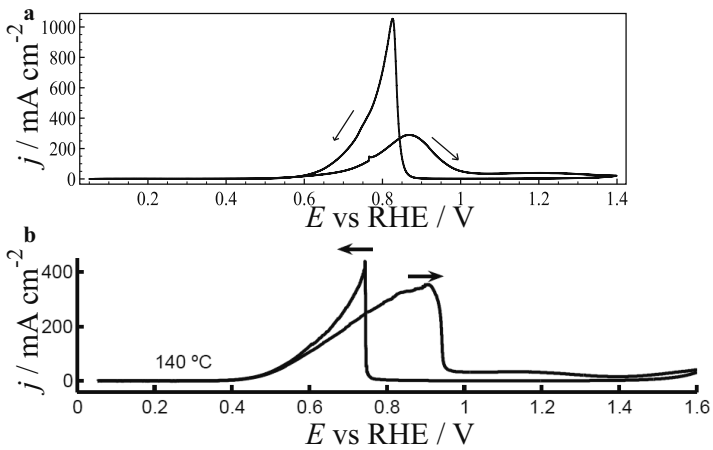

Figure 3.4: Example of a (a) small electrode (0.005 cm^2) and a (b) large electrode (3 cm^2) performing cyclic voltammetry at low sweep rates (a - 20 mV s^{-1} and b - 10 mV s^{-1}) at 140°C. The linear slope visible when using the large electrode is a consequence alluded to be primarily caused by the to electrolyte resistance. The data for the large electrode is adopted from a previous work on the autoclave [72]. Note the different current scale.

Fig. 3.4 illustrates the solution to the problem of large ohmic resistances. That is simply to use a relatively small electrode. While a definite criteria for a good experimen-

tal setup is not found, it is a good indicator that high temperature peaks should be have a similar shape as room temperature peaks and that the linear current vs potential plots are a good indicator that ohmic resistance or too large working electrode area may cause a problem. Naturally, this is only a problem for very high currents. Therefore, it is dependent on the system studied and what kind of currents that are expected. Therefore, the general rule of thumb is to use as small electrode as possible provided the small currents can be measured without too much noise.

3.3.3 Stability of the elecrochemically active area

A small electrode is an advantage in electrochemical experiments. However, temperature change can influence the electrode size in ways not intended. For an electrode that is polished as a disc sealed in glass, the large contact area of platinum towards glass in relation to platinum to electrolyte can be problematic. Obtaining a good seal between a Pt wire and glass is essential in minimizing the electrode area. However, this is not straightforwardly achieved as the molecular interactions are weak and the thermal expansion coefficients do not scale with each others. Ultimately, repeated heating and cooling of the seal will lead to an incomplete seal through formation and propagation of small cracks where electrolyte potentially can intrude and effectively change the active working electrode area. This effect was observed for a 10 μm diameter commercially obtained microelectrode (BASi MF-2005) as shown in Fig. 3.5. After the electrode had been heated to 140°C (blue) and 160°C (black), the electrode was much larger than the electrode as new (red). This was determined from the area of the hydrogen adsorption peaks during cyclic voltammetry in 0.5 M H_2SO_4 at room temperature. Such an increase in electrochemically active area is detrimental in the study of temperature effects of electrochemical reactions.

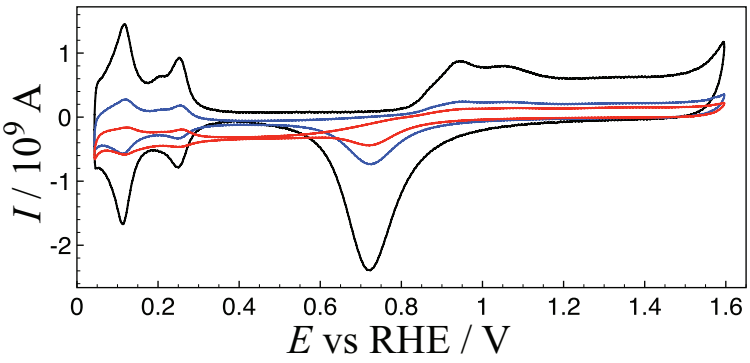

Figure 3.5: Example of electrode growth when using a 10 μm microelectrode. Room temperature cyclic voltammetry at the first cycle (red), room temperature cyclic voltammetry after the first heating cycle (blue) (max. temp 140°C), and room temperature cyclic voltammetry after the second heating cycle (black) are shown (max. temp 160°C). Sweep rates are at 100 mV s^{-1}.

In addition to a larger active electrode area resulting of electrolyte intrusion in small gaps between the electrode and the seal material, the possibility of accumulating product gas within the cracks is also plausible. Such an effect was consistently seen for electrodes with an increased working electrode area, in particular during the negative-going sweep at the onset of platinum reduction as shown in Fig. 3.6. This effect led to a large increase in the current that quickly descended to trace a current perhaps resulting merely from the electrode area confined to the outside of the sealed area, i.e. the flat grinded original area.

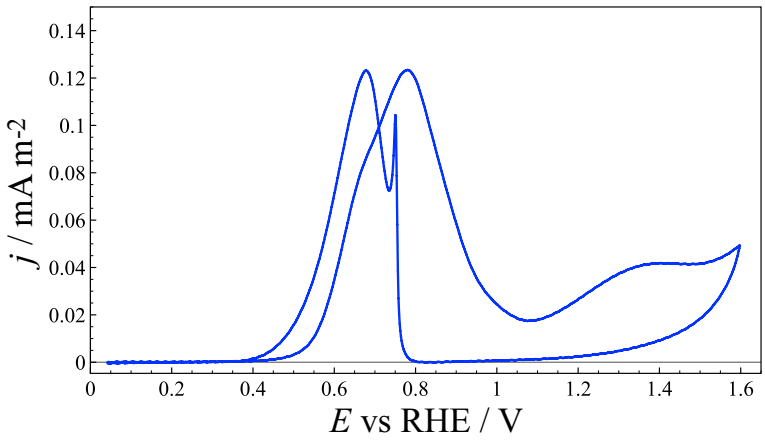

Figure 3.6: Example of downward sweep giving an extra peak due to poor seal between platinum and glass. Sweep rate is 1000 mV s^{-1} and temperature is 120°C.

Both problems associated to higher temperatures yielding an increased electrochemically active area and that the cracks give artifacts in the cyclic voltammogram can be solved by adjusting the working electrode geometry. More specifically, the problem is reduced by using a wire electrode where the fraction of the area associated with the seal is minimized, i.e., by using an electrode with greatly increased length/diameter ratio. Therefore, the design of any high temperature experiment should incorporate all effects related to the electrode size meaning that the electrode size should be minimized while most of the electrochemically active area should be associated with the surface of a wire and not be greatly influenced by any cracking in the platinum-glass seal. A satisfying compromise was done in this work by employing a 0.05 mm diameter Pt wire (VWR 99.95%) and allowing for 3-5 mm of the Pt wire to be kept outside the seal, allowing for a high length/diameter ratio minimizing seal effects in the experiments with the highest current densities.

3.3.4 Reference electrode stability

As the reference electrode is inside the autoclave, the potential is influenced by the temperature change. However, to keep the change predictable, the partial pressure of hydrogen must be kept constant at each temperature. If this criteria is not met, a drift in

the reference electrode potential can be observed. Therefore, the autoclave heat gradients should be minimized, and this translates to a low heating rate. From experience in operating the system, a heating rate of less than 20 K hr^{-1} is recommended.

3.4 Conclusion

A successful setup and experimental procedure was established for conducting high temperature aqueous electrochemical experiments. Specific challenges associated to ohmic resistance, working electrode area stability and reference electrode stability are discussed. A compromise using a thin Pt wire with a high length/thickness ratio for high current measurements, and slow heating/cooling rate are recommended for optimum operation. The full setup described was used in Chapters 4-5.

4 Method for studying high temperature aqueous electrochemical systems: Methanol and glycerol oxidation

THOMAS HOLM[a,b], PER KRISTIAN DAHLSTRØM[a,b], ODNE S. BURHEIM[c], SVEIN SUNDE[a], DAVID A. HARRINGTON[b], FRODE SELAND[a]

[a] *Department of Materials Science and Engineering, Norwegian University of Science and Technology, NO-7491 Trondheim, Norway.*
[b] *Department of Chemistry, University of Victoria, Victoria, British Columbia, V8W 3V6, Canada.*
[c] *Department of Electrical Engineering and Renewable Energy, Norwegian University of Science and Technology, NO-7491 Trondheim, Norway.*

Manuscript submitted to Electrochimica Acta

Abstract

A method for high purity aqueous electrochemical experiments at temperatures above the normal boiling point of water and at temperatures up to 140°C is described, and used to study platinum surface oxidation, methanol oxidation, and glycerol oxidation at polycrystalline platinum electrodes. A three-electrode cell in a self-pressurized glass autoclave is heated in an oil bath. Slow ramping of the temperature allows efficient acquisition of kinetic parameters such as activation energies, oxidation onset potentials and Tafel slopes by using cyclic voltammetry. For methanol oxidation on polycrystalline platinum, the dissociative adsorption of water or the dissociative adsorption of methanol is the rate-determining step at low overpotentials. Glycerol oxidation on polycrystalline platinum is rate-determined by dissociative adsorption of water or dissociative adsorption of glycerol at temperatures below 110°C. At higher temperatures, there is a dramatic decrease in overpotential, and the reaction is suggested to selectively oxidize to glyceraldehyde, with dissociative glycerol adsorption as the rate-determining step.

4.1 Introduction

Use of direct alcohol fuel cells (DAFC) offers an attractive alternative to the full implementation of the hydrogen economy [74]. The use of liquid organic fuels simplifies the infrastructure demands, and most of these fuels are available at industrial scales. However, organic fuels suffer from sluggish kinetics, complex reaction pathways, electrode

poisoning, and fuel crossover in the membrane. These cells usually operate at elevated temperatures to improve the kinetics, influence the bonding of reaction intermediates [75–79], alter the reaction products [8], simplify the water management [80], and improve waste heat recovery efficiency. However, higher temperatures may degrade the membrane, catalyst support and gas diffusion electrode [81, 82]or cause humidification problems [83, 84].

Understanding the reaction mechanism at the operating temperature is essential to improvement of the kinetics, but most kinetic studies have been at lower temperatures. Measurement over a wide range of temperatures enables activation energies to be obtained. In this work, we demonstrate that a self-pressurized autoclave can study alcohol oxidations at temperatures up to 140°C under the high-purity conditions needed to get quality kinetic data at noble-metal electrodes. This system has the advantage that aqueous electrochemistry can be run at temperatures above the normal boiling point of water. High temperature aqueous electrochemistry has been reviewed [68, 69], and has been used for decades to study corrosion [37], reference electrodes [38–40], pH measurements [41, 42], transport properties [43–45], and nuclear materials [46]. The method used builds on previous methods using pressurized autoclaves to study alcohol oxidation [5, 47–49], but this is the only work known to the authors that facilitates fast acquisition of kinetic properties at several temperatures.

Two alcohols with distinctly different properties and kinetics, methanol and glycerol, were chosen to demonstrate the method. These fuels have a high volumetric energy density, 4.3 and 6.3 kWh L^{-1}, compared to compressed hydrogen at 700 bar which has a volumetric energy density 1.3 kWh L^{-1}. Methanol is a single-carbon molecule that is widely studied as a potential DAFC fuel candidate. The reaction mechanism of methanol oxidation has been established [7], and it is a simple molecule with the potential for high CO_2 yield. However, it is volatile and has high vapor pressures above its normal boiling point at 64.7°C, which complicates high temperature operation with liquid reactants. Glycerol is a three-carbon alcohol molecule that has attracted increasing interest as a potential fuel candidate in the last decade. This interest has arisen due to glycerol being readily available at low cost, as it is a byproduct of biodiesel production [85]. Glycerol has the advantage of a low vapor pressure below its normal boiling point of 290°C. However, complete electrooxidation of glycerol to CO_2 demands carbon-carbon bond breaking, resulting in low yields of CO_2 at room temperature on polycrystalline Pt [16].

Below, we present kinetic data for oxidation of methanol and glycerol at Pt in sulfuric acid electrolyte up to 140°C. The kinetic parameters determined include onset potentials, E_{onset}, Tafel slopes, b_T, and activation energies, E_{A}, as determined from cyclic voltammetry.

4.2 Experimental

The pressurized system consisted of a 300 mL glass autoclave with a PTFE lid (Büchi AG), Fig. 4.1. Wire electrodes were sealed in glass and a custom PTFE connection with

a hole for the wire was made to fit into the 1/4 inch Swagelok fittings. The reference electrode (within the cell) was a reversible hydrogen electrode (RHE) with a small tube where hydrogen gas could be produced and collected to equilibrate at a Pt wire. All potentials are referred to this reference electrode unless otherwise specified. The counter electrode was a Pt mesh spot-welded to a Pt wire sealed in glass. The working electrode was a Pt wire electrode sealed in glass. The area of the working electrode was 0.08 cm^2 for the fuel-free, 0.05 cm^2 glycerol oxidation experiments, and 0.005 cm^2 for the methanol experiments. The much higher current densities for methanol oxidation made it necessary to use a smaller electrode to reduce the effect of solution resistances.

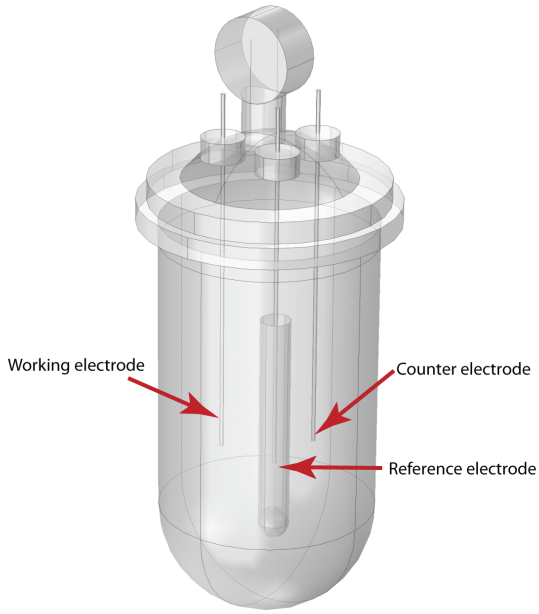

Figure 4.1: Cell setup for the autoclave.

The glassware and electrodes were cleaned in hot sulfuric acid before each run and rinsed at least twice in high purity water (Millipore Milli-Q). The autoclave was filled with 200 mL of electrolyte containing the alcohol, sealed off, and put in a temperature controlled oil bath. This setup allowed for a maximum temperature of 160°C and 10 bar gauge pressure. Due to the corrosive nature of the electrolyte and the limited number of inputs to the autoclave, the temperature was controlled and measured in the oil bath. Therefore, the relationship between the electrolyte temperature and the oil bath temperature was determined in a calibration run using 200 mL of high purity water.

The supporting electrolyte was 0.5 M sulfuric acid (Seastar Chemicals Baseline 93 - 98%). The alcohol oxidation experiments used 1 M solutions of methanol (Acros electronic use grade 99.8%) or glycerol (Anachemia ACS grade 99.5%) in the supporting

electrolyte. A Gamry Ref. 600 potentiostat was used. The electrodes were electrochemically cycled between 0.05 and 1.4 V for 100 scans at 200 mV s^{-1} prior to the heating experiments. A series of experiments at different temperatures was conducted in a single session while ramping the temperature in the oil bath at 10 K hr^{-1}. A series of cyclic voltammograms between 0.05 and 1.4 V run at sweep rates between 20 mV s^{-1} and 1000 mV s^{-1} started every 30 min and lasted less than 10 min. In addition, potentiostatic electrochemical impedance spectroscopy was used to estimate the solution resistance, which was found to be small at all temperatures and was neglected in the analysis. In summary, a series of experiments acquired the data at 5 K intervals, with a temperature uncertainty of ± 2 K. The current densities were calculated on an electrochemically-active surface area basis by assuming the charge of the hydrogen adsorption peaks between 0.4 and 0.07 V was 220 μC cm^{-2}.

The metal-solution potential difference at the RHE changes with temperature, and so measurements of the apparent activation energy, $E_{\mathrm{A,app}}$, at a fixed potential vs RHE are not determined only by the working electrode reaction. They were corrected to represent the activation energy for constant working-electrode metal-solution potential difference, E_A, according to the method of Protsenko and Danilov [86], Eq. (4.1).

$$E_{\mathrm{A}} = E_{\mathrm{A,app}} - \alpha F T \frac{dE_{\mathrm{RHE}}}{dT} \tag{4.1}$$

For the correction term, α was assumed to be 0.5, T was the average temperature of the temperatures used for the regression, and dE_{RHE}/dT was estimated as $\Delta S^{\mathrm{o}}_{\mathrm{SHE}}/F = 0.87$ mV K^{-1} [87], where ΔS^{o} is for the reaction $\mathrm{H^+ + e^- \rightleftharpoons \frac{1}{2}H_2}$. The smaller temperature dependence of the activity part of the Nernst equation at the RHE has been neglected.

4.3 Results and discussion

4.3.1 Platinum surface processes at high temperatures

Fig. 4.2a-c compare the cyclic voltammograms at 80°C without alcohol, with methanol, and with glycerol. The platinum voltammogram in sulfuric acid, Fig. 4.2a, shows the well-known regions for underpotential deposition (upd) of hydrogen (0.05 V - 0.3 V), double-layer charging (0.3 V - 0.8 V), and platinum oxide formation and reduction (0.8 V - 1.4 V) [88]. The addition of methanol or glycerol, Fig. 4.2a-b, gives a large increase in current and the alcohol oxidation processes dominate the total reactions. However, the influence of the platinum oxide formation is seen in the large drop in current at potentials higher than 0.9 V even though the overpotential for alcohol oxidation is steadily increasing. The current increases sharply again during the negative-going sweep direction as the platinum oxide is reduced and exposes active Pt sites for alcohol oxidation.

When the temperature is increased for platinum in sulfuric acid, it mainly influences the platinum oxide formation and reduction processes, Fig. 4.3, as observed before over a lower temperature range [36]. Although the extent of Pt oxidation increases at higher

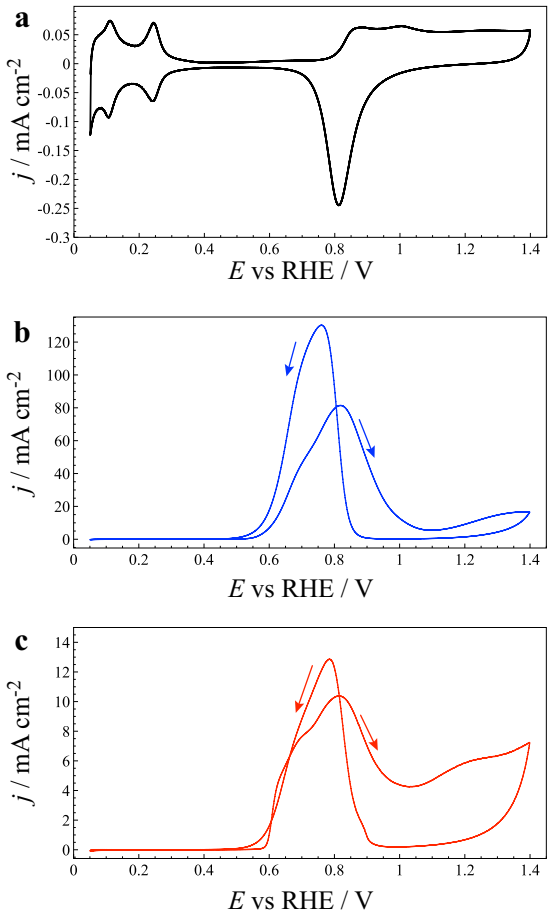

Figure 4.2: Cyclic voltammogram for platinum in 0.5 M H_2SO_4 only (a), solution containing 1 M methanol (b - blue), and solution containing 1 M glycerol (c - red). Scan rate is 50 mV s^{-1} and temperature is 80°C. Note the different scales for the current density.

temperatures, the onset potential change is small and between 0.81 and 0.85 V for all temperatures. Therefore, the platinum oxide should have little influence on the alcohol oxidation reaction at potentials relevant for fuel cells, i.e., below 0.7 V. However, the temperature may influence processes such as anion adsorption and water adsorption without a visible influence on the voltammograms. These processes may influence the alcohol oxidation activity.

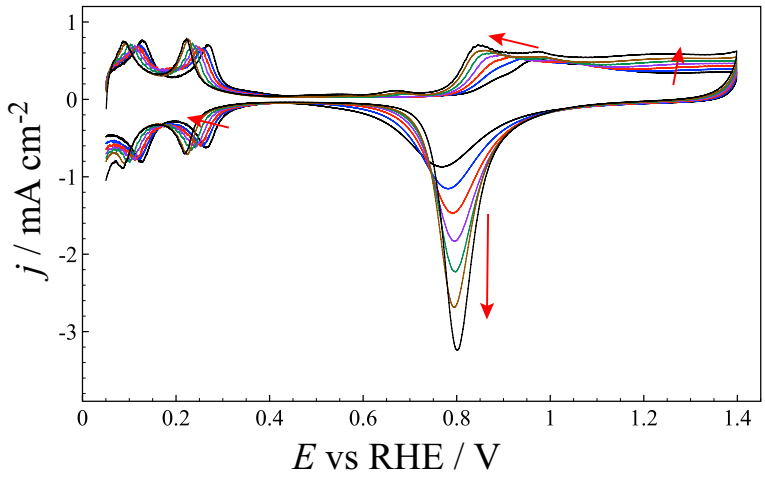

Figure 4.3: Temperature dependence of Pt cyclic voltammograms in sulfuric acid. Scan rate is 500 mV s^{-1}. Temperatures are 25°C (black small current), 40°C (blue), 60°C (red), 80°C (purple), 100°C (green), 120°C (brown), and 140°C (black large current). Red arrows indicate the trend as temperature is increased.

4.3.2 Temperature dependence of methanol oxidation

In the presence of methanol, large anodic currents arise as seen in Fig. 4.2b. The complete oxidation of methanol to CO_2, Eq. (4.2), has a standard potential of 0.016 V vs SHE. However, as seen in the voltammogram in Fig. 4.2b, the methanol oxidation reaction rate is insignificant until about 0.6 V.

$$CH_3OH + H_2O \rightarrow CO_2 + 6H^+ + 6e^- \tag{4.2}$$

The reaction mechanism of methanol oxidation has been reviewed [6, 7, 89, 90]. A suggested pathway for producing CO_2 is given in Eqs. (4.3)-(4.6), and involves reactions such as dissociative adsorption of methanol (Eq. (4.3)) and water (Eq. (4.5)), oxidation of methanol to adsorbed CO (Eq. (4.3)-(4.4)), surface reaction between adsorbed molecules (Eq. (4.6)), diffusion of the reactants and products in the solution, and surface diffusion of the adsorbed species. A second "direct" pathway also occurs, which does not involve adsorbed CO as an intermediate [6, 89, 91]. In addition, at room temperature only about 40% of the total current goes toward CO_2 production [8, 92], and products

such as formaldehyde and formic acid are found [8, 93–95]. Accordingly, the sequence of reactions presented is a very simple picture of the actual mechanism.

$$CH_3OH \leftrightarrows CH_2OH(ads) + H^+ + e^- \tag{4.3}$$

$$CH_2OH(ads) \leftrightarrows CO(ads) + 3H^+ + 3e^- \tag{4.4}$$

$$H_2O \leftrightarrows OH(ads) + H^+ + e^- \tag{4.5}$$

$$CO(ads) + OH(ads) \rightarrow CO_2 + H^+ + e^- \tag{4.6}$$

The large overpotentials suggests that the surface is either blocked by a strongly adsorbed species or is kinetically not favorable for one or more of the reactions in Eqs. (4.3)-(4.6). The reaction is not mass-transport controlled at these concentrations [96, 97]. At potentials below 0.6 V, IR studies show that the surface is largely covered by CO [98]. However, steady-state experiments indicates that the maximum surface is only about 70% of a monolayer [99, 100], which arises because dehydrogenation of methanol to adsorbed CO requires three adjacent Pt sites [101, 102]. Therefore, the surface is not blocked by a compact CO layer indicating that sites are still available for dissociative water adsorption, and the reaction of CO further to CO_2 (Eq. (4.6)), or the dissociative adsorption of water onto the surface (Eq. (4.5)) has to be the rate-determining step. An observed drop in overpotential when platinum is alloyed with a metal more active towards water adsorption supports this assumption [12, 103], and DFT calculations suggest that dissociative water adsorption to OH is favorable above about 0.6 V vs SHE at room temperature on Pt(111) [104–107].

Although the potential-dependent adsorption of water (Eq. (4.5)) is rate-determining at low potentials, its rate increases into the peak starting at 0.6 V until another step becomes rate determining. The surface coverage of CO at room temperature drops when the potential increases [108], indicating that the reaction is not dependent on adsorbed OH. IR studies at these potentials have found a large presence of formate (HCHO) at the surface indicating that either an earlier step in the CO_2-producing mechanism or one of the mechanisms producing formaldehyde or formic acid is dominating [92]. The rise in current density is halted at 0.85 V due to the Pt oxide formation as discussed in Section 4.3.1. The drop in current density ends at 1.0 V, where it is known that the whole surface is covered with platinum oxide [88]. The oxidized platinum surface results in low current densities until the oxide is reduced again. This oxide reduction starts at 0.9 V in the negative-going sweep, and initiates the large activity increase of methanol oxidation during the cathodic scan. The reaction then proceeds until the surface is largely covered with CO again, and water adsorption is again rate limiting.

An increase in temperature was found to increase the yield of CO_2 during methanol oxidation, greatly simplifying the reaction mechanism [8]. The voltammgrams show a thousandfold increase in current density from 21°C to 140°C, Fig. 4.4a-c. Even though the increase in current density is large, the basic features in the voltammograms remain similar for all temperatures. There is a very low current until the onset of the oxidation,

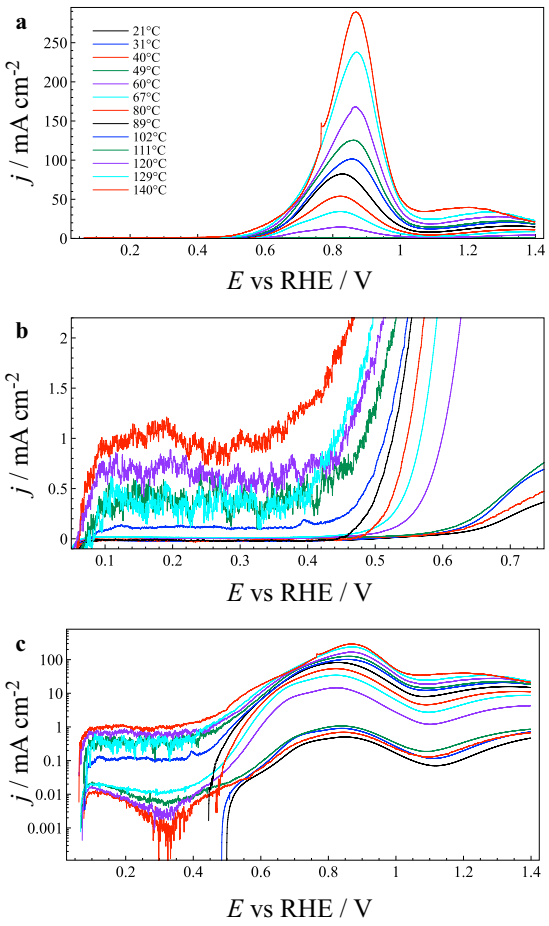

Figure 4.4: Temperature dependence of methanol oxidation. Only the anodic scan direction of the voltammograms is shown. Scan rate 20 mV s^{-1}. (a) Full scale cyclic voltammograms, (b) expanded scale cyclic voltammogram highlighting the onset potentials, (c) logarithmic plots of current vs potential highlighting the Tafel slopes.

highlighted in Fig. 4.4b. An increase in temperature clearly influences the onset potentials and Tafel slopes, and it allows for the determination of activation energies, these are discussed in Section 4.3.4.

4.3.3 Temperature dependence of glycerol oxidation

In the case of glycerol oxidation, in Fig. 4.2c, the voltammogram has many of the same features as for methanol oxidation in Fig. 4.2b, indicating that many of the same processes determine the measured current. There is little current until 0.6 V in the positive-going sweep, then a peak with a shoulder from 0.6 V to about 1 V, and then a drop in current to a plateau that persists until the reversal potential at 1.4 V. During the negative-going sweep, there is little current until 0.9 V where a large oxidation peak is visible before the current drops to zero at about 0.5 V. Complete oxidation of glycerol to CO_2 is a 14-electron process, shown in Eq. (4.7).

$$C_3H_5(OH)_3 + 3H_2O \rightarrow 3CO_2 + 14H^+ + 14e^- \tag{4.7}$$

However, oxidation of glycerol has been shown to yield various other products including tartronic acid, gluconic acid, glyoxylic acid, formic acid, carbon monoxide, glyceraldehyde and glyceric acid [16, 109, 110]. The large variety of products is due to the difficulty of breaking carbon-carbon bonds, and factors such as crystal orientation [111], reactant concentration [112], support material [113], and pH [16, 109, 114, 115] influence the mechanism. Low temperatures and overpotentials mainly give glyceraldehyde, Eq. (4.8), and glyceric acid, Eq. (4.9), where R = -$CH(OH)CH_2OH$. At higher overpotentials formic acid and carbon dioxide were found [16, 19, 110, 116–119].

$$RCH_2(OH) \rightarrow RCHO + 2H^+ + 2e^- \tag{4.8}$$

$$RCH_2(OH) + H_2O \rightarrow RCOOH + 4H^+ + 4e^- \tag{4.9}$$

The equations above show that water as an oxygen donor is required to oxidize glycerol to glyceric acid but not to glyceraldehyde. The similarity with the methanol voltammetry in Fig. 4.2b suggests that dissociative water adsorption is important also for glycerol oxidation. The onset potential at lower temperatures is the same as for methanol, suggesting that water dissociation is again the rate-determining reaction, which would imply that production of glyceraldehyde is the dominating reaction at the onset potential and in the early stages of the main oxidation peak as indicated by the work by Kwon et al [16].

An increase in temperature has been previously shown to increase the yield of CO_2 [120]. Changing the temperature has a dramatic effect on the voltammograms as shown in Fig. 4.5a-c. The maximum current density is increased about 100-fold by a temperature change from 21°C to 140°C. In addition, the reaction initiates at much lower potentials, which may have practical significance, and which also signals a change of mechanism. The quantitative analysis of these changes in terms of the reaction mechanism are discussed in the next section.

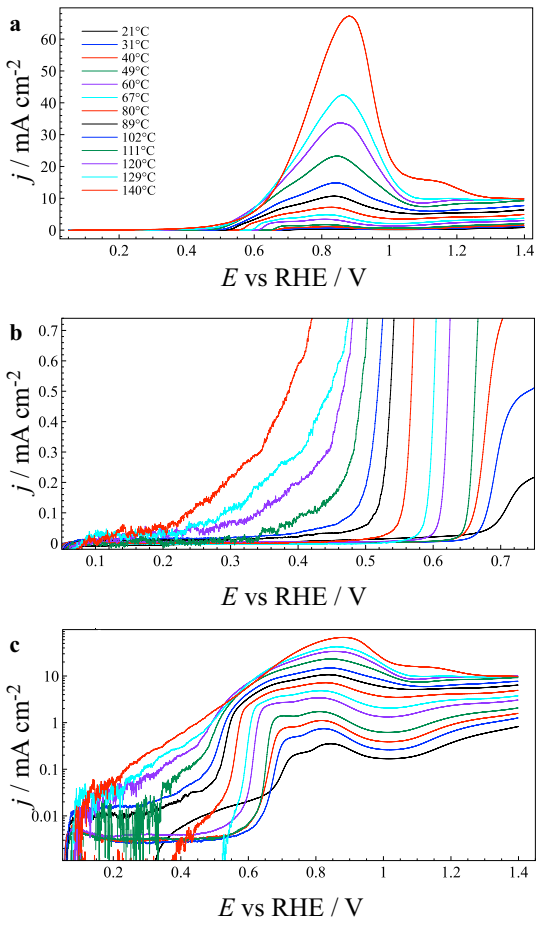

Figure 4.5: Temperature dependence of glycerol oxidation. Only the anodic scan direction of the voltammograms is shown. Scan rate 20 mV s^{-1}. (a) Full scale cyclic voltammograms, (b) expanded scale cyclic voltammogram highlighting the onset potentials, (c) logarithmic plots of current vs potential highlighting the Tafel slopes.

4.3.4 Kinetic analysis

Three parameters may be extracted from the temperature-dependent data and used to investigate the reaction mechanism. Onset potentials, E_{onset}, and Tafel slopes, b_T, were found directly from the slow-sweep voltammograms and are shown in Fig. 4.6. The activation energy was found at fixed potential from a series of voltammograms at different temperatures. In all cases only the initial stage of oxidation was analysed. The Tafel slopes were found from cyclic voltammograms at 20 mV s^{-1} as the slope of $\log(j)$ vs E, the slopes can be seen in Figs. 4.4c and 4.5c. The Tafel slope was defined as the initial slope after the onset potential. The onset potentials were defined as the potential at which the oxidation current exceeded a threshold value, given in the caption of Fig. 4.6.

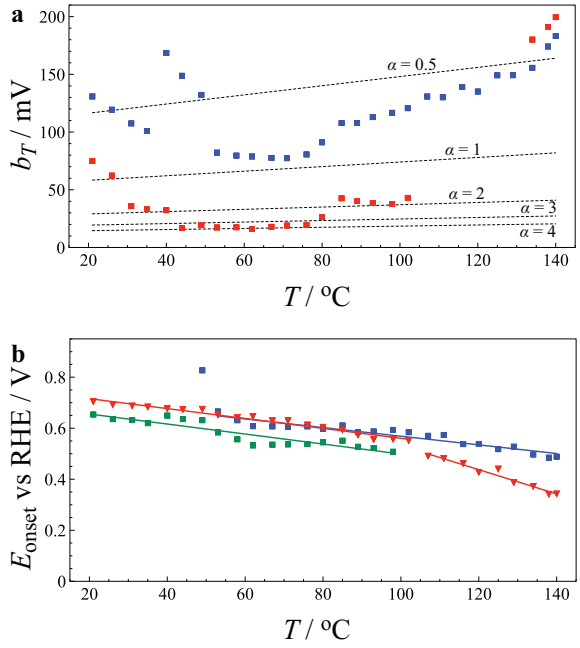

Figure 4.6: Temperature dependence of Tafel slopes and onset potentials. Methanol oxidation (blue) and glycerol oxidation (red). (a) Experimental initial Tafel slopes are the filled squares. The dashed lines correspond to the theoretical Tafel slopes for the α values shown. (b) Onset potentials for glycerol at threshold current 0.1 mA cm^{-2} (red triangles), methanol at threshold current 0.1 mA cm^{-2} (green boxes), and methanol at threshold current 1 mA cm^{-2} (blue boxes). Full lines are the regression lines. The potentials are corrected for the temperature dependence of the reference electrode and are given relative to RHE at 298 K.

Considering first the Tafel slopes for methanol oxidation, Tafel behavior was found from the start of oxidation until about the peak potential. The Tafel slopes changed consistently with temperature and had values corresponding to transfer coefficients $\alpha =$

$\ln(10)(RT/b_T F)$ ranging from 0.3 to 0.9. According to the conventional analysis, values close to 0.5 indicate that the first electron transfer step is rate determining, and values close to 1 indicate a chemical step after the first electron transfer step is rate determining. Assuming that the mechanism given in Eq. (4.3)-(4.6) dominates the current at all potentials and temperatures, the possible candidates are the dissociative methanol adsorption, Eq. (4.3), dissociative water adsorption, Eq. (4.5), or a surface diffusion step involving one of the adsorbed molecules in the reaction.

Looking at the Tafel slopes found for glycerol oxidation in Fig. 4.6a, there is a much larger change as the temperature is increased. The Tafel slopes for glycerol oxidation were not as constant as for methanol oxidation and for many temperatures they account for the sharp increase in current after the onset potential that can span less than 50 mV in some cases. Therefore, the low Tafel slope values in Fig. 4.6a resulting in high α values of have high uncertainties. Starting at room temperature, the transfer coefficient, α, increases in value from 0.7 to 2 and then further to 3.5 - 4. Above 75°C it drops to first about 2, and then down to less than 0.5 at temperatures above 130°C. Under the simplifying assumption that glyceraldehyde or glyceric acid are the main products at all temperatures [16], the α value may be used to narrow down the number of possible mechanisms. A low α value, such as at temperatures above 130°C indicates that the first dehydrogenation of glycerol may be rate determining. The high α values of 3.5 - 4 have numerous possibilities in terms of rate-determining steps, and is consistent with but not limited to glyceric acid dehydrogenation or the last electrochemical step in the production of glyceric acid as rate-determining step. For the intermediate α value of about 2, from 90 - 110°C, a possible mechanism is two electrochemical steps followed by a chemical one, and a candidate rate-determining step is the desorption of glyceraldehyde. The α values found from the Tafel slopes are most valuable if they range several orders of magnitude of current increase, and this is valid mostly at 140°C. Therefore, the low α values at these temperatures are a clear indication of a change in mechanism at high temperatures.

For the onset potentials in Fig. 4.6b, trend lines are shown to give an impression of how much the potential is changing. The resulting slopes are between -1.7 and -2.0 mV K^{-1} for methanol oxidation at all temperatures and for glycerol oxidation at low temperatures. For glycerol, there is a sharp change in slope to -4.7 mV K^{-1} at temperatures above 110°C, which leads to a much-reduced onset potential of about 0.35 V by 140°C. The onset potentials and the Tafel slopes gives a consistent picture of the mechanisms. For methanol, consistent trends across the whole temperature range support a single dominant reaction mechanism at all temperatures. However, for glycerol, both Tafel slopes and onset potentials change at high temperatures indicating a change in mechanism. The decrease in the onset potential to the region where dissociative adsorption of water does not occur [104–107] suggests a switch to glyceraldehyde as a product. The α value of about 0.5 would be consistent with the first electron-transfer step rate limiting, and the second electron transfer in a fast step. A slow oxidative adsorption step followed by a fast oxidative desorption step to give glyceraldehyde is consistent with the Tafel slope, and would lead to low surface coverage, explaining the absence of the surface passivation that seems to dominate at lower temperatures.

The last kinetic parameter available from the cyclic voltammetry data is the activation energy. Apparent activation energies were first found from the slopes of $\log(j)$ vs $1/T$ plots at fixed potential vs RHE in Fig. 4.7a-b. These were converted to the activation energies at fixed working-electrode metal-solution potential difference shown in Fig. 4.7c by the method detailed in experimental section.

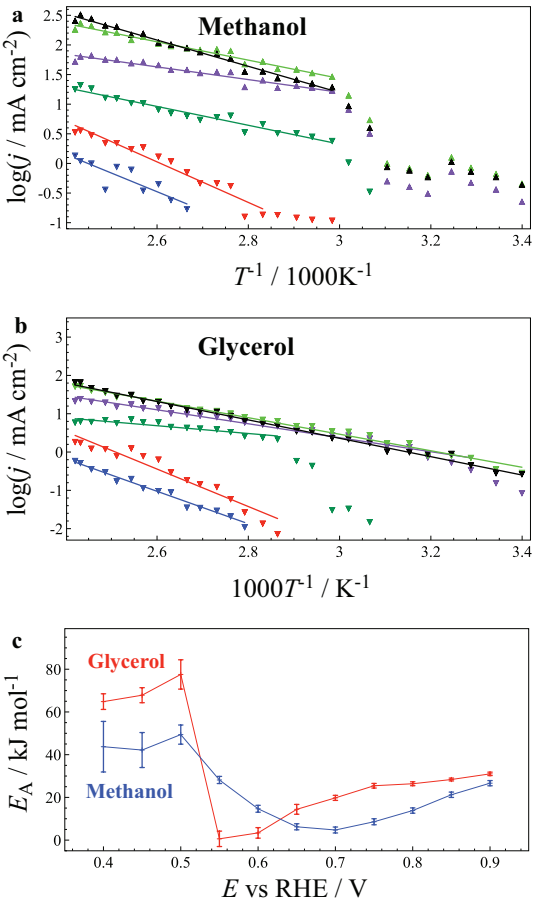

Figure 4.7: Arrhenius plots and activation energies. (a), (b) Arrhenius plots for methanol and glycerol oxidation. Potentials vs RHE: 0.4 V (blue), 0.5 V (red), 0.6 V (green), 0.7 V (purple), 0.8 V (light green), 0.9 V (black). Lines are regression lines used to calculate the apparent activation energies. (c) Corrected activation energies for methanol (blue) and glycerol (red).

At low overpotentials, only high temperature data was used for the Arrhenius plots because there is essentially no reaction at low temperatures. At low overpotentials, the activation energy is high for both methanol oxidation (40 - 50 kJ mol^{-1}) and for glycerol oxidation (60 - 80 kJ mol^{-1}). Relatively high activation energies ($>$ 60 kJ mol^{-1})

suggest a bond breaking process [12, 121, 122]. This supports the previous findings from Tafel slopes and onset potentials that either dissociative water adsorption or dissociative alcohol adsorption is rate determining. At higher overpotentials, a sharp drop in activation energy is observed, indicating a change in the mechanism. Low activation energies for both methanol oxidation (5 - 30 kJ mol^{-1}) and glycerol oxidation (5 - 35 kJ mol^{-1}) suggest that an adsorption or surface diffusion step is rate determining [98, 123–128]. Conclusions based on electrochemical activation energies are uncertain because they depend to some extent on the potential and on the charges of the species involved. However, combining the results in Fig. 4.7 with the findings from Tafel slopes and onset potentials, one can narrow down the possible rate-determining reaction steps. In the case of methanol oxidation, the mechanism seems to be stable as a function of both temperature and potential, and this indicates that either dissociative water adsorption, Eq. (4.5), or dissociative methanol adsorption, Eq. (4.3), is the rate-determining step in all cases. For glycerol oxidation, the picture is more complicated and the rate-determining step changes both as a function of temperature, Fig. 4.6, and as a function of potential, Fig. 4.5. At low temperatures, glycerol oxidation seems to be limited in the same way as methanol oxidation. At high temperatures, the same mechanism seems to span the whole potential range, and the kinetic parameters suggest that glyceraldehyde is the main oxidation product.

4.4 Conclusions

This work demonstrates a method for performing high purity aqueous electrochemistry at temperatures above the boiling point of water using commercially available equipment. This allows for the study of alcohol oxidation at high rates and at temperatures relevant for fuel cell operation. It uses efficient acquisition of data over a wide temperature range and allows the determination of kinetic parameters such as onset potentials, Tafel slopes and activation energies.

Methanol oxidation was studied at temperatures up to 140°C. The voltammograms and kinetic parameters show that the dissociative adsorption of water, (Eq. (4.5)), or the oxidation dissociative adsorption of methanol, Eq. (4.3), are rate-determining at all temperatures and at potentials below the main peak maximum.

Glycerol oxidation was studied over the same temperature range. For temperatures below 110°C, the rate-determining step is the same as for methanol oxidation. However, glycerol oxidation changes reaction mechanism above 110°C, the Tafel slope indicated that dissociative glycerol adsorption is the rate-determining step and the final reaction product is glyceraldehyde. This change in mechanism is associated with a large decrease in overpotential. This suggests that at the higher temperatures studied here, glycerol may be a viable fuel in a fuel cell, or in a electrochemical reactor to selectively oxidize glycerol to glyceraldehyde. Further studies will be required to chemically verify that glyceraldehyde is indeed the high-temperature reaction product.

4.5 Acknowledgements

Financial support from the Natural Sciences and Engineering Research Council of Canada (discovery grant 37035), the Research Council of Norway (project 221899), the University of Victoria, and the Norwegian University of Science and Technology is gratefully acknowledged. Thomas Holm thanks the Faculty of Natural Sciences and Technology at Norwegian University of Science and Technology for the award of a scholarship.

5 Dynamic Electrochemical Impedance Spectroscopy Study of Platinum Oxidation at High Temperatures

THOMAS HOLM[a,b], ROBERT L. SACCI[b], SVEIN SUNDE[a], FRODE SELAND[a], DAVID A. HARRINGTON[b]

[a] *Department of Materials Science and Engineering, Norwegian University of Science and Technology, NO-7491 Trondheim, Norway.*
[b] *Department of Chemistry, University of Victoria, Victoria, British Columbia, V8W 3V6, Canada.*

This chapter intended for publication at a later stage.

Abstract

A self-pressurized autoclave is used to study platinum oxidation at temperatures up to 140°C. A combination of conventional voltammetry and dynamic electrochemical impedance spectroscopy (dEIS) is used. The dEIS method gives dynamic data collected at varying surface condition, which can be used to study the processes occurring in real-time. The data from cyclic voltammetry and from the dEIS method are used to investigate the mechanism of platinum oxidation in an acidic solution. The fitted parameters from the dEIS results indicate that the surface oxide charge passed at a given potential is more influential than the temperature at a given potential. The observation that an estimate of the current can be found from the inverse charge-transfer resistance can serve as basis of a further investigation into the nature of the oxide.

5.1 Introduction

Platinum electrochemistry and especially platinum oxidation is a subject of study due to its relevance as a catalyst for numerous electrochemical reactions and because it is a model system for noble-metal oxidation [88]. In aqueous systems and in 0.5 M H_2SO_4 solution in particular, platinum has a signature cyclic voltammogram between the hydrogen evolution potentials and oxygen evolution potentials. This cyclic voltammogram is shown in Fig. 5.1, and the lower potentials below 0.3 V are dominated by two peaks related to hydrogen adsorption and desorption, while the anodic current starting at 0.8 V and the large reduction peak at 0.8 V are related to platinum oxide formation.

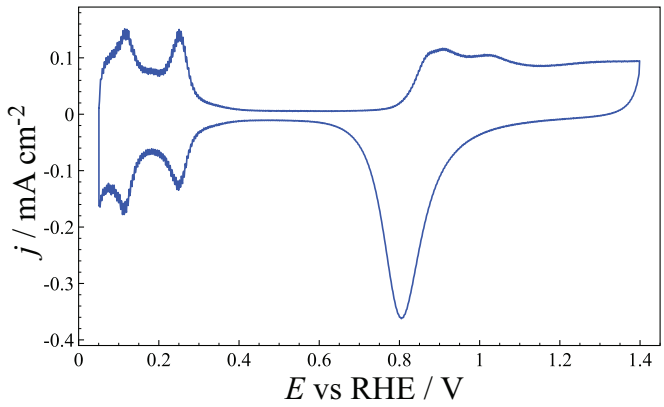

Figure 5.1: Cyclic voltammetry of platinum electrodes in 0.5 M H_2SO_4 at 40°C. Sweep rate is 100 mV s^{-1}.

Platinum oxidation is not limited to a monolayer and the cyclic voltammogram in Fig. 5.1 suggests that the mechanism is highly irreversible even at high temperatures. During platinum oxidation, a reversible layer of either oxide or adsorbed species is formed that is highly reversible [27], subsequently, some mechanism that allows multilayer growth follows. Many mechanisms have been suggested for this behavior including dipole flipping [129], film layer growth model [130], and a 3D rearrangement of the surface allowing multilayer growth.

Limited work has been done on the temperature dependence of the platinum oxidation reaction [36]. This is an important dependency, as a faster reaction rate is expected and kinetic parameters can be derived from such a study. To further enhance the power of a temperature study, cyclic voltammetry is combined with dynamic electrochemical impedance spectroscopy (dEIS). This allows for real time investigation of the surface processes occurring, which the surface is monitored by more parameters than just the current.

In this work, an electrochemical investigation using cyclic voltammetry of platinum in sulfuric acid is done for potentials up to 1.4 V, to limit the presence of high valence platinum (Pt(IV)) [28] and to limit the thickness to about 2 monolayers. In addition, the experimental work is done at temperatures up to 140°C, hereby expanding previous studies that have been limited to 50°C [36]. This is combined with the use of dEIS to further enhance the parameters studied. It builds on previous work on this system using impedance or ac voltammetry [26, 28, 30, 131]. These two techniques combined offer a powerful combination that allows for an expanded understanding of the platinum oxidation reactions.

5.2 Experimental

5.2.1 Experimental Setup

The pressurized vessel was acquired from Büchi AG, and is the same setup as used in chapter 4 and described in chapter 3. The system contained a 300 mL glass autoclave with a PTFE lid. The electrodes were sealed in glass and a custom made PTFE connection was made to fit into the 1/4 inch Swagelok connections. The reference electrode was a specially made reversible hydrogen electrode (RHE), with a small tube where hydrogen gas could be produced and collected to make the equilibrium on a Pt wire. All potentials are referred to this reference electrode unless otherwise specified. The counter electrode used was a mesh of Pt spot-welded to a Pt wire enclosed in glass. The working electrode used for the experiments was a short Pt wire electrode enclosed in glass. The area of the working electrode was 0.06 cm^2.

All of the glassware and the electrodes were cleaned in hot sulfuric acid before each run and rinsed at least twice in high purity water (Millipore Milli-Q). The vessel was filled with a fixed amount of electrolyte, 200 mL, sealed off, and put in a temperature controlled oil bath. This setup allowed for a maximum temperature of 150°C and 10 bar gauge pressure. Due to the corrosive nature of the electrolyte and the limited number of inputs to the autoclave, the temperature was fixed and measured in the oil bath. Therefore, a calibration of the relation between the electrolyte temperature and the oil bath temperature was done using 200 mL of high purity water, facilitating the calculation of electrolyte temperature from the oil bath temperature.

The electrochemical experiments were done using a 0.5 M sulfuric acid supporting electrolyte (Ultrapur 93-98%). The potentiostat used was a Gamry Ref. 600 potentiostat. The electrodes were electrochemically cycled between 0.05 and 1.4 V for 100 scans at 200 mV s^{-1} prior to the heating experiment. The heating experiments were conducted by heating the electrode to the desired temperature and then starting a cycle of experiments taking in total less than 1 hr. After each cycle, two hours was allowed for the electrolyte to reach the next temperature in the series (20 K steps). The electrochemical series of experiments consisted of cyclic voltammograms between 0.05 and 1.4 V run at scan rates between 5 mV s^{-1} and 1000 mV s^{-1}, and potentiostatic electrochemical impedance spectroscopy run at three different steady-state potentials (0.3, 0.6, 0.9, and 1.2 V). In addition, two full series of dynamic electrochemical impedance spectroscopy (dEIS) were run at scan rates of 5 mV s^{-1} and 20 mV s^{-1}. The cyclic voltammograms were normalized by the charge of the hydrogen adsorption peaks between 0.4 and 0.07 V at room temperature. The normalization constant used to estimate the electrochemically active surface area of the platinum electrodes was 220 μC cm^{-2}.

5.2.2 Dynamic electrochemical impedance spectroscopy

This method consists of running a standard voltammetric technique like chronoamperometry or cyclic voltammetry, while simultaneously applying a multisine ac signal to the

potential so that electrochemical impedance spectroscopy can be conducted simultaneously. The dc signal was generated using a Hokuto Denko Function Generator HB-111 and the ac signal was synthesized using in-house built software previously described [50, 51]. The dc and ac potential signals were then added together using a SRS SIM900 Mainframe with SIM910, SIM980, and SIM983 modules and a Keithley KUSB-3116 ADC/DAC converter and applied through a Gamry Ref. 600 potentiostat. The resulting current response was sampled continuously using the Keithley KUSB-3116 module along with the dc and ac potential signals applied to the cell. This response was post-processed to get the "steady-state" voltammogram and an electrochemical impedance spectra at intervals of 5 mV for 5 mV s^{-1} sweep rate and 10 mV for 20 mV s^{-1} sweep rate. The frequencies applied ranged from 1 Hz to 10 kHz and followed the rules developed by Popkirov and Schindler [132]: 1) each frequency in the waveform had an integer number of periods in the waveform period, $T = 1/f_{\min}$; 2) the rms amplitude for the individual sine waves decreased by one-half for every decade increase in the frequency; 3) the phases of the individual sine waves were randomized; 4) the maximum amplitude of the AC waveform was 30 mV which corresponded to a maximum amplitude of 4.5 mV_{rms} for the lowest frequency and a minimum of 0.5 mV_{rms} for the highest frequency.

The impedance data was fitted to an equivalent circuit representing the electrode processes. The circuits considered are shown in Fig. 5.2 and are denoted as R, C, and W, where R are resistances, Q are constant phase elements (CPE), C are capacitors, and W are Warburg elements. The fitting was done using the Zview software (Scribner Scientific) which allowed for multiple spectra to be fitted sequentially. As an aide to get a higher quality fit, a constant real resistance of 100 Ω was added so that the real impedance was emphasized at high frequencies. The data is plotted as a complex capacitance plot because this type of plot enhances the features for this type of impedance data. The transformation from impedance to complex capacitance was straightforward, $C(\omega) = 1/(i\omega(Z_{\mathrm{Re}}(\omega) + iZ_{\mathrm{Im}}(\omega)))$.

5.3 Results and discussion

5.3.1 Cyclic voltammetry

The influence of temperature on the cyclic voltammogram is shown in Fig. 5.3 at a sweep rate of 200 mV s^{-1}. The features of the voltammogram remain largely constant, i.e., the general features are platinum oxidation, platinum oxide reduction and hydrogen adsorption and desorption. However, as previously reported in the literature [36], the temperature change has an influence on these processes, and most profoundly on the platinum oxidation/platinum oxide reduction. The increase in temperature reduces the onset potential of the oxidation and increase the slope of the initial oxidation. After the platinum oxidation has commenced, the more stable plateau current increases as the temperature increases and in total, this gives more anodic charge during platinum oxidation. Subsequently, this oxide is reduced during the negative going sweep and the charge under the cathodic peak at 0.8 V is increased as temperature increases. The hydrogen adsorp-

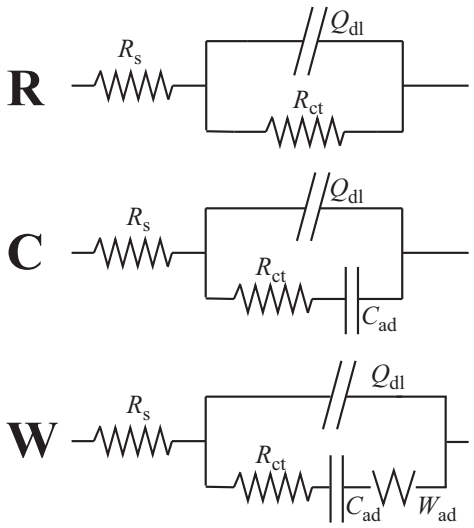

Figure 5.2: Equivalent circuits considered for the surface processes occurring on the platinum surface during cyclic voltammetry.

tion and desorption features shift slightly to lower potentials as the temperature increases in a similar fashion as the first platinum oxidation peak. The small peak that occurs at about 0.7 V during the anodic sweeps at the highest temperatures is attributed to impurity oxidation. Interestingly, the temperature change is analogous to a change in sweep rate if the cyclic voltammograms are normalized by the sweep rate as shown in Fig. 5.4. Therefore, a sweep rate dependence, i.e., really a time dependence, gives the same qualitative change as a change in temperature. A low sweep rate results in oxidation at lower potentials and a thicker oxide layer. At the same time, the sweep rate dependence illustrates that while the hydrogen adsorption and desorption processes are purely reversible fast monolayer processes, i.e., independent on sweep rate, the platinum oxidation process is a kinetically controlled process both dependent on time and temperature.

A simplified mechanism for platinum oxidation is suggested in Eqs. (5.1)-(5.5). Although the specific mechanisms of each step in the reaction order are topics of discussion, the formation of a multilayer oxide like platinum involves first adsorption of O or OH^-, Eqs. (5.1)-(5.2), followed by a place-exchange mechanism, Eq. (5.3), that allows for oxide "flipping" into the platinum matrix exposing new platinum surface atoms for subsequent oxidation, Eqs. (5.4)-(5.5). The mechanism proposed in Eqs. (5.1)-(5.5) limits the oxidation to 880 μC cm^{-2}, which is the measured limit at 1.4 V [36], and can be verified by current integration. It is also assumed that the surface is at "steady-state", i.e., that the subsequent cycles overlap and that long-term irreversible reordering of the surface or dissolution of platinum plays a minor role. While infrared spectroscopy studies suggest that the adsorbed hydroxide ion is a central part of the mechanism [133], and first principles studies indicate that hydroxide adsorption can occur at potentials as low as 0.6 V [104, 106, 107], it is not visible as a species on the surface through EQCM [24]. It

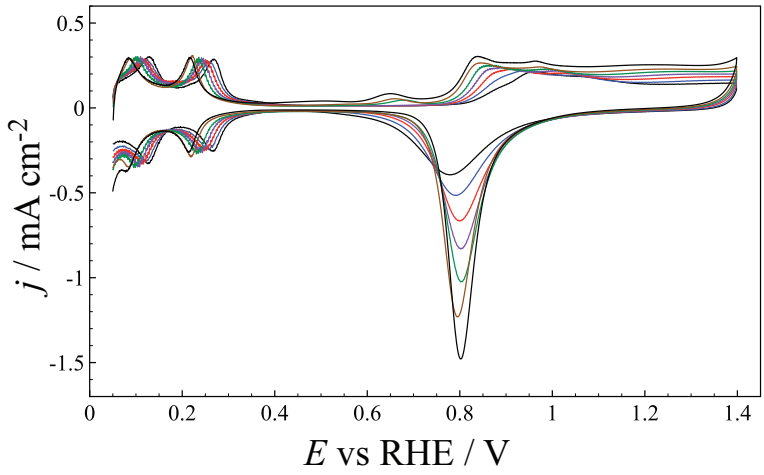

Figure 5.3: Cyclic voltammogram oxidation and reduction of platinum in sulfuric acid solution. Sweep rate is 200 mV s^{-1}. Temperature are 24°C (black small current), 40°C (blue), 60°C (red), 80°C (purple), 100°C (green), 120°C (brown), and 140°C (black large current).

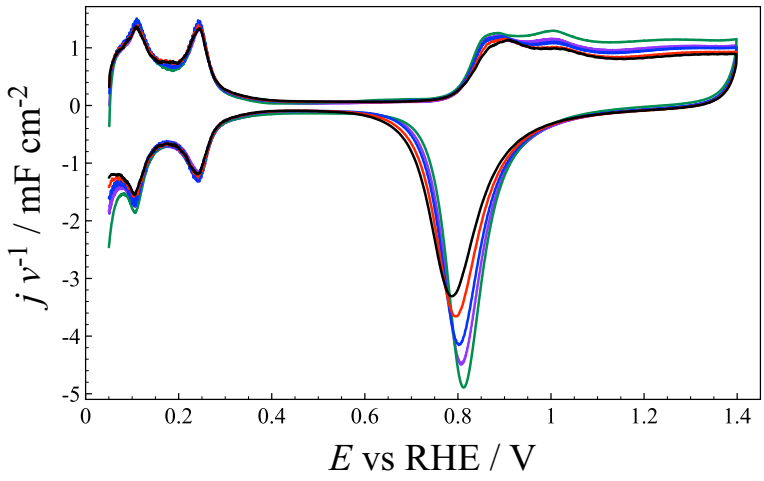

Figure 5.4: Cyclic voltammetry normalized by sweep rate for platinum electrodes in 0.5 M H_2SO_4 at 80°C. The sweep rates are 50 mV s^{-1} (green), 100 mV s^{-1} (purple), 200mV s^{-1} (blue), 500 mV s^{-1} (red), 1000 mV s^{-1} (black).

has therefore been suggested that Eqs. (5.1)-(5.2) can be viewed as a single step [36] or that the first step is a fast quasi-equilibrium that is not giving much coverage of surface hydroxide [134, 135]. If the hydroxide steps, Eq. (5.1) and Eq. (5.4), are viewed as fast steps the total reaction, although being a surface reaction, can be viewed as a ECE mechanism, where the surface reconfiguration giving multilayer oxide formation, Eq. (5.3), is a chemical step.

$$\mathrm{Pt} + \mathrm{H_2O} \rightleftarrows \mathrm{PtOH} + \mathrm{H^+} + \mathrm{e^-} \tag{5.1}$$

$$\mathrm{PtOH} \rightleftarrows \mathrm{PtO} + \mathrm{H^+} + \mathrm{e^-} \tag{5.2}$$

$$\mathrm{PtPtO} \leftrightarrows \mathrm{PtOPt} \tag{5.3}$$

$$\mathrm{PtOPt} + \mathrm{H_2O} \rightleftharpoons \mathrm{PtOPtOH} + \mathrm{H^+} + \mathrm{e^-} \tag{5.4}$$

$$\mathrm{PtOPtOH} \rightleftharpoons \mathrm{PtOPtO} + \mathrm{H^+} + \mathrm{e^-} \tag{5.5}$$

A mystery in the mechanism is that the current does not show an exponential increase. Therefore, an empirical rate-law with a Temkin term has been suggested for the reaction in Eq. (5.6) [135]. In this rate-law, j_α is the oxide forming current, k is a reaction constant, σ is the total oxide charge density, and B and C are constants. In contrast to what would be expected from a reaction mechanism as in Eqs. (5.1)-(5.5), there is not dependence on free sites at the surface as there is no marked change in mechanism when the oxide charge density passes what would correspond to a monolayer. Instead, one has the dependency on the total oxide charge density which could be converted into a de-facto coverage, $\Theta_{\mathrm{Ox}} = \sigma/220\mu\mathrm{C\ cm^{-2}}$. The resulting current of the rate-law in Eq. (5.6) is an exponentially increasing current that is slowed down until it reaches a plateau current that is held indefinitely. In Fig. 5.3, there are some minor peaks at the start of the oxide formation stage (0.8-1.0 V) and then a slowly decreasing current until the maximum potential at 1.4 V, but overall a good fit with such a rate-law. This also fits well with previous studies [36] where the rate-law is followed until 1 monolayer and then the reaction is suggested to be limited by the place-exchange mechanism. Furthermore, the C parameter in Eq. 5.6 has been measured to have the same order of magnitude as a Tafel behavior and is assumed to be of a similar significance [129, 136].

$$j_\alpha = \frac{\partial \sigma}{\partial t} = nFk\exp(CE)\exp(-B\sigma) \tag{5.6}$$

$$b_T = \left(\frac{\partial \log j}{\partial E}\right)^{-1} = \frac{RT}{\alpha F}\ln(10) \tag{5.7}$$

Now, from the cyclic voltammetry data a Tafel slope can be found from the initial currents in both the anodic and cathodic processes. For the negative-going sweep direction, a sweep rate of 20 mV $\mathrm{s^{-1}}$ was used giving data that spans one order of magnitude of current. For the positive-going sweep direction, a sweep rate of 100 mV $\mathrm{s^{-1}}$ was used and the current spanned less than one order of magnitude. Assuming that this represents the real Tafel slope, b_T, the resulting charge-transfer coefficient from Eq. (5.7) can be found

Table 5.1: Transfer coefficient from Tafel slopes from 20 mV s^{-1} CV data, and integrated cathodic current for CVs at 200 mV s^{-1}. The number of electrons transferred per Pt atom is calculated assuming that the hydrogen adsorption peaks represent 1 e^-/Pt.

Temperature / °C	α	Charge density / μC cm^{-2}	n
24	0.32	385	1.77
40	0.36	433	1.98
60	0.29	478	2.21
80	0.41	521	2.38
100	0.38	574	2.57
120	0.69	613	2.75
140	1.06	670	2.99

and is plotted vs the temperature in Fig. 5.5a. Assuming that the rate law, Eq. (5.6), describes the current at the start of platinum oxidation, the anodic transfer coefficient, α, is expected to be constant. This is partly supported by the experimental results, but there is a slow increase from 0.55 to 0.92 when the temperature is increased from 23°C to 120°C. The lower value at 140°C can partly be explained by the larger role that impurities play at these potentials making the slope determination more complicated (see Fig. 5.3 at 0.7 V). The range of values indicates that the reaction is moving from a one-step electrochemical reaction being rate-determining, Eq. (5.1), to a range where simultaneous $2e^-$ transfer is rate determining, Eqs. (5.1)-(5.2), or an electrochemical step followed by a chemical rate-determining step. This indicates that the first hydroxide adsorption step has a role in the mechanism. For the reduction reaction, the charge-transfer coefficient is constant until 100°C at 0.29-0.41, then it increases up to 1.06 at 140°C. This behavior is most easily explained by the thickness of the oxide at the start of the oxide reduction reaction. As seen in Table 5.1, the number of electrons passed during oxidation of platinum increases from 1.77 at 24°C to 2.99 at 140°C. From the reaction mechanism stated in Eqs. (5.1)-(5.5), when two electrons are used pr Pt site, the place-exchange mechanism, Eq. (5.3), is active meaning that upon reduction of this layer, an electrochemical step followed by a chemical place-exchange mechanism leads to a transfer coefficient, α, of 1. Especially, this is most relevant where the number of electrons passed pr surface, n, site reaches close to 3. For the temperature at 100°C and below, this indicates that an electrochemical step is rate-determining, and a reverse version of Eq. (5.2) might be a potential candidate.

5.3.2 Dynamic Electrochemical Impedance Spectroscopy

The combination of dEIS with cyclic voltammetry is attractive as it allows instantaneous measurement of cyclic voltammogram and electrochemical impedance spectroscopy, with determination of the impedance spectra at non-steady-state surface conditions. This type of treatment has been discussed in a previous work in our group [27, 51], and the experimental guidelines given there were followed. For platinum oxidation, the dEIS method

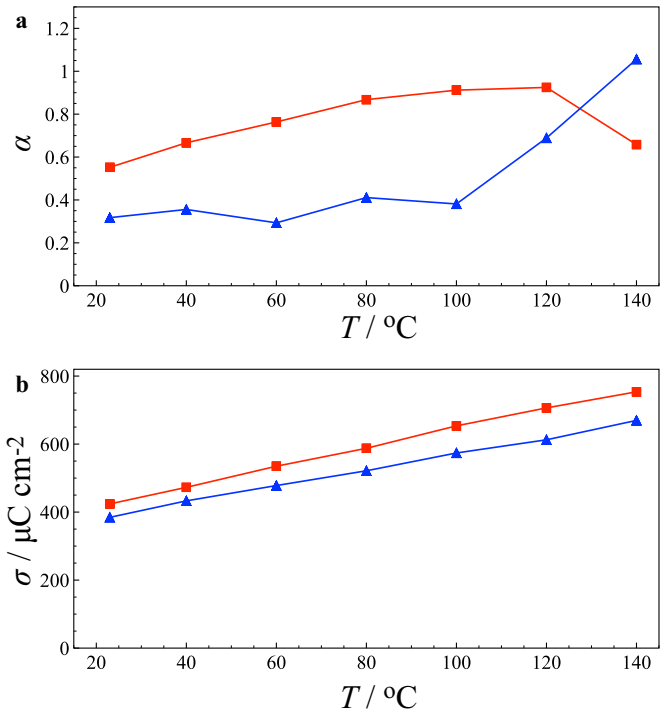

Figure 5.5: Cathodic Tafel slopes (blue - from 20 mV s^{-1}) and anodic Tafel slopes (red - from 100 mV s^{-1}) as a function of the temperature (a), the y-axis gives the charge-transfer coefficient, α. The integrated charge for the platinum oxidation (red) and the platinum oxide reduction (blue) currents (b).

has been documented before [27, 30, 131], and the equivalent circuits are based on the theoretical systems. The theoretical process known to occur on a platinum electrode should result in a W circuit [27] or even more complex circuits [30]. However, to decide on which circuit is most appropriate both visual representation and an F-test, Eq. (5.8) was used.

$$F_{\chi^2} = \frac{\chi^2_{\text{old}} - \chi^2_{\text{new}}}{\chi^2_{\text{new}}} \frac{\nu_{\text{new}}}{\beta} \tag{5.8}$$

Here, the χ^2 values are the fit quality parameter given by the fitting software, ν is the degrees of freedom defined as $2N_{\text{freq}} + N_{\text{parameters}} - 1$, i.e., the number of frequencies plus the number of parameters minus one, and β is the number of parameters added from the old to the new model, and this number should be equal to 1. An example of the visual representation of the impedance data as a complex capacitance plot is given in Fig. 5.6. In Fig. 5.6, three potentials giving very different response are shown at room temperature, one during hydrogen adsorption/desorption reaction (a), one during the double-layer charging zone (b), and one right after the onset of platinum oxidation (c). From the visual representation in Fig. 5.6, it is evident that for most potentials, the addition of elements to the R-circuit, Fig. 5.2, gives a small change in fit quality and that the difference between the circuits is at the lowest frequencies, i.e., where our measurement method is less accurate. Therefore, our analysis was for all temperatures, potentials and sweep rates limited to the R-circuit. By using an estimated solution resistance from high-frequency steady-state impedance spectra and assuming that this is constant at all potentials, impedance parameters with low uncertainties were obtained. For the CPE parameters, Q and ϕ, (defined as $Z_{\text{CPE}} = 1/(i\omega)^{\phi}Q$), the parameters had a standard deviation of less than 5%. For the charge-transfer resistance, R_{ct}, the standard deviation varied and gave a low uncertainty during platinum oxidation and during hydrogen evolution, while it gave uncertain values in between where only adsorption processes and double-layer charging occur.

The fit quality, χ^2, and all the impedance parameters from the R-circuit in Fig. 5.2 are shown in Fig. 5.7 for the anodic sweep direction at 24°C and a 5 mV s^{-1} sweep rate. A similar figure for the cathodic sweep direction is shown in Fig. 5.8. These two figures, Figs. 5.7-5.8 show the current divided by sweep rate, CPE parameter, Q, and CPE coefficient, ϕ, in the (a) figure, and the solution resistance, R_{s} (constant), charge-transfer resistance, R_{ct}, and the fit quality, χ^2 in the (b) figure.

Looking at the results in Figs. 5.7-5.8, the fit quality, χ^2, is fairly stable throughout the voltammogram, and is between 10^{-2} and 10^{-4}. The fit quality is consistently better for potentials in the double-layer zone and after the initial oxidation of platinum. It is worse during the first stage of platinum oxidation and during hydrogen adsorption/desorption. This is also evident from Fig. 5.6, where the 900 mV case is more complicated and this is at potentials where the initial platinum oxidation occurs.

The presence of a CPE instead of an ideal capacitor greatly complicates a physical interpretation of the measured quantities. Looking at the values of the parameters, Q and ϕ, it is evident both from Fig. 5.2 and from Figs. 5.7-5.8, that at many potentials,

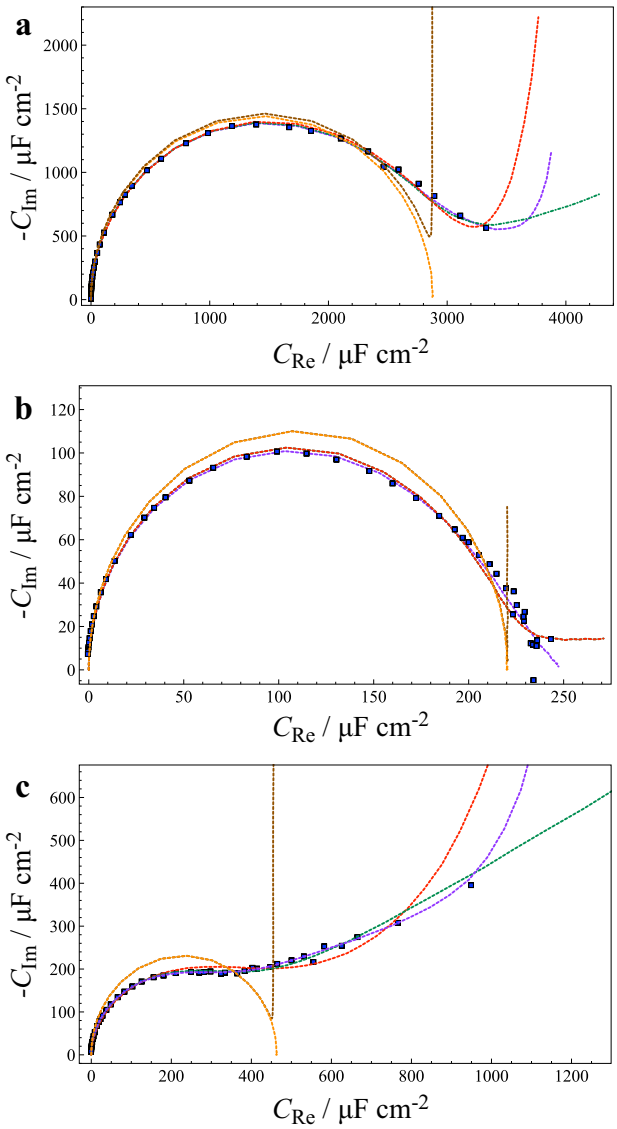

Figure 5.6: Comparison of fits to the different equivalent circuits from Fig. 5.2. The figures shows the experimental data (squares) with the R-circuit (red), the C-circuit (green), and the W-circuit (purple) plotted for room temperature complex capacitance spectra at (a) 70 mV, (b) 500 mV, and (c) 900 mV. All data are for the upward scan direction at 5 mV s^{-1}. In addition, the R circuit with the CPE element replaced with a capacitor (brown) and an RC circuit (orange) are included for comparison.

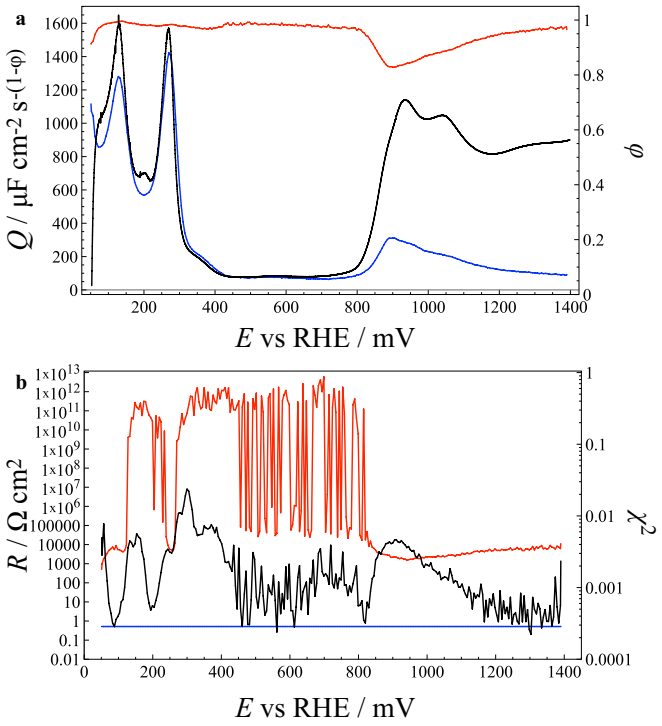

Figure 5.7: Figure showing the fitted parameters for a R-circuit. Top figure (a) shows the cyclic voltammetry current, $j\nu^{-1}$, vs the potential (black), the Q-values from R-circuit fitting (blue), and the ϕ values from the fitting (red, second y-axis). The bottom figure (b) shows the charge-transfer resistance, R_{ct} (red), the solution resistance, R_{s} (blue), and the fit quality as χ^2 (black, second y-axis). All data are collected during anodic scan direction (increasing potentials) run at a 5 mV s^{-1} sweep rate at room temperature (24°C).

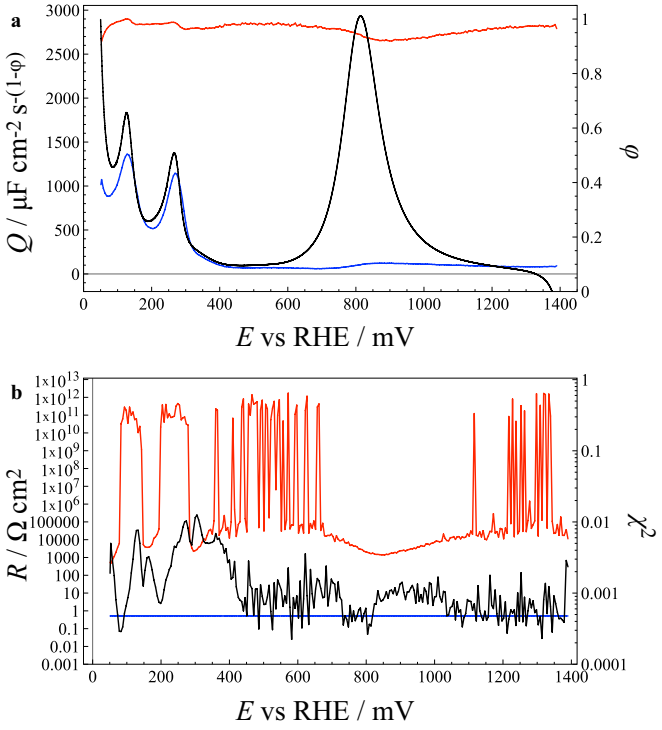

Figure 5.8: Figure showing the fitted parameters to a R-circuit. Top figure (A) shows the cyclic voltammetry current, $j\nu^{-1}$, vs the potential (black), the Q-values from R-circuit fitting (blue), and the ϕ values from the fitting (red, second y-axis). The bottom figure (B) shows the charge-transfer resistance, R_{ct} (red), the solution resistance, R_{s} (blue), and the fit quality as χ^2 (black, second y-axis). All data are collected during cathodic scan direction (decreasing potentials) run at a 5 mV s^{-1} sweep rate at room temperature (24°C).

the response is near ideal giving a CPE coefficient value, ϕ, between 0.95 and 1. In this work, this is interpreted as a near ideal capacitor and treated as such. At some potentials, especially at the onset of platinum oxidation, 900 mV in Fig. 5.7, the CPE parameter drops to 0.82, i.e., far from ideal behavior. A method for determining an equivalent capacitance has been suggested in the literature [137, 138], where the CPE behavior has the origin in surface heterogeneities. The CPE element can be mathematically described by a distribution of time constants at the surface [138], and this could be associated with the many facets at a polycrystalline platinum surface. In addition to a drop in CPE coefficient, ϕ, a simultaneous increase in the value of the CPE parameter, Q, occurs. As the increase in CPE parameter is temporary, this effect is interpreted as a portion of the surface oxidation process being more reversible. As the oxide layer grows and the potential increases, the surface shows a more ideal capacitive response that is similar to when the sweep direction is reversed. Therefore, at higher potentials, i.e., close to 1400 mV, this is a measure of the capacitance of the oxidized surface and indicates that the pure platinum surface and the platinum oxide surface both show close to ideal capacitor behavior with similar capacitance. In addition, this confirms the irreversible nature of the platinum oxide meaning that as the oxide coverage increases, the reversibility of the reaction is reduced. This could be because the observed reversibility is related to the adsorption at the uncovered surface. The difference between the platinum oxide processes and the hydrogen adsorption and desorption processes illustrates the difference between a highly ideal adsorption process and this irreversible oxide formation process. At the low potentials of hydrogen adsorption, the CPE parameter, Q, traces the current both in the anodic and cathodic sweep direction indicating that hydrogen adsorption and desorption is a highly reversible and fast reaction. In the double-layer zone, at 600 mV, the CPE parameter, Q, has the value of 70 μF cm^{-2} s$^{-(1-\phi)}$ and has a CPE coefficient, ϕ, of 0.98 showing a similar value as previously reported [139] for the sum of the double-layer capacitance and the capacitance related to anion adsorption.

For the charge-transfer resistance, R_{ct}, it is evident from Fig. 5.6a-b that when the current largely has a capacitive origin (at potentials less than 700 mV), there is high uncertainty in the value of the R_{ct} parameter. Therefore, values above 10^6 Ω cm^2 are not treated as reliable results. Applying this rule limits sensible interpretation of R_{ct} parameter to potentials above 800 mV in the anodic scan, between 1100 and 650 mV in the cathodic scans and at very low potentials when hydrogen evolution is occurring. Wherever the charge-transfer resistance has 10^6 Ω cm^2 or less, it indicates that a faradaic reaction occurs giving charge-transfer of electrons.

5.4 Temperature dependence of dEIS parameters

When studying the fitted dEIS parameters as a function of temperature, a range of dependencies apply. Most of the parameters are in some way dependent on surface state, oxide coverage making the trends more complicated than actually plotting a simple parameter value as a function of temperature. This is illustrated in Fig. 5.9 where (a) the CPE

parameter, Q, and (b) the CPE coefficient, ϕ, are plotted as a function of temperature at selected potentials for the 5 mV s^{-1} sweep rate. The fitting procedure indicate that the standard deviation in these parameters is less than 2% of the value for the CPE parameter, Q, and less than 0.5% for the CPE coefficient, ϕ. However, the real standard deviation of the measurements is probably several times the standard deviation estimated from the fitting procedure. The potentials chosen for Fig. 5.9 are chosen to illustrate the stages of the platinum oxidation. Therefore, the potentials range from oxide free, 470 mV up and 500 mV up, to the initial oxide formation stage, 1000 mV up, to mature oxide layer, 1370 mV up and 1200 mV down, and again to oxide free surface, 500 mV down. Firstly, it is noted that except for at the onset of platinum oxide formation (1000 mV), the CPE parameter, Q, has a fairly stable value of between 60 and 100 μF cm^{-2} $s^{-(1-\phi)}$. In a similar way, the CPE coefficient is at values between 0.95 and 1 for most of the potentials. Such a finding indicate that there is really not much difference between the platinum oxide and the platinum surface in terms of capacitive properties and capacitance values. However, this changes for the 470 and 500 mV values at temperature above 100°C and for the onset of platinum oxidation. This change at high temperatures is likely influenced by the impurities visible at 0.7 V. The change observed in the CPE parameter, Q, is always accompanied by a drop in the CPE coefficient, ϕ, indicating that it is no longer a measure of the actual capacitance. As for the temperature influence, a slight drop in CPE parameter value is visible, although this is not a very clear trend. In addition, the CPE parameter after the oxide formation may be influenced by the total oxide charge density and the result may be somewhat skewed by this as a higher temperature gives a higher total oxide charge density at the same potentials.

For the charge-transfer resistance, R_{ct}, a similar presentation as for the CPE parameter is given in Fig. 5.10 for the 5 mV s^{-1} sweep rate. The standard deviation of charge-transfer resistance is estimated to be less than 10% from the fitting procedure. Again, the real standard deviation is probably quite much higher, and Fig. 5.10 gives an indication of what the real standard deviation is. The charge-transfer resistance values, R_{ct}, are presented directly (a) and (b) as the inverse charge-transfer resistance, R_{ct}^{-1}, in Fig. 5.10. The potentials presented are all part of where platinum oxide formation is expected where a series is at the onset of the platinum oxidation, 850 mV up, 900 mV up, and 1000 mV up, some are at potentials where the oxide layer is well beyond formation, 1200 mV up and 1370 mV up, and some potentials are during the platinum oxide reduction, 1000 mV down, 900 mV down, and 800 mV down. While there is a change in the value of the charge-transfer resistance, R_{ct}, there is no definite trend as the temperature is increased. Therefore, it is concluded that R_{ct} is more a function of surface condition than of temperature for these potentials. Especially, this is visible for the inverse charge-transfer resistance, R_{ct}^{-1}, which is a measure of the current response as the potential is perturbed, $R_{\mathrm{ct}}^{-1} \approx (\partial j/\partial E)$ at constant surface conditions. Similarly to what is observed in Figs. 5.7 and 5.8, the charge-transfer resistance, R_{ct}, has the lowest value during the onset of platinum oxide formation or during platinum oxide reduction, and this is seen for temperatures up to 80°C for the 900 mV up, 1000 mV up, 900 mV down, and 800 mV down. As the temperature increases, the trend is similar, but as observed in Fig.

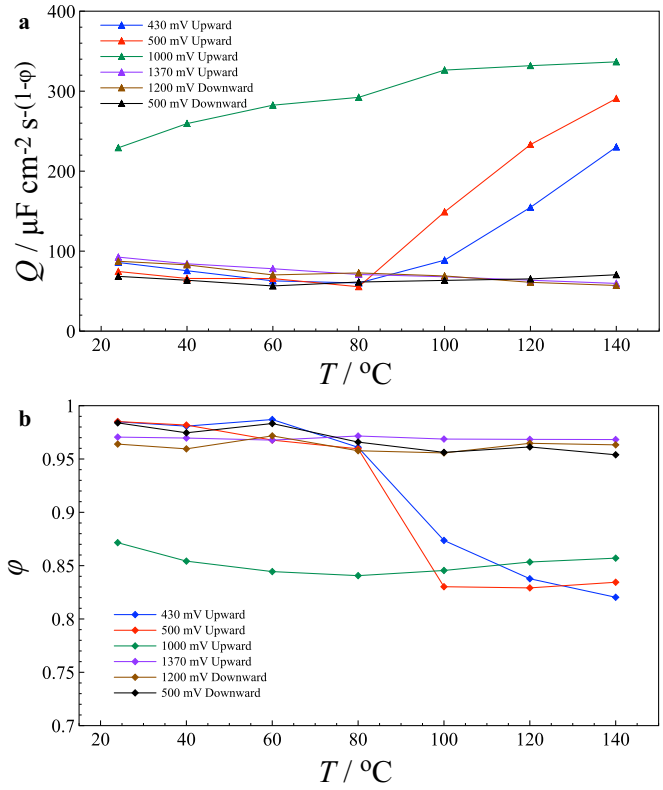

Figure 5.9: Temperature dependence of the CPE parameter, Q (a), and the CPE coefficient, ϕ (b), at selected potentials.

5.3, the platinum oxide formation starts at lower potentials and the platinum oxide reduction is finished at higher potentials meaning that the potentials with the highest current change as the temperature increases which will influence the charge-transfer resistance. Therefore, no trend of temperature influence on the charge-transfer resistance at a given potential can be found.

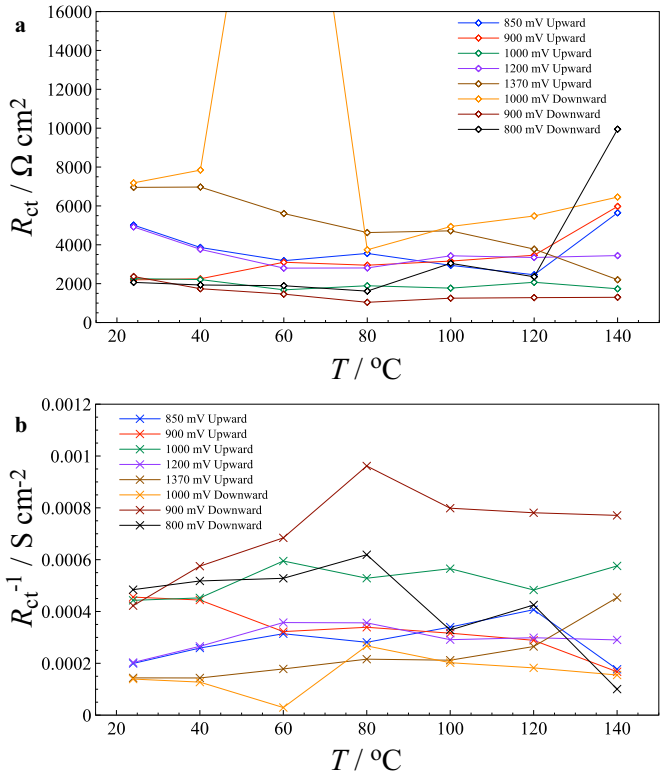

Figure 5.10: Temperature dependence of the charge-transfer coefficients, R_{ct}. Showing the charge-transfer resistance (a) and the inverse charge-transfer resistance (b).

5.5 Possible interpretation of the charge-transfer resistance

Building on the observation that the charge-transfer resistance has the lowest value during the initial platinum oxide formation and that it drops off after more oxide formation charge has passed, the inverse charge-transfer resistance, R_{ct}^{-1} is investigated further. Observing that a current can be estimated based on that the charge-transfer resistance can be viewed as $(\partial j/\partial E)$ at constant surface conditions, an estimate of the current can be found by scaling this to the measured current in the cyclic voltammograms. The equation used to scale this is given in Eq. (5.9), where ΔE is the difference in potential between each dEIS measurement which is really an arbitrary constant, and a which is a scaling constant.

$$j_{\mathrm{Rct}} = a\left(\frac{\partial j}{\partial E}\right)\Delta E \approx a\frac{\Delta E}{R_{\mathrm{ct}}} \tag{5.9}$$

By using Eq. (5.9) and the scaling factor, $a = 2$, the plot of the dEIS current, j_{Rct}, and the cyclic voltammogram are presented in Fig. 5.11 for the different sweep rates, (a) 5 mV s^{-1} and (b) 20 mV s^{-1}. The ΔE values used were 5 mV for the 5 mV s^{-1} results and 10 mV for the 20 mV s^{-1} results. As can be observed in Fig. 5.11 for both sweep rates, the charge-transfer current, j_{Rct}, scales well with the cyclic voltammetry current at the onset of platinum oxide formation, while it slowly drops off as more charge is passed to form platinum oxide. The difference between the sweep rates is that the higher sweep rate results, Fig. 5.11b, better trace the cyclic voltammetry current, while the lower sweep rate results, Fig. 5.11a, have a large offset at high potentials. This indicates that the total charge passed for oxide layer formation does in fact influence the charge-transfer resistance, and this influence is probably larger than the influence of temperature as observed in Fig. 5.10. In addition, the estimated current from the charge-transfer resistance, j_{Rct}, can possibly be viewed as a measure of the more reversible portion of the total current, and a measure of the ratio of more irreversible current to more reversible current passing at a given point. This observation can serve as a basis for a more thorough investigation using dEIS into the platinum oxide mechanism.

5.6 Conclusion

A self-pressurized autoclave was used to study platinum oxidation in 0.5 M H_2SO_4 solution successfully up to 140°C. High quality cyclic voltammograms were collected at all of these temperatures showing a clean electrolyte. This allowed for the derivation of kinetic parameters such as Tafel slope at all temperatures giving a change that indicated the importance of the place-exchange mechanism for platinum oxidation and platinum oxide reduction.

Combination of cyclic voltammetry with dynamic electrochemical impedance spectroscopy gave an additional set of parameters measured instantaneously at the same potentials as the cyclic voltammetry. Impedance spectra were measured at all temperatures, potentials and at sweep rates of 5 mV s^{-1} and 20 mV s^{-1}. The simultaneous measurement of impedance spectra and cyclic voltammetry made it possible to observe temperature dependent parameters for the impedance spectra, and indicated the fitted impedance parameters are more dependent on surface condition than on temperature.

5.7 Acknowledgments

Financial support from the Natural Sciences and Engineering Research Council of Canada, the University of Victoria and the Norwegian University of Science and Technology is gratefully acknowledged. Thomas Holm thanks the Research Council of Norway for the award of a scholarship.

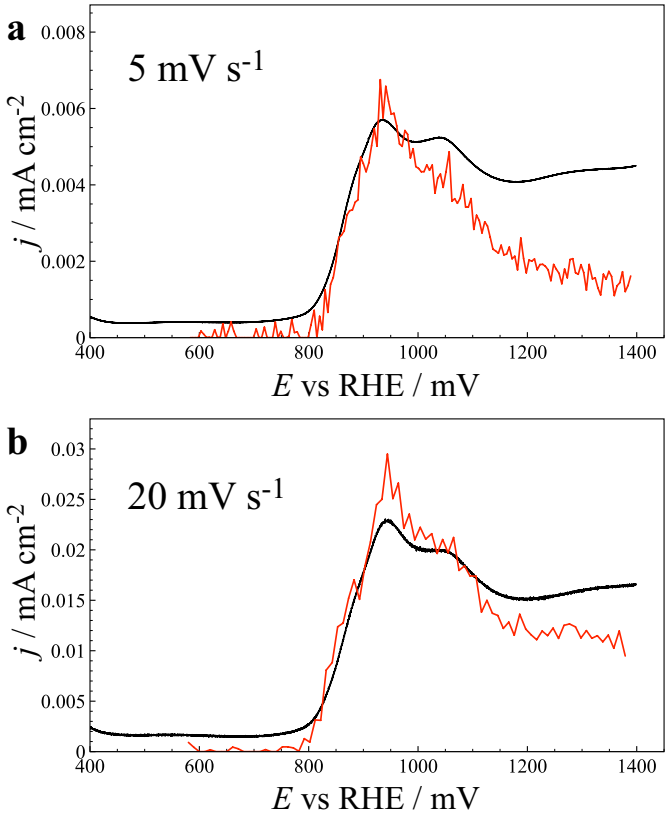

Figure 5.11: Cyclic voltammetry at room temperature with modeled data from charge-transfer resistance for 5 mV s^{-1} (a) and 20 mV s^{-1}. Showing cyclic voltammogram (black), and the estimated current, j_{Rct} (red).

Part II

Microfluidic Flow Cells

6 A semi-analytical method for simulating mass transport at channel electrodes

THOMAS HOLM[a,b], SVEIN SUNDE[a], FRODE SELAND[a], DAVID A. HARRINGTON[b]

[a] *Department of Materials Science and Engineering, Norwegian University of Science and Technology, NO-7491 Trondheim, Norway.*
[b] *Department of Chemistry, University of Victoria, Victoria, British Columbia, V8W 3V6, Canada.*

This chapter is published in Journal of Electroanalytical Chemistry [58].
doi:10.1016/j.jelechem.2015.03.019

Abstract

A method for simulating electrode reactions in channel flow is developed and efficiently implemented in the symbolic algebra program Maple™. The steady-state convective diffusion equation for fully developed 2-D laminar (Poiseuille) flow past one or more electrodes in a channel is considered for a charge-transfer electrode reaction between two soluble species. The case where axial diffusion (along the channel, x direction) is neglected and the diffusivities are equal has an exact solution as an infinite series, in which each term is the product of an exponentials in x and a confluent hypergeometric function in y (across the channel). The practical implementation consists of evaluating a finite number of terms and numerically evaluating the two parameters in each term. Sturm-Liouville (eigenfunction) theory is used to reliably find the parameters for arbitrary values of the rate constants. Comparison is made with results from a commercial software package that uses a finite-element method.

6.1 Introduction

The application of eigenfunction methods for the solution of convective-diffusion equations relevant to electrochemistry has a long history. The solution to the Graetz problem, which solves heat transfer to the walls of a tube with laminar flow, was given as an eigenfunction expansion as early as 1883, and an extensive treatment of the electrochemical version was given by Newman [140]. In the context of mass transport in the rectangular channels that we consider here, Moldoveanu and Anderson solved the limiting current case in terms of a series of parabolic cylinder functions [141]. In these cases, the general case of arbitrary rate constants was not attempted, perhaps because a reliable way of locating the eigenvalues was not available. Recently, Schmachtel and Kontturi used

eigenfunction methods to numerically solve chronoamperometry currents at the rotating disk electrode [142]. They considered the case of arbitrary rate constants and also showed that the case of quasireversible electrode reactions could be solved as easily as the case of irreversible reactions.

Here we apply the eigenfunction expansion method to 2-D steady-state flow past electrodes in a channel, and compare with the more conventional finite-element (FE) method, as implemented in COMSOL Multiphysics®. The eigenfunction solution is a weighted sum of functions, with the functions spanning across the channel and along the electrode. That is, it is a mesh-free method and so should give good accuracy at the beginning of the electrode, where there is a step change in boundary conditions and the current density is high. Furthermore, the concentration profile, once determined, can be easily manipulated term by term to find local current densities, average current densities, or collection efficiencies, without significant degradation in accuracy. The accuracy is determined by the number of terms processed, and calculation of additional terms allows the global error to be estimated. The case where axial diffusion (along the channel) is neglected has an exact solution as an eigenfunction expansion and is investigated here.

6.2 Theory

We consider a solution of the steady-state diffusion-convection problem in a 2-D channel with fully developed laminar (Poiseuille) flow. Notation is given in Fig. 6.1.

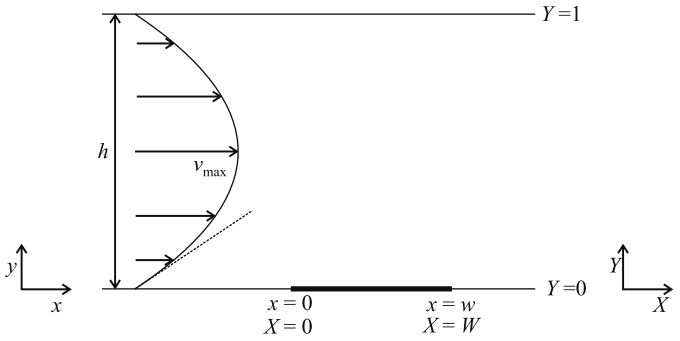

Figure 6.1: Notation. Flow is from left to right, with one or more embedded electrodes (bold) in the bottom of the channel. Lower case variables are dimensioned, upper case variables are dimensionless. The dashed line is the velocity profile (extending to infinite height) for the Lévêque approximation.

The electrode reaction between two solution species, Eq. (6.1), has the current density at a particular location at the electrode given by the usual rate law, Eq. (6.2). The potential at the electrode is fixed, so the rate constants (m s^{-1}) do not vary over the electrode surface. However, we allow the possibility of many electrodes along the wall of the channel, and the potential and rate constants may be different at each. The convective diffusion equation to be solved for each species is Eq. (6.3). We make the common

assumption that the diffusivities of the two species are equal.

$$\mathrm{R} \underset{k_\mathrm{b}}{\overset{k_\mathrm{f}}{\rightleftarrows}} \mathrm{P} + \mathrm{e}^- \tag{6.1}$$

$$j(x) = Fv(x) = Fk_\mathrm{f}c_\mathrm{R}(x,0) - Fk_\mathrm{b}c_\mathrm{P}(x,0) \tag{6.2}$$

$$0 = D\frac{\partial^2 c_i(x,y)}{\partial y^2} - \frac{4v_\mathrm{max}}{h^2}y(h-y)\frac{\partial c_i(x,y)}{\partial x},\ i = \mathrm{R},\mathrm{P} \tag{6.3}$$

Matching of the fluxes at the electrode surface to the reaction rate leads to the boundary conditions, Eq. (6.4), at the electrode surface. (The convective flux at the walls is zero, so only the diffusive part needs to be considered.) The flux at insulating sections between electrodes and at the top of the channel is zero, Eqs. (6.5) and (6.6). The "initial" condition is that the concentrations take the bulk values at a location x_0 upstream of the first electrode, Eq. (6.7). In the absence of axial diffusion, the solution only propagates downstream, and there is no loss in taking $x_0 = 0$. The measured current density is given by averaging over the electrode surface, Eq. (6.8).

$$D\left(\partial c_\mathrm{R}(x,y)/\partial y\right)_{y=0} = -D\left(\partial c_\mathrm{P}(x,y)/\partial y\right)_{y=0} = v(x) \tag{6.4}$$

$$\left(\partial c_\mathrm{R}(x,y)/\partial y\right)_{y=0} = \left(\partial c_\mathrm{P}(x,y)/\partial y\right)_{y=0} = 0 \tag{6.5}$$

$$\left(\partial c_\mathrm{R}(x,y)/\partial y\right)_{y=h} = \left(\partial c_\mathrm{P}(x,y)/\partial y\right)_{y=h} = 0 \tag{6.6}$$

$$c_i(x_0,y) = c_i^\mathrm{b},\ i = \mathrm{R},\mathrm{P} \tag{6.7}$$

$$j_\mathrm{ave} = (FD/w)\int_0^w \left(\partial c_\mathrm{R}(x,y)/\partial y\right)_{y=0}\mathrm{d}x \tag{6.8}$$

As discussed below, the quasireversible solution including the back reaction can be simply derived from the irreversible solution with apparent rate constant $k = k_\mathrm{f} + k_\mathrm{b}$, so we need only develop a numerical method for the irreversible case. We change to dimensionless variables (see Fig. 6.1): $Y = y/h$, $X = x/h$, $W = w/h$, $C(X,Y) = c_\mathrm{R}(x,y)/c_\mathrm{R}^\mathrm{b}$, $K = hk_\mathrm{f}/D$, $J = \left(h/c_\mathrm{R}^\mathrm{b}DF\right)j$ and $A = 4v_\mathrm{max}h/D = 6Pe$ where $Pe = v_\mathrm{av}h/D = 2v_\mathrm{max}h/3D$ is a Péclet number for mass transfer. The convective diffusion equation and boundary conditions are now:

$$0 = \frac{\partial^2 C(X,Y)}{\partial Y^2} - A\,Y(1-Y)\frac{\partial C(X,Y)}{\partial X} \tag{6.9}$$

$$\left(\partial C(X,Y)/\partial Y\right)_{Y=0} = KC(X,0)\ \text{(at electrode)} \tag{6.10}$$

$$\left(\partial C(X,Y)/\partial Y\right)_{Y=0} = 0\ \text{(between electrodes)} \tag{6.11}$$

$$\left(\partial C(X,Y)/\partial Y\right)_{Y=1} = 0\ \text{(top of channel)} \tag{6.12}$$

$$C(0,Y) = 1\ \text{(upstream)} \tag{6.13}$$

Writing $C(X,Y) = F(X)G(Y)$ and rearranging gives Eq. (6.14), which shows that the partial differential equation is separable. The general solution, Eq. (6.15), is a

superposition of products of exponential functions of X and functions of Y that satisfy the differential equation (6.16), where the primes indicates differentiation with respect to Y.

$$\frac{1}{Y(1-Y)G(Y)}\frac{\mathrm{d}^2G(Y)}{\mathrm{d}Y^2} = \frac{A}{F(X)}\frac{\mathrm{d}F(X)}{dX} = -b^2 \tag{6.14}$$

$$C(X,Y) = \sum_{i=1}^{\infty} a_i \exp(-b_i^2 X/A) G_i(Y) \tag{6.15}$$

$$-G''(Y) = b^2 Y(1-Y)G(Y) \tag{6.16}$$

Eq. (6.16) has an operator $-d^2/dY^2$ operating on $G(Y)$ to give a constant b^2 times a weighting function $Y(1-Y)$ times $G(Y)$. According to Sturm-Liouville theory [143], such equations have an infinite set of eigenfunction solutions, $G_i(Y)$, which depend on the boundary conditions at the electrode and top channel surfaces. The eigenvalues are the particular values b_i^2 that give valid solutions. As detailed in 6.7, we first narrow the solutions to those that satisfy the zero-flux boundary condition at the top of the channel, Eq. (6.17). This ensures that the concentration, Eq. (6.15), satisfies the zero-flux condition, Eq. (6.12). These solutions $G(Y)$, normalized so that $G(1) = 1$, are given in terms of confluent hypergeometric functions in Appendix A (in this chapter).

$$G'(1) = 0 \tag{6.17}$$

The remaining undetermined constant is b, which is determined by the type of boundary condition at the $Y = 0$ surface, i.e., the electrode surface or an insulating surface between electrodes. Three subcases are considered. The first is the limiting current boundary condition, where the concentration is zero at the electrode surface, Eq. (6.18). Solving Eq. (6.18) for b leads to the series of values in Eq. (6.19).

$$G(0) = 0 \tag{6.18}$$

$$b_1^{(\infty)} = 3.82, b_2^{(\infty)} = 11.90, b_3^{(\infty)} = 19.92, ... \tag{6.19}$$

$$b_i^{(\infty)} \sim \frac{\pi(i-\frac{1}{2})}{\int_0^1 \sqrt{Y(1-Y)}dY} = 8\,(i-1/2) \tag{6.20}$$

$$8\,(i-1) < b_i^{(\infty)} < 8\,(i-1/2)\,,\ i = 1, 2, \ldots \tag{6.21}$$

where the superscript ∞ denotes an infinite rate constant ($K = \infty$). Eq. (6.20) for the eigenvalues[1] is from Sturm-Liouville theory [143], and although it is an asymptotic formula for large i, closer inspection shows that it works well also for small i: the predicted values $8(i-1/2)$ are slightly higher than the actual values in Eq. (6.19).. Successive b_i values are in the ranges given in Eq. (6.21), which means that the numerical

[1]We refer to the b_i values as eigenvalues, though strictly these are the square roots of the eigenvalues.

solver can reliably find all eigenvalues by searching for one solution of Eq. (6.18) in each of these ranges.

Consider now the boundary condition for an insulating section of the channel or for zero current at the electrode, where the flux is zero, Eq. (6.22). Here the eigenvalues are given by Eq. (6.23).

$$G'(0) = 0 \tag{6.22}$$

$$b_i^{(0)} = 0, 9.05, 17.15, 25.19, ... \sim 8(i-1) \tag{6.23}$$

The last case is the Robin boundary condition of Eq. (6.24), where K is a dimensionless rate constant. Here the eigenvalues satisfy the inequalities of Eq. (6.25).

$$G'(0) - KG(0) = 0 \tag{6.24}$$

$$8(i-1) < b_i^{(0)} < b_i^{(K)} < b_i^{(\infty)} < 8\,(i-1/2) \tag{6.25}$$

For all cases, b_i lies between $8(i-1)$ and $8(i-1/2)$. (For negative K, a nonphysical case, the b_i values lie between $8(i-1/2)$ and $8i$.)

The coefficients a_i are determined by the "initial" concentration profile at $X = 0$, the upstream edge of the electrode. From Eq. (6.15), a given initial profile $C(0, Y) = f_0(Y)$ (not necessarily $C(0, Y) = 1$) is a linear combination of the eigenfunctions $G_i(Y)$, and the coefficients can be found using the orthogonality of the eigenfunctions as

$$a_i = \frac{\int_0^1 Y(1-Y) f_0(Y) G_i(Y)\,\mathrm{d}Y}{\int_0^1 Y(1-Y) G_i(Y)^2\,\mathrm{d}Y} \tag{6.26}$$

Once the numerical values of the a_i and b_i have been calculated for the chosen number of terms N, the series form of the concentration, Eq. (6.15), is easy to manipulate. For example, the dimensionless form of the current density, Eq. (6.8), averaged over an electrode running from $X = 0$ to $X = W$ is

$$J_{\text{av}} = \frac{1}{W} \int_0^W \left.\frac{\partial C}{\partial Y}\right|_{Y=0} \mathrm{d}X \tag{6.27}$$

(This is also a dimensionless average flux.) It may be calculated term by term as

$$J_{\text{av}} = \frac{A}{W} \sum_{i=1}^{\infty} \frac{a_i}{b_i^2} \left[1 - \exp(-b_i^2 W/A)\right] G_i'(0) \tag{6.28}$$

where $G_i'(0)$ may be evaluated using the differentiation rule Eq. (6.42).

6.2.1 Multiple electrodes

The case of multiple electrodes and gaps between them is handled similarly. The solution for the first electrode proceeds as described above, with $f_0(Y) = 1$. This solution at the downstream edge of the electrode is just used as the initial profile that replaces $f_0(Y)$ in the solution of the next "segment". For example, a three-segment configuration might have segment 1 as an electrode between $X = 0$ and $X = 1$, segment 2 as an insulator between $X = 1$ and $X = 2$ with a no-flux boundary condition at $Y = 0$ and then segment 3 as an electrode after $X = 2$. The segment 1 solution $C(1, Y) = f_1(Y)$ is used as the initial profile for segment 2, and the segment 2 solution $C(2, Y) = f_2(Y)$ is used as the initial profile for segment 3.

6.3 Methods

6.3.1 Maple

A procedure *chsolve* to implement the above algorithm was written in the symbolic algebra system Maple™[57]. The code and examples of its use are available as supplementary material, see Appendix B (in this chapter). The procedure takes as inputs: (i) the numerical value of the dimensionless rate constant. As above, "0" indicates the zero flux condition and "infinity" indicates the case of zero concentration at the electrode surface, (ii) the name of a procedure that evaluates the initial concentration profile $f_0(Y)$, (iii) the value of A, and (iv) the number of terms N required in the eigenfunction expansion, Eq. (6.15). The output is a procedure that evaluates the dimensionless concentration as a function of X and Y, which can then be plotted, differentiated or otherwise manipulated to produce derived quantities.

The case of multiple segments is handled by giving the rate constant as a piecewise function of X. In the single segment case, A can be left as a symbol, and then the output concentration and quantities derived for it can be plotted as a function of A. For the multisegment case, the numerical value of A must be given; this restriction arises from the need to numerically evaluate the integrals in Eq. (6.26) to find the concentration profile at the beginning of second and subsequent segments.

The limiting factor is the efficient numerical calculation of the integrals in Eq. (6.26). When the accuracy requested (via the "Digits" variable) is low, Maple works in hardware double precision arithmetic and uses the Numerical Algorithms Group routine "d01akc". For higher accuracy, Maple works in arbitrary precision arithmetic, and uses an adaptive Gaussian quadrature routine "Gquad".

6.3.2 Comsol

The case of a single electrode of width $W = 1$ under limiting current conditions was also solved using COMSOL Multiphysics® [144], with the conditions chosen as close as possible to those used in Maple. To effectively non-dimensionalize the problem, the

problem was solved in base SI units with the parameters h, w, D and c^{b} set to unity. The problem was solved for both species using the PARDISO solver, and the A value was changed parametrically to get the solution at different flow rates. The outlet was put 10 electrode widths downstream of the electrode to eliminate the influence of the boundary condition. The outlet boundary condition is given in Eq. (6.29).

$$D_i \frac{\partial c_i}{\partial x} = 0 \tag{6.29}$$

To solve for the limiting current case, the rate constant K was set to a high value (10^{10}) to effectively get a concentration of zero at the electrode. The surface concentration was verified post-calculation to be zero. Comsol does not allow the concentration at a point to have two values, as is the case for Maple at the upstream edge of the electrode. To solve the problem as closely as possible to the Maple solution, the start of the geometry was set to 1/16000 of the electrode width upstream of the electrode. Here, the concentration was set to the inlet concentration, $C = 1$. This gives one mesh point (geometry determined) in distance between the concentration of 1 at the inlet to the concentration of 0 at the electrode start. The absence of axial diffusion was achieved by using anisotropic diffusivities with zero X components.

The standard triangular meshing was used. A fine mesh was used at the inlet and along the electrode surface. This was set to 1/500 of the dimensionless diffusion layer thickness $\Delta = \delta/h$ estimated in the Lévêque approximation as Eq. (6.30).

$$\Delta = 2.83\,(W/A)^{1/3} \tag{6.30}$$

for $A = A_{\max}$, where $A_{\max}$ is the highest A value that is evaluated. The mesh was allowed to grow at a rate of 5% out from the inlet and electrode surface.

6.4 Results

Examples of the capabilities of this method are given here, with the calculation details given in a Maple worksheet in the supplementary material, see Appendix B (in this chapter) and Appendix A.

6.4.1 Irreversible Reaction

The case of $K = K_{\mathrm{f}} = 10$ for $A = 100$ (Péclet number 16.7) is illustrated in Fig. 6.2. The consumption of the species at the electrode is seen, and its variation along the electrode surface. The increasing thickness of the diffusion layer is also evident, and by $X = 2$, the concentration at the top of the channel is significantly diminished from its initial value of 1. Small ripples in the Y direction close to $X = 0$ are the Gibbs' phenomenon, well known in Fourier theory, which is a special case of the Sturm-Liouville theory applicable here.

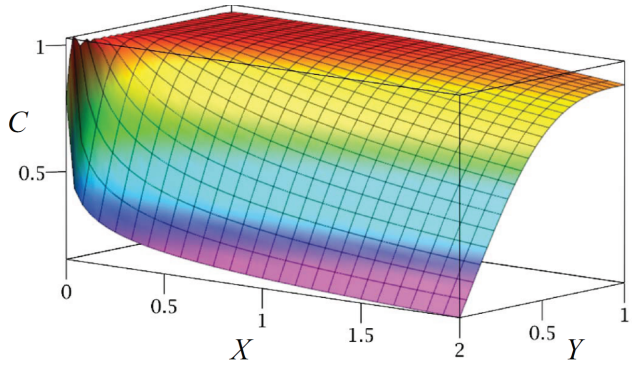

Figure 6.2: Concentration profile for an irreversible reaction. $K_{\mathrm{f}} = 10$, $A = 100$. Series evaluated to 40 terms.

6.4.2 Flow rate dependence of limiting current

The limiting current density is found from the flux via Eq. (6.28), for the case of the boundary condition $C(X, 0) = 0$ or Eq. (6.18). The series in Eq. (6.28) has numerical values of the a_i and b_i but A and W are still arbitrary, and so the limiting current as a function of flow rate may be readily plotted and compared with the Comsol results as in Fig. 6.3. For comparison, two approximate relationships are also shown: (i), the limiting current given by the Levich equation, Eq. (6.31), and (ii), the complete consumption or "thin layer" limit, Eq. (6.32).

$$J_{\mathrm{av}}(\mathrm{Levich}) = \left(3^{4/3}/2\Gamma\left(1/3\right)\right)(A/W)^{1/3} \tag{6.31}$$

$$J_{\mathrm{av}}(\text{thin layer}) = A/6 = Pe \tag{6.32}$$

The Levich equation for limiting current assumes not only the absence of axial diffusion, but also the Lévêque approximation for the velocity profile (see Fig. 6.1). The Lévêque approximation is valid only when the diffusion layer thickness is small compared to the channel height, i.e., the concentration changes only near the electrode surface. This approximation applies at high flow rates. The current density tends to zero as A tends to zero at fixed W as predicted by Eq. (6.28). At the lowest flow rates, the reactant is completely consumed before it reaches the downstream edge of the electrode. In this case the total moles reacting per second at the electrode must equal the total moles per second entering the channel, which leads to the thin layer limit of Eq. (6.32). The behavior and comparison of the curves is further discussed below.

6.4.3 Quasireversible reactions

For the case where the redox reaction, Eq. (6.1), is quasireversible with rate law Eq. (6.2), we define a dimensionless product concentration, S, Eq. (6.33), and nondimensionalize

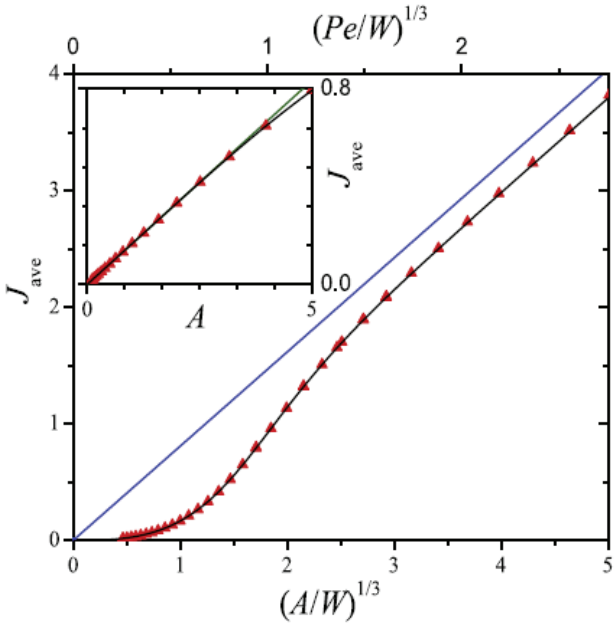

Figure 6.3: Current density dependence on flow rate. Limiting current ($C = 0$) boundary condition, for $W = 1$. $A = 6Pe$ is a dimensionless flow rate. Comparison of Maple 40 term eigenfunction solution (black line) and Comsol solution (red triangles). Main figure compares these with the $A^{1/3}$ dependence of the Levich approximation (blue line, Eq. (6.31)); inset compares with complete consumption approximation (green line, Eq. (6.32)).

the other quantities similarly to before. We assume the diffusivities are equal and that the product concentration is initially zero.

$$S = c_{\mathrm{P}}/c_{\mathrm{R}}^{\mathrm{b}} \tag{6.33}$$

$$\begin{aligned} -\left(\partial S(X,Y)/\partial Y\right)_{Y=0} &= \left(\partial C(X,Y)/\partial Y\right)_{Y=0} \\ &= \left(hk_{\mathrm{f}}/D\right) C(X,0) - \left(hk_{\mathrm{b}}/D\right) S(X,0) \\ &= K_{\mathrm{f}} C(X,0) - K_{\mathrm{b}} S(X,0) \end{aligned} \tag{6.34}$$

For the case of equal diffusivities, the principle of unchanging total concentration applies [145], which means that $c_{\mathrm{R}} + c_{\mathrm{P}} = c_{\mathrm{R}}^{\mathrm{b}}$ everywhere in the channel, or equivalently $S(X,Y) = 1 - C(X,Y)$. Under this condition, it is possible to easily derive the quasireversible solution from the irreversible one [146]. This means that only one mass-transport problem needs to be solved. The quasireversible concentrations are given by Eqs. (6.35) and (6.36), where $C_{\mathrm{ir}}^{(K_{\mathrm{f}}+K_{\mathrm{b}})}$ means the solution to the irreversible problem with rate constant $K_{\mathrm{f}} + K_{\mathrm{b}}$.

$$C(X,Y) = \left(K_{\mathrm{f}} C_{\mathrm{ir}}^{(K_{\mathrm{f}}+K_{\mathrm{b}})}(X,Y) + K_{\mathrm{b}}\right)/\left(K_{\mathrm{f}} + K_{\mathrm{b}}\right) \tag{6.35}$$

$$S(X,Y) = 1 - C(X,Y) \tag{6.36}$$

That is, the eigenfunction solution is found for the boundary condition of Eq. (6.24) with $K = K_{\mathrm{f}} + K_{\mathrm{b}}$, and then substituted into Eqs. (6.35) and (6.36). Eq. (6.27) then gives the quasireversible current density. Examples of steady-state current potential curves calculated in this way are given in Fig. 6.4.

If the product is initially present with concentration $c_{\mathrm{P}}^{\mathrm{b}}$, then $c_{\mathrm{R}}^{\mathrm{b}}$ is replaced by $c_{\mathrm{P}}^{\mathrm{b}} + c_{\mathrm{R}}^{\mathrm{b}}$ in the definitions of C and S and the revised rule is given by Eq. (6.37), where $f = c_{\mathrm{R}}^{\mathrm{b}}/(c_{\mathrm{P}}^{\mathrm{b}} + c_{\mathrm{R}}^{\mathrm{b}})$. An example is given in the supplementary material.

$$C(X,Y) = \frac{C_{\mathrm{ir}}^{(K_{\mathrm{f}}+K_{\mathrm{b}})}(X,Y)\left(fK_{\mathrm{f}} - (1-f)K_{\mathrm{b}}\right) + K_{\mathrm{b}}}{K_{\mathrm{f}} + K_{\mathrm{b}}} \tag{6.37}$$

6.4.4 Collection efficiency

The collection efficiency may be determined by considering flow of reactant solution initially without product past an upstream electrode where the reaction produces product under limiting current conditions. The solution then flows past a gap and then past a downstream electrode that reduces product back to reactant under limiting current conditions. The collection efficiency is calculated as the ratio of the current at an downstream electrode to the current at the upstream electrode.

To implement this, first a two-segment calculation is carried out for the reactant concentration C with boundary condition $K = \infty$ ($C = 0$) for the first segment (upstream electrode) and $K = 0$ (zero-flux) for the second segment (gap between the two electrodes). The product concentration S at the end of the second segment is calculated as

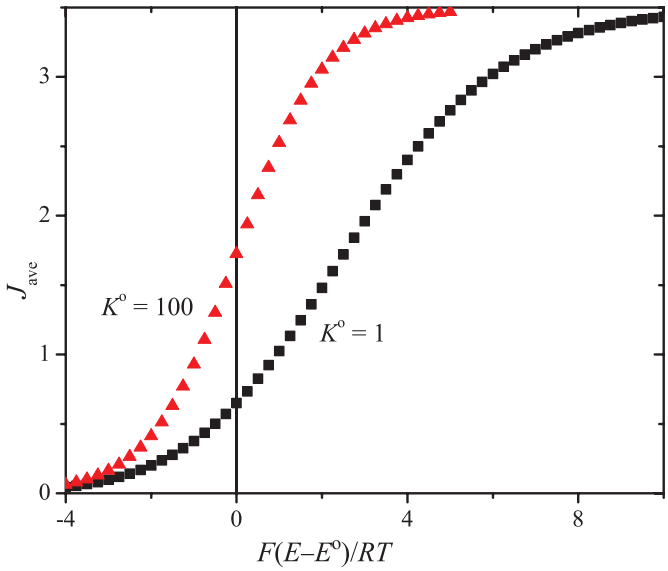

Figure 6.4: Steady-state current potential curves. Quasireversible reaction, $\beta = 0.5$ $W = 1$, $A = 100$, 40 terms. Curves shown for two values of the dimensionless rate constant K^o.

$1 - C$ under the assumption that the diffusivities are equal, and this is then used as the initial concentration profile for the calculation of the concentration S for the third segment (second electrode) with boundary condition $K = \infty$ ($S = 0$). Integration of the local current densities over the two electrodes gives the two currents, whose ratio is the collection efficiency. Fig. 6.5 shows an example where the electrode widths and the gap are all equal and $A = 100$. This collection efficiency here, 0.295, is higher than the value using the standard calculation, 0.250, which assumes the Lévêque approximation [54]. This is because at this flow rate, a significant amount of the product has diffused across the channel, and its reflection back enhances the collection efficiency.

6.5 Discussion

6.5.1 Accuracy and convergence

The limiting current case is the most difficult of the cases from a numerical point of view, and so we begin with a discussion of the results in Fig. 6.3. The Comsol results, intended as a verification strategy, do not agree with the Maple results using 40 terms. Increasing to 100 terms makes only a 0.3% difference at the highest flow rate shown on the plot. There appears to be a constant systematic error in the Comsol results. This is confirmed by looking at the low flow rate regime, where the Maple behavior correctly gives $J_{av} = A/6$, but Comsol has a constant offset, and does not go to zero at zero flow rate, which is the correct limit in the absence of axial diffusion. This is attributed to use

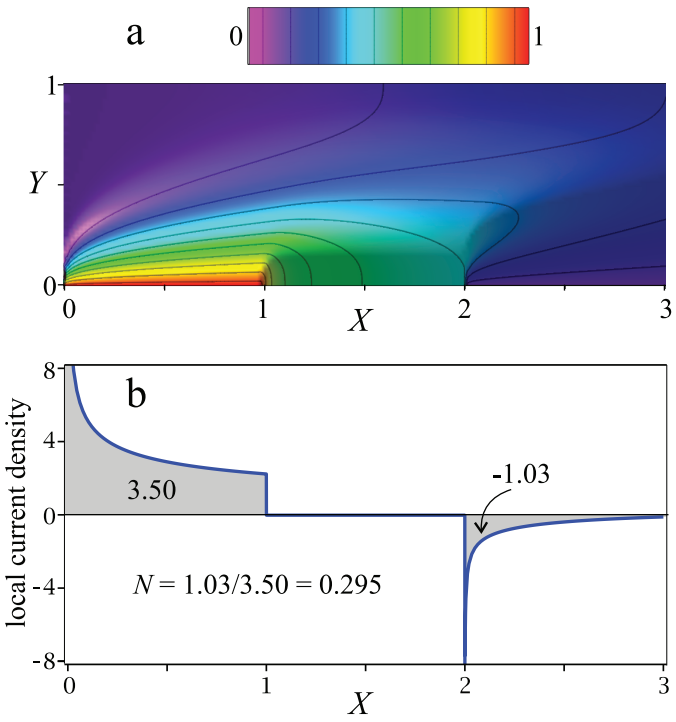

Figure 6.5: Collection efficiency calculation. (a) Concentration of product. Limiting current production at electrode between $X = 0$ and $X = 1$ and limiting current consumption at electrode between $X = 2$ and $X = 3$ (40 term calculation). Contours are at 0.05, 0.15, ..., 0.95. (b) Local dimensionless current density along the channel, and calculation of efficiency from the shaded areas.

of a triangular mesh with edges that do not align with the X and Y directions, and lead to a small amount of "numerical diffusion" in the X direction even when axial diffusion was nominally precluded. Use of a rectangular mesh aligned with the X and Y directions was attempted to solve this problem, but expanding meshes do not maintain alignment and fixed fine meshes run into memory limitations, and so this strategy was not pursued further.

Convergence issues of the eigenfunction method did become significant at higher flow rates than shown in Fig. 6.3, where the separation from the Levich line increased. Increasing the number of terms improved the situation, in that the point of divergence was delayed to higher flow rates, but ultimately it is simply more accurate to use the Levich formula.

For the more general case of finite rate constants, the accuracy of the method was investigated over a wide parameter space. A criterion for adequate convergence was taken as less than 0.1% change on increasing the number of terms by 10. It is difficult to prove that this represents absolute convergence, but it enables the trends to be found, and gives reasonable confidence that the results are correct at the 1% level. Parameters investigated were: (i) K from 10^1 to 10^7 by factors of 10, and ∞, (ii) numbers of terms from 10 to 100 in steps of 10, (iii) A values from 1 to 10^5 in a 1-3-10 sequence. This study led to the following conclusions:

1. Convergence is easier to reach (at a lower number of terms) for lower K values.
2. Convergence is faster at lower A values and/or lower K.
3. For $K \geq 10^5$, the results for 10 or more terms are all within 0.1% of the $K = \infty$ value.
4. For a given K value, the change from 90 to 100 terms leads to less than 0.1 % change for all A values except for the two largest. The two largest A values only reach this criteria for the two smallest K values.
5. The calculation time is mainly dependent on the number of terms used (and less on the K or A value), but this effect is small enough that 100 terms can be practically calculated as a matter of routine. The calculation time for 100 terms was comparable to the Comsol calculation time.

Although Maple allows for arbitrary precision calculations, the hardware double precision calculations were found to be sufficient for 100 term calculations, i.e., the accuracy is limited by the number of terms and not the accuracy of the calculation engine.

For multisegment calculations, the calculation time for second and subsequent segments was significantly higher than for the first segment, because of the large number of hypergeometric function evaluations needed in the integrals in the a_i coefficients, Eq. (6.26). This can be remedied by numerically fitting the concentration profile at the end of a segment to a suitable function, and using that as the initial concentration profile for the next segment. Strictly, this means that the guarantee of higher accuracy with more

terms (provided by Sturm-Liouville theory) is invalidated. However, least-squares fitting of the concentration profile at 101 points across the channel to a degree 10 polynomial decreased the calculation time for the second segment to approximately the same time as the first segment without a noticeable change in accuracy (see the collection efficiency calculation in the supplementary material).

6.5.2 Method assessment

Most analytical solutions for concentrations or currents in channel electrodes have used the Lévêque approximation, and neglected axial diffusion, e.g., these are standard approximations in calculating collection efficiencies [54, 55, 147]. These approximations work best at fast flow rates and large channel heights. There has been some consideration of the effects of axial diffusion [140, 148–150], and more recently Amatore and coworkers [151] have mapped out the zone diagram for the various limiting and intermediate cases in terms of the parameters W and Pe. The present work neglects axial diffusion but goes beyond the Lévêque approximation and considers the full velocity profile across the channel. Axial diffusion may be neglected when the time to diffuse axially along the electrode is long compared to the times to diffuse across the channel or to flow past the electrode, leading to $W \gtrsim 1$ and $W \cdot Pe \gtrsim 1$. The latter condition covers zone II in Amatore's notation, which is the largest region in the $W - Pe$ plane, and is defined as where neither of the approximations (6.31) or (6.32) apply. The condition $W \gtrsim 1$ and the poor convergence at very high Pe further restrict the region of validity somewhat, but there remains a region of intermediate flow rates and small channel heights where the present algorithm is practical. The collection efficiency calculation above (Sec. 6.4.4) indicates that the error in using the Lévêque approximation for small channel heights can be significant.

The present work indicates that solving for the case of the full parabolic velocity profile across the channel is not significantly more difficult than the Lévêque approximation. Like the semidifferentiation approach of Oldham for planar electrodes [152], the present method first exactly solves the problem across the channel and thereby reduces the problem to solving along the near surface of the channel. It is to be emphasized that the eigenfunction expansion is an exact solution to the problem without axial diffusion, and the only approximation arises from the need to solve for the eigenvalues and coefficients numerically, and to terminate the series after a finite number of terms.

There are standard methods for using eigenfunction expansions that may be used in problems that include axial diffusion, i.e., for elliptic partial differential equations [153], which will be explored in subsequent work. That is, the present confluent hypergeometric functions may be a suitable basis set for the more general case, but the complexity of the method will be significantly greater, and an iterative method may be required.

In terms of a numerical method, the eigenfunction expansion method does not use a mesh and so does not have the complication of creating and validating meshes that FE or finite-difference methods have. Such methods need finer meshes near electrodes and electrode edges. On the other hand, eigenfunction expansion methods are known

for slow convergence. Perhaps not surprisingly, we find that the conditions that require a fine, adaptive mesh for FE solution (such as large flow rates), are also the conditions that require more terms for acceptable convergence in our method. Accurate convergence was possible for comparable computational expense as for the FE method, but the present method is algorithmically much simpler and the global error is more easily assessed. An important advantage of the present method is that a whole segment is solved at one time, so the complexity of the calculation is largely independent of the channel height or width of the electrode.

In principal the present method did not require a symbolic algebra system for its implementation. Such systems allow arbitrary precision calculations, but this feature was not found to be necessary here. These systems do have an important advantage in processing the concentration profile into the required measurable quantities, such as average current density or collection efficiency. This processing typically involves differentiation or integration, which is done exactly by simple rules such as the differentiation rule (6.42), and does not degrade the accuracy of the calculation.

Another advantage of these systems is that the numerical evaluation of the hypergeometric and exponential functions in the solution is deferred until they are needed. In Fig. 6.2, for example, Maple's plot routine decides where to evaluate the concentrations, using more points in steeper regions of the plot. The numerical evaluation of these concentrations occurs in the plot routine itself, and not in the construction of the series solution. Therefore, there is no need for evaluate the solution over a fine grid of points just in case they might be required later. This is perhaps seen most clearly in the case of a single electrode, where the limiting current can be given as a function of an unspecified A, and then this function is used to create Fig. 6.3.

6.6 Conclusions

The eigenfunction method developed here is computationally efficient, and is accurate in its domain of validity. It can find concentrations, current densities and derived quantities for any values of the rate constant, and can be used for multiple electrodes in a channel. Although convergence is slower in cases where a finite element method would require fine adaptive meshes, avoiding the need to determine and validate a mesh is a distinct advantage. Implementation in a symbolic algebra system gives flexibility in manipulating the derived quantities without degrading accuracy. Coupled with the advances in computing speed, the advantages of symbolic algebra programs mean that reconsideration of algorithms such as the eigenfunction method demonstrated here can lead to competitive numerical methods with high accuracy that are simple to implement.

6.7 Acknowledgments

Financial support from the Natural Sciences and Engineering Research Council of Canada (discovery grant 37035), the Research Council of Norway (project 221899), the Univer-

sity of Victoria and the Norwegian University of Science and Technology (NTNU) is gratefully acknowledged. T.H. thanks NTNU for the award of a scholarship. D.A.H. thanks Sönke Schmachtel for useful discussions.

Appendix A: Solution of ODE for $G(Y)$

The differential equation (6.16) has the general solution Eq. (6.38) with two arbitrary constants g_1 and g_2.

$$G(Y) = g_1 G_1(Y) + g_2 G_2(Y) \tag{6.38}$$

$$G_1(Y) = \exp\left(bY(1-Y)/2\right)$$

$$\times\ {}_1F_1\left(1/4 - b/16; 1/2; b(2Y-1)^2/4\right) \tag{6.39}$$

$$G_2(Y) = \exp\left(bY(1-Y)/2\right)(2Y-1)$$

$$\times\ {}_1F_1\left(3/4 - b/16; 3/2; b(2Y-1)^2/4\right) \tag{6.40}$$

Other notations for the confluent hypergeometric functions ${}_1F_1\left(a; b; z\right)$ are ${}_1F_1\left(; z\right)$ or $M(a, b, z)$ [154]. It is evident that $G_1(Y)$ is symmetric (even) about $Y = 1/2$ and $G_2(Y)$ is antisymmetric (odd) about this point. Applying the no-flux boundary condition at the top of the channel, $G'(1) = 0$, allows determination of one of the constants, and the other is chosen to scale the functions so that $G(1) = 1$, with the result Eq. (6.41). This contains the constant b, which is determined from the electrode boundary condition as described in the main text.

$$G(Y) = \frac{G_2'(1)G_1(Y) - G_1'(1)G_2(Y)}{G_2'(1)G_1(1) - G_1'(1)G_2(1)} \tag{6.41}$$

Derivatives are evaluated using the rule (Ref. [154], Eq. 13.3.15)

$${}_1F_1\left(c; d; f(Y)\right)' = \frac{c}{d}\,{}_1F_1\left(c+1; d+1; f(Y)\right) f'(Y) \tag{6.42}$$

According to Sturm-Liouville theory, the eigenfunctions $G_i(Y)$ for different values of b_i that satisfy the boundary conditions are orthogonal with respect to the weight function $Y(1-Y)$:

$$\int_0^1 Y(1-Y)G_i(Y)G_j(Y)\,\mathrm{d}Y = 0,\ i \neq j \tag{6.43}$$

Appendix B: Supplementary material

A version of the Maple worksheet utilized is given in the Appendix A, and a description of the Comsol setup is given in Appendix B for the three times Comsol was used in this work: (1) calculating the steady-state non-dimensional currents for A-values, (2) solving the collection efficiency for the stated problem and gives the value used in Section 6.4.4, (3) solving the dimensionless current for the quasi-reversible example with $K = 10$ giving the current of 2.1817 in Section 6.4.1.

7 Mass-transport impedance at channel electrodes: Accurate and approximate solutions

THOMAS HOLM[a,b], MATS INGDAL[a,b], ESPEN V. FANAVOLL[a,b], SVEIN SUNDE[a], FRODE SELAND[a], DAVID A. HARRINGTON[b]

[a] *Department of Materials Science and Engineering, Norwegian University of Science and Technology, NO-7491 Trondheim, Norway.*
[b] *Department of Chemistry, University of Victoria, Victoria, British Columbia, V8W 3V6, Canada.*

This chapter is published in Electrochimica Acta [60].
doi:10.1016/j.electacta.2016.03.096

Abstract

Accurate numerical electrochemical impedance spectra at channel electrodes are obtained using commercial finite element method software. These agree with experimental measurements on the hexaammineruthenium(II/III) reversible redox couple. The numerical solutions are used as a benchmark to test the validity of some common analytical approximations for the mass-transport impedance.

7.1 Introduction

Improved microfluidic fabrication methods have led to a resurgence of devices using channel flow electrodes [155], and it is important to quantitatively understand the mass transport in these systems. Channel electrodes do not have uniform accessibility, which makes them mathematically more difficult than the analogous rotating disk electrode (RDE). One approach is use to the finite element method (FEM) to give accurate numerical solutions, and its implementation in the program COMSOL Multiphysics® [59] has found wide use in electrochemistry [156]. Another approach to accurate solutions is to use semianalytic methods, which have recently been used for band electrodes with and without flow [58, 157, 158]. More commonly, approximations are applied to get simplified analytical expressions: (i) axial diffusion (in the channel direction) is neglected, and/or (ii) the Lévêque approximation is applied, i.e., the velocity profile is assumed to be linear.

Electrochemical impedance spectroscopy is well known as a powerful method for studying electrode processes, but the convective-diffusion problem under a.c. conditions must be properly understood in order to make progress. Even for the much-studied RDE,

the convective-diffusion impedance is typically modeled by approximate analytical solutions, sometimes with different expressions for high and low frequency regions [159–164], and comparison of these with numerical solutions is available, e.g., [165, 166]. For channel electrodes, the two above-mentioned approximations have been used to get analytical treatments [167–170]. Alternatively, convection has been neglected altogether [171]. Approximate and experimental treatments of higher harmonics have also been reported [172]. Comparisons of approximate treatments with experiment have typically been restricted to the regimes where the approximations are valid. Experiments and theory are lacking in some important parameter regimes, in particular for low flow rates and low-height channels.

There is therefore the need for accurate numerical impedance solutions for channel electrodes. These can be directly compared with experiment, or can be used to establish the validity of various approximate analytical methods. Both of these objectives are achieved here, where we compare numerical solutions from Comsol with experiment and literature approximations, for the simple redox reaction, Eq. (7.1).

$$\mathrm{R} \rightleftharpoons \mathrm{P} + n\mathrm{e}^- \tag{7.1}$$

The experiments used the $\mathrm{Ru^{II}/Ru^{III}}$ hexaammine redox couple with $n = 1$. Only a few FEM simulations of impedance have been reported before, e.g., [173, 174], none of which treat channel electrodes.

7.2 Methods

7.2.1 Microfluidics

The microfluidic flow cells, Fig. 7.1, were made in the NorFab facilities (Trondheim, Norway). The electrodes were prepared on clean glass slabs by a photoresist method using ma-405 photoresist and ma-D331/s developer (Micro Resist Technology GmbH). Titanium (10 nm) and platinum (190 nm) were evaporated onto the developed glass slides (Pfeiffer Vacuum Classic 500) and excess metal was removed with mr-REM 600 (Micro Resist Technology GmbH).

The PDMS channels were made from a channel master on a Si slide. The master was fabricated by applying photoresists SU8-5 and SU8-2100 (both MicroChem Corp.), developing the pattern, and removing excess material with Mr-DEV 600 (Micro Resist Technology GmbH). The wafer was then hard baked. The PDMS was made by mixing base (Lindberg and Lund AS) and curing agent (Dow Corning S.A). The mixture was degassed and poured on top of the Si master. The finished PDMS channel was assembled by making inlet and outlet holes, activating the surface using a plasma cleaner, and then mounting on the electrode glass slide.

Wires were connected by soldering, and a reservoir for collecting the electrolyte and holding the external reference electrode was added, see Fig. 7.1. The cells produced had 100 μm wide electrodes in a 100 μm high channel with a depth of 1 mm.

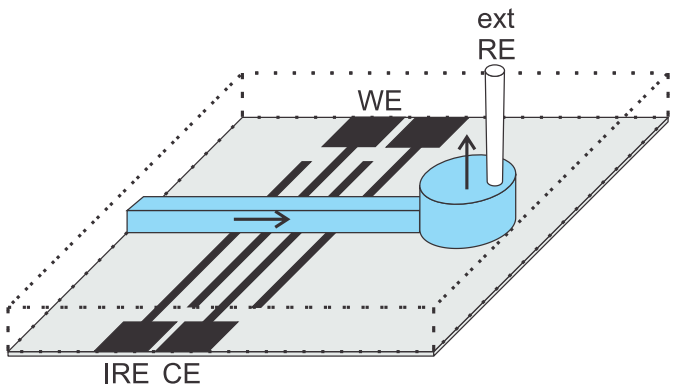

Figure 7.1: Diagram of the cell. Channel and outlet reservoir shown in blue, with arrows showing the fluid flow direction. IRE and ext RE are the internal and external reference electrodes.

7.2.2 Electrochemistry

To avoid oxygen, the microfluidic cell was mounted in a chamber that was purged with argon (Praxair Ultra High Purity 5.0). The absence of oxygen was confirmed by cycling the electrode between oxygen evolution and hydrogen evolution in 0.5 M H_2SO_4 (Seastar Chemicals, Baseline grade). Solutions were made up with Millipore Milli-Q water. All electrochemistry was performed with a Gamry Ref. 600 potentiostat. The external reference electrode used during electrochemistry in 0.5 M H_2SO_4 was a reversible hydrogen electrode mounted in the outlet reservoir, which consisted of a Pt wire sealed in glass and exposed to the solution and a trapped hydrogen bubble.

To further minimize the effect of oxygen, an iodine monolayer was deposited on the electrodes by holding at 0.4 V vs RHE for 6 minutes in 0.5 M H_2SO_4 + 4 mM KI ($\geq$ 98.5% Caledon) electrolyte. The quality of the iodine layer was checked using cyclic voltammetry (CV) in H_2SO_4, by comparing the magnitude of the capacitive current between 0.3 and 0.7 V vs RHE. The layer was deemed sufficient if the capacitive current had dropped to below 0.01 mA cm^{-2} for a scan rate of 200 mV s^{-1}.

The data reported in this paper used the reversible Ru^{II}/Ru^{III} hexaammine redox couple. The aqueous solution was prepared from nominally 5 mM $Ru^{II}(NH_3)_6Cl_2$ ($\geq$ 98% Sigma-Aldrich) and 5 mM $Ru^{III}(NH_3)_6Cl_3$ ($\geq$ 99.9% Sigma-Aldrich) in 0.1 M K_2SO_4 electrolyte ($\geq$ 99.5% AnalaR). The ruthenium hexaammine complexes degrade if there is oxygen present in the solution, and so argon was purged for 10 minutes before the complexes were introduced, and then purged again after introduction. The electrolyte was always made fresh on the day of the experiments and properly stored to avoid oxygen introduction. Despite this, slight degradation of ruthenium hexaammine did occur, and the actual concentrations were estimated as 4.0 mM by adjusting the Comsol modeled results to give a satisfactory fit for all flow rates.

The Ru^{II}/Ru^{III} hexaammine redox couple was used as an internal reference electrode

(IRE, about 0.45 V vs SHE). It was the first (most upstream) electrode in the microfluidic channel. Potentiostatic impedance spectra were collected at the Ru^{II}/Ru^{III} reversible potential as determined from the average of the anodic and cathodic peak potentials in CVs. This potential was slightly offset from 0.0 V vs IRE (see Fig. 7.3). The ac amplitude was 5 mV (rms), and the frequency range was from 100 kHz to ca. 0.1 Hz at 20 points per decade. The lower frequency limit was chosen by noting when the impedance was not significantly changed on decreasing the frequency. The flow rate was varied between 1 μL min^{-1} and 300 μL min^{-1} using a syringe pump (Harvard Apparatus PHD 2000).

7.2.3 Modelling

The geometry modeled is shown in Fig. 7.2, introducing the two dimensionless parameters, A ($= 6v_{\text{av}}h/D$), which is a Péclet number, and B ($= w/h$), which is a geometric parameter. Here, v_{av} is the average velocity in the channel, h is the channel height, D is a diffusivity, and w is the electrode width. To model diffusional impedance on a channel electrode, one has to solve the convective-diffusion equation for a 2-D channel, Eq. (7.2), which assumes laminar flow with a parabolic (Poiseuille) velocity profile.

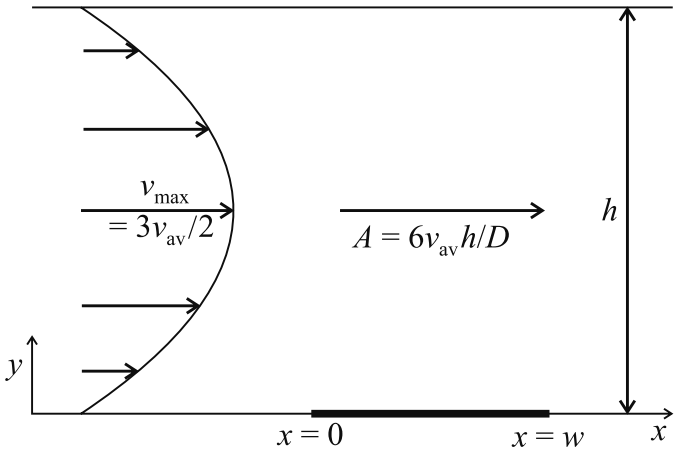

Figure 7.2: Geometry of the channel electrode in 2-D. Flow is from left to right, with one electrode (bold) in the bottom of the channel. The parabolic velocity profile is also shown, with the relationship between the average and maximum velocities.

$$\frac{\partial c_i(x,y,t)}{\partial t} = D_i\frac{\partial^2 c_i(x,y,t)}{\partial x^2} + D_i\frac{\partial^2 c_i(x,y,t)}{\partial y^2} - \frac{6v_{\text{av}}}{h^2}y(h-y)\frac{\partial c_i(x,y,t)}{\partial x} \quad (7.2)$$

Here, c_i is the concentration of reactant or product species $i = \text{R}, \text{P}$, and D_i is the diffusivity of species i. In the presence of the ac perturbation of angular frequency ω, the concentration will have the form of Eq. (7.3).

$$c_i(x,y,t) = c_{i,\text{ss}}(x,y) + \widetilde{c}_i(x,y)\exp(i\omega t) \quad (7.3)$$

Here, the ac concentration $\widetilde{c}_i(x,y)$ is complex. The linearity of Eq. (7.2) allows the steady-state and ac problems to be separated. To force reversibility, Butler-Volmer kinetics were used with an exchange current density of 10^{15} A m^{-2}. Reversibility was verified by comparing steady-state solutions with the Nernst equation solutions at the surface. At channel walls other than the electrode, the flux was set to zero. The inlet concentration was fixed at the bulk value, and the outlet boundary condition was that the concentration gradient was zero.

COMSOL Multiphysics® [59] was used for the numerical 2-D solution of the dc and ac equations. The 2-D solution may be scaled with the electrode depth d (normal to x and y) to compare with the experimental results. Edge effects in the z direction are small for an experimental ratio of $d/h = 10$ [175]. The channel length (x-direction) was set to 20 times the electrode width to ensure that the inlet and outlet conditions did not influence the solution. The electrode started at the midpoint of the channel. A strict meshing criteria was set based on the criteria of maximum diffusion length, $x_{\max} = \sqrt{D\pi^{-1}f_{\max}^{-1}}$, where $f_{\max}$ is the maximum frequency of the modeled impedance spectrum, here 10 kHz. The electrode mesh size at the surface was set to $x_{\max}/10$, while in the electrolyte volume, the mesh was allowed to grow to $10x_{\max}$ at a growth rate of maximum 5% per mesh point. The problem was solved using the PARDISO solver including a nested dissection multi-threaded pre-ordering algorithm.

For the chosen reaction kinetics at the electrode, Comsol's impedance mode automates the solution of the ac concentrations profiles $\widetilde{c}_{\mathrm{R}}(x,y)$ and $\widetilde{c}_{\mathrm{P}}(x,y)$. A harmonic perturbation of the potential with an amplitude set to 5 mV was used, for frequencies between 10^{-3} to 10^{4} Hz. The steady-state potential was set to the reversible potential so the steady-state current is zero. The dimensionless convective-diffusion impedance Z/Z_0 was calculated for each frequency by numerical integration of Eq. (7.4), c.f. Jacobsen and West [176].

$$\frac{Z}{Z_0} = \frac{1}{w}\int_0^w \left(\frac{-\widetilde{c}_{\mathrm{P}}(x,0)}{h\left(\partial\widetilde{c}_{\mathrm{P}}(x,y)/\partial y\right)_{y=0}} + \frac{-D_{\mathrm{P}}\widetilde{c}_{\mathrm{R}}(x,0)}{hD_{\mathrm{R}}\left(\partial\widetilde{c}_{\mathrm{R}}(x,y)/\partial y\right)_{y=0}} \right) \mathrm{d}x \tag{7.4}$$

This impedance may be derived using the procedure given by Orazem and Tribollet [177] (their Eq. (11.52) and following). For Butler-Volmer kinetics, Z_0 is given by Eq. (7.5).

$$Z_0 = \frac{2RTh}{n^2F^2D_{\mathrm{P}}d(c_{\mathrm{R}}^{\infty} + c_{\mathrm{P}}^{\infty})} \tag{7.5}$$

Here F is the Faraday constant, c_i^{∞} is the bulk concentration of species i, R is the gas constant, and T is the temperature.

7.3 Results and Discussion

7.3.1 Comparison between modeled and experimental data

Cyclic voltammograms for solutions with equimolar amounts of Ru^{II} and Ru^{III} show shapes expected for a reversible couple, Fig. 7.3. For first cycle scans, the peak potential was independent of scan rate and the peak currents were proportional to the square root of the scan rate. The difference between anodic and cathodic peak currents in the cyclic voltammogram is due to the difference in diffusion coefficients: $D_{\mathrm{Ru^{II}}} = 8.8 \times 10^{-10}$ $\mathrm{m^2\ s^{-1}}$, $D_{\mathrm{Ru^{III}}} = 5.71 \times 10^{-10}$ $\mathrm{m^2\ s^{-1}}$ [178]. The reversible potential was taken to be the average of the anodic and cathodic peak potentials, which was slightly shifted from 0.0 V vs IRE.

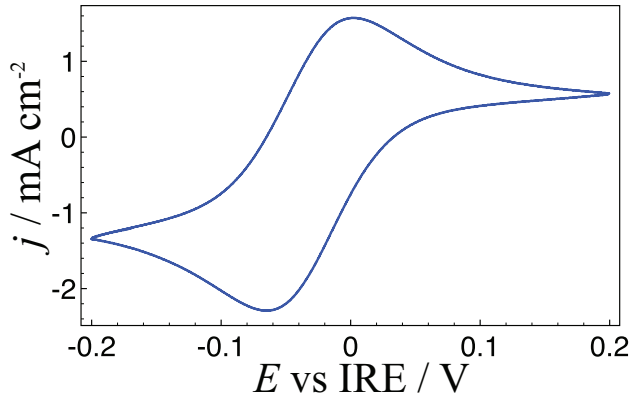

Figure 7.3: Steady-state cyclic voltammogram. Sweep rate 200 mV $\mathrm{s^{-1}}$. No flow.

Since the objective of this work was a careful study of the mass transport impedance, experimental and model impedances were evaluated at the reversible potential, where interference from the charge transfer resistance is minimized. Experimental impedance spectra are shown in Fig. 7.4 as a function of flow rate. At the highest measured frequency of $f_{\mathrm{max}} = 100$ kHz, the imaginary part of the impedance was small compared to the real part, which was independent of flow rate and represented the solution resistance. No distinguishable high frequency semicircle associated with the charge transfer resistance was observed, as expected for a fast reversible reaction. Therefore, correction for the solution resistance should give a pure convective diffusion impedance that can be compared with analytical or numerical simulations. This was done by estimating the solution resistance from the assumption that the real and imaginary part of the impedance should be equal at high frequencies, $Z_{\mathrm{Re}}(f_{\mathrm{max}}) = |Z_{\mathrm{Im}}(f_{\mathrm{max}})|$, meaning that the solution resistance could be estimated as $R_{\mathrm{s}} = Z_{\mathrm{Re}}(f_{\mathrm{max}}) - |Z_{\mathrm{Im}}(f_{\mathrm{max}})|$. This solution resistance was then subtracted from the real part of the impedance at all frequencies.

The resulting convective-diffusion impedance spectra have some features that are similar for all the flow rates. At high frequencies (low Z values), the Nyquist plot is

linear with a slope of one. This is a well-known feature of the Warburg impedance for semiinfinite planar diffusion to the electrode. At these frequencies, the ac diffusion length is small compared to the electrode width and channel height, and senses only the stagnant layer near the electrode surface. Therefore the impedance is not influenced by convection, electrode edge effects or channel height. At lower frequencies, the impedance deviates from the linear trend and the deviation occurs at lower Z-values for higher flow rates or lower diffusivities (higher A-values), as convection becomes more important. As the ac diffusion length becomes comparable to the electrode or channel dimensions, axial diffusion and the channel height can influence the impedance. At the lowest frequencies, the concentrations and current can keep up with the sinusoidal potential changes and the impedance becomes real.

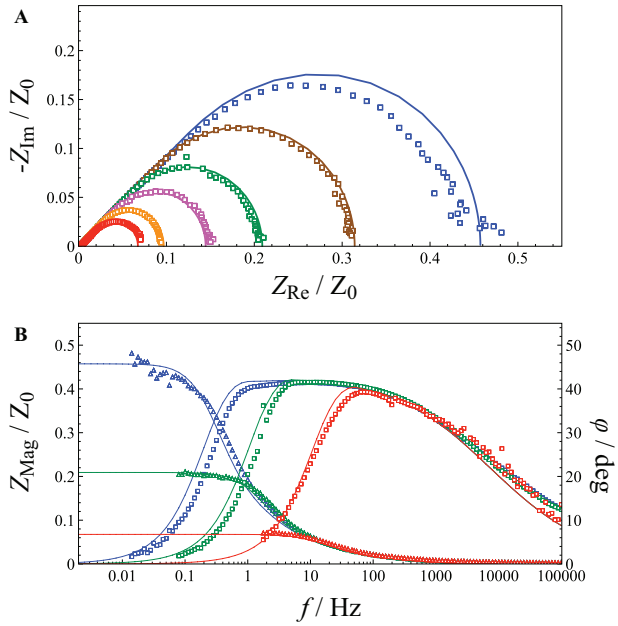

Figure 7.4: Potentiostatic impedance data at different flow rates. Experimental values are the squares and triangles. Comsol fits are the solid lines. Impedances have been corrected for solution resistance as described in the text. (a) Nyquist plot. Flows in μL min^{-1} are given in the order 1 (blue), 3 (brown), 10 (green), 30 (purple), 100 (orange), 300 (red), (b) Bode plot. Selected flow rates using the same color code.

The impedance spectra were modeled as described in the Section 7.2.3 using the literature diffusivities quoted above, the experimental temperature of 294 K and bulk concentrations of 4 mM. At the very highest frequencies, both the experimental and fitted results depart from 45° (Fig. 7.4b). In the case of the experimental results, this is due to non-faradaic processes, while for the numerical results, this is due to inadequately fine meshing for these conditions. At the lowest flow rate there is some experimental scatter at the lowest frequencies and the fit is worse. Aside from these small deviations,

the model shows excellent agreement with the experimental results over more than two orders of magnitude in flow rate and six orders of magnitude in frequency, indicating that the process is well described with the convective-diffusion equation, Eq. (7.2). This demonstrates the possibility of using a FE method to calculate impedance and use it as a tool to confirm the geometry or flow rate of a microfluidic flow cell.

7.3.2 Comparison between numerical and analytical solutions

Analytical approximations have the advantage of simplicity over numerical simulations, but they also more easily predict parameter dependences, such as dependence of limiting currents on flow rate. Therefore the Comsol simulations were compared with two common approximations in the literature, with parameter sets chosen to match two experimental data sets with distinct A and B values. The two literature approximations for channel electrode were described in the papers by Compton and co-workers [167–169, 171]. The first method [168] simplifies the convective diffusion equation, Eq. (7.2), so that axial diffusion is neglected (term 2) and so that the flow is simplified as Lévêque flow (term 4), i.e., the velocity is proportional to y. The second method [171] simplifies Eq. (7.2) so that the convection term is neglected (term 4). Both methods assume that the diffusivities are the same for both species.

The first set of parameters is to match the above experiments, at the lowest flow rate (1 μL min^{-1}). Fig. 7.5 compares the experimental data (black squares) with expressions for the two approximations (evaluated in Matlab® [179]), as presented by Compton and Winkler [171]. The geometric mean of the literature diffusivities was used as the common one required by the approximations, $D = 7.089 \times 10^{-10}$ m^2 s^{-1}; other parameters are as for the experiments, leading to $A = 141.4$, $B = 1.0$. The no-convection solution (blue triangles) is far from experiment, except in the high-frequency range where the Warburg impedance for semiinfinite 1-D diffusion to a planar electrode suffices. The no-convection solution at low frequencies will only be a reasonable solution at flow rates much lower than those achieved under controlled conditions with a syringe pump. The Lévêque and no-axial diffusion approximation (green triangles) comes within the experimental error and is close to the numerical solutions. This approximation is expected to be better at higher flow rates, and so the case shown here is the most stringent test among our experimental data; higher flow rates did show better agreement between this approximation and the numerical solution. This confirms the conclusion from Compton and Winkler's work [171], that the Lévêque and no-axial diffusion approximate solution is useful for a wide range of flow conditions.

A second comparative data set is that given by Compton and Winkler [171] in their Fig. 4f, shown here as black squares in Fig. 7.6. Under the conditions modeled here ($A = 1234$, $B = 0.01625$), the no-convection solution (blue triangles) is not very accurate, but it is a better approximation than previously. The narrow electrodes make the Lévêque and no-axial diffusion solution (green triangles) worse than before, and so neither solution is a good approximation. Our calculated values for these approximations agree with those given by Compton and Winkler. The Comsol numerical solution of the the full

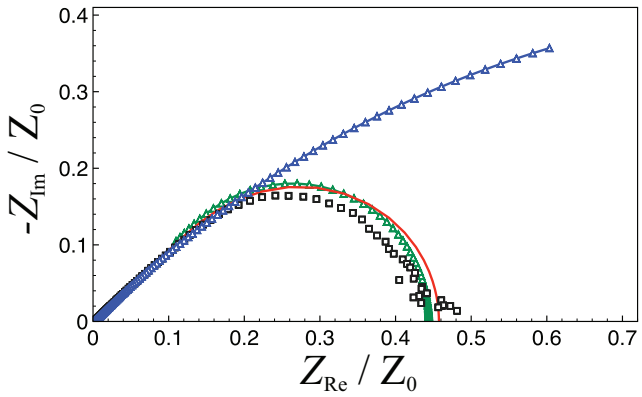

Figure 7.5: Potentiostatic electrochemical impedance spectroscopy modeled at a flow rate of 1 μL min^{-1}. The experimental values are shown as red squares, the Comsol model is the full line (red), the method described by Compton et al [168] assuming no axial diffusion and the Lévêque approximation for the flow is shown as the green triangles, and the solution assuming no convection is shown as blue triangles.

convective-diffusive equation (red line) gives a result that fits well with the experimental values. Hence, for some flow conditions and geometries, it is necessary to use the full numerical solution to get a satisfactorily fit to the experimental data.

At low flow, high diffusivities, or low w/h ratios (B-values) it is expected that axial diffusion can no longer be neglected. Furthermore, the Lévêque approximation is expected to be inaccurate for wide electrodes (high B-values) or low flow rates (low A-values) as it is assumed that the top of the channel does not influence the resulting impedance. In addition, it has a high-frequency limit of applicability as derived by Compton and Sealy [168], which is normally about 50 Hz for our dimensions. This high-frequency limit is not a serious drawback, as the semiinfinite diffusion solution is a good approximation at higher frequencies.

The numerical solution clearly has advantages in the flexibility it offers for problems with all ranges of geometries and flow. Its key assumption is simply that the flow is laminar with a parabolic profile, an assumption that is well validated in microfluidic systems some distance away from the channel inlet. The flow should not be so slow that the inlet or outlet conditions influence the result at the electrode surface, and for the numerical solution this means that at low frequencies the inlet and outlet lengths should be much longer than the ac diffusion length.

7.3.3 Validity of the no-axial diffusion and Lévêque approximations

Here, the solution with the Lévêque approximation and no axial diffusion is compared to the Comsol result. Assuming that Comsol gives an accurate result for all flows and geometries, the validity region for the no axial diffusion and Lévêque approximation can

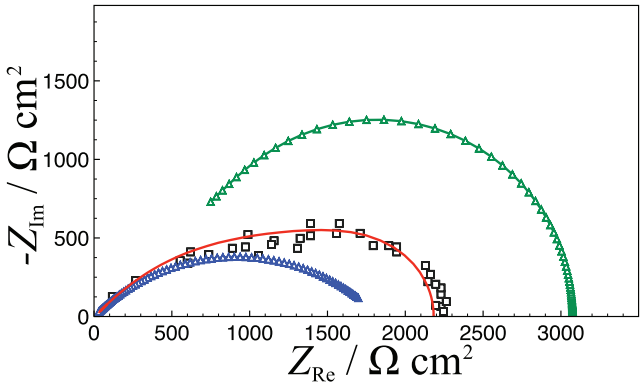

Figure 7.6: Model comparisons of experiment and theory. Adapted with permission from Figure 4f in Ref. [171], Copyright (1995) American Chemical Society. Experiment (black squares), Lévêque and no axial diffusion approximation (blue triangles), no-convection approximation (green triangles), Comsol numerical solution (red line).

be determined. A matrix of values for A ($= 6v_{\text{av}}h/D$), and B ($= w/h$) was simulated, and agreement between the accurate and approximate solutions was quantified based on the error at the lowest frequency. The results are color coded in Fig. 7.7, together with experimental values from this work (with good fit at $B = 1$, blue crosses), and from Compton and Winkler [171] ($B = 0.1$ and lower, brown crosses). Based on these results, linear zone boundaries were assigned, showing the limits of validity for the two approximations: the Lévêque approximation (dotted line, $B^{-1}A^{1/2} = 1$) and the neglect of axial diffusion (solid line, $BA^{1/2} = 3$). That is, axial diffusion may be neglected for $BA^{1/2} \geq 3$ (faster flow and wider electrodes/lower channels) and the Lévêque approximation holds for $B^{-1}A^{1/2} \geq 1$ (faster flow and narrower electrodes/higher channels). These conditions are given in terms of the original variables in Eqs. (7.6) and (7.7), and the analytical solution for no-axial diffusion and the Lévêque approximation holds when both conditions hold. If one has a geometry or flow not satisfying these conditions, a full numerical solution is necessary.

$$BA^{1/2} = \left(\frac{6w^2 v_{\text{av}}}{hD}\right)^{1/2} \geq 3 \tag{7.6}$$

$$B^{-1}A^{1/2} = \left(\frac{6h^3 v_{\text{av}}}{w^2 D}\right)^{1/2} \geq 1 \tag{7.7}$$

7.4 Conclusions

The FE method software (COMSOL Multiphysics®) reproduces the experimental impedance spectra for a reversible redox couple, over more than two orders of magnitude in flow

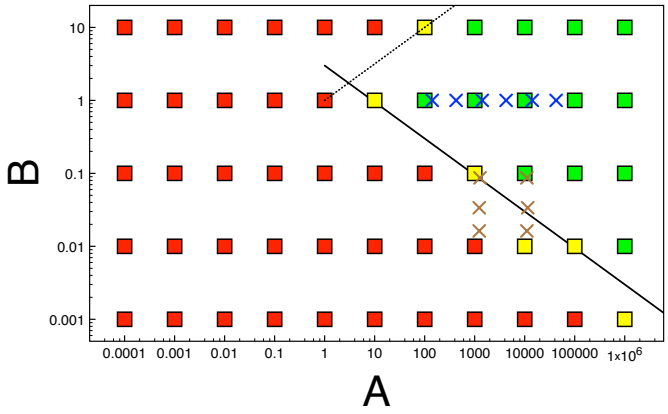

Figure 7.7: Validity analysis of the no axial diffusion and Lévêque approximation. Error at the lowest frequency is color coded: $< 10\%$ (green), $10 - 25\%$ (yellow), $> 25\%$ (red). Blue crosses are the experimental values from this work (at $B = 1$), and brown crosses are the values from Compton and Winkler's work [171] (at $B = 0.1$ and lower). The lines are the zone boundaries described in the text.

rates. It can be used to investigate the validity of analytical methods described in the literature, namely one neglecting axial diffusion and using the Lévêque approximation for the flow, and one where the convection was neglected. Although useful for many flow regimes, the assumptions used in the derivations of these solutions are not valid for all flows and electrode sizes and the non-universal validity of these methods is demonstrated. Estimates are given for when axial diffusion can be neglected and when the Lévêque approximation holds.

The FE method can be applied for a wide set of conditions, such as flow regimes, varying diffusivities for different species, varying electrode sizes and varying kinetics. In particular, the low-frequency intercept is well determined. It has the principal drawback of numerical methods that the spectra are solved for a single set of parameters at a time, but it is promising as a guide to find more accurate analytical approximations.

7.5 Acknowledgments

Financial support from the Natural Sciences and Engineering Research Council of Canada (discovery grant 37035), the Research Council of Norway (project 221899), the University of Victoria, and the Norwegian University of Science and Technology is gratefully acknowledged. The Research Council of Norway is also acknowledged for the support to the Norwegian Micro and NanoFabrication Facility, NorFab (197411/V30). Thomas Holm thanks the Faculty of Natural Sciences and Technology at Norwegian University of Science and Technology for the award of a scholarship.

Appendix A: Supplementary material

A detailed description of the Comsol setup and procedure is given in Appendix C.

8 Mass transport impedance at channel electrodes: Using a double electrode setup

THOMAS HOLM[a,b], MATS INGDAL[a,b], JONATHAN STROBL[b], ESPEN V. FANAVOLL[a,b], SVEIN SUNDE[a], FRODE SELAND[a], DAVID A. HARRINGTON[b]

[a] *Department of Materials Science and Engineering, Norwegian University of Science and Technology, NO-7491 Trondheim, Norway.*
[b] *Department of Chemistry, University of Victoria, Victoria, British Columbia, V8W 3V6, Canada.*

This chapter intended for publication at a later stage.

Abstract

A method for measuring downstream concentration effects using a double channel electrode is demonstrated. The method consists of using a single potentiostat to set a current perturbation at an upstream electrode and measuring the resulting potential response at a downstream electrode. A numerical simulation is used to explain the phenomena and a qualitative explanation of the features is given which lays the foundation for a more rigorous theoretical treatment. Such a method allows for simultaneous acquisition of geometric, diffusional, and convection parameters, and is potentially a quick method of characterization for channel electrodes.

8.1 Introduction

The ease of fabrication offered by soft lithography using PDMS has led to a large increase in the use of microfluidic flow cells in the last decade. For electrochemists, the laminar flow regime offers the possibilities of making membraneless fuel cells [53], membraneless water electrolysers with automatic gas separation [180], and various sensor technologies [181]. A series of electrodes in a microfluidic channel can serve as an electroanalytical tool analogous to the rotating ring-disc electrode (RRDE), with an upstream generator electrode and downstream detector electrodes. In this role, channel electrodes allow for more flexible configurations, high collection efficiencies, and use of much smaller amounts of analyte.

Solutions for various kinetics and mass transport problems at a single channel electrode are available for a single channel microband, including transient current response [182–185] and impedance [60, 168, 169, 171]. For downstream electrodes, dc collection

efficiency calculations are available for a single species [54, 147], and for more complicated reaction mechanisms [186, 187]. A complication for channel electrodes is that, unlike the RRDE, they are not uniformly accessible, and without approximations only numerical solutions are possible. In the case of impedance, Albery has given a solution for the ac collection efficiency at the RRDE based on Laplace transform methods [188, 189], but numerical approximations were required, and a qualitative analysis as we present below was not attempted.

In order to use ac downstream detection methods, it is important to calibrate the method. Here, we use a fast reversible redox couple and compare experimental, numerical, and approximate analytical solutions for a new quantity, the downstream impedance, Z_{dn}. This is defined as the ratio of the ac potential at a downstream sensing electrode (SE) to the ac current density at the upstream working electrode (WE), Eq. (8.1), where the ac quantities are frequency-dependent complex number phasors in the usual way. In the approximation that the redox couple is reversible, the Nernst equation relates the instantaneous potential to the instantaneous concentrations at both the WE and SE. The ac concentration profile generated at the WE flows downstream and causes an ac potential at the SE. An approximate treatment gives a very simple interpretation of Z_{dn} in which the phase acts as "clock" for a concentration wave traveling down from the WE to the SE, and the magnitude is a measure of the diffusive spread across the channel during this travel. A feature of the present method is that it implements a generator-collector measurement without a bipotentiostat.

$$Z_{\mathrm{dn}} = \frac{\widetilde{E}_{\mathrm{SE}}}{\widetilde{j}_{\mathrm{WE}}} \tag{8.1}$$

8.2 Experimental

8.2.1 Microfluidics

The production of the microfluidic cells has been described previously [60] and is given in detail in Chapter 2. The geometry of the cell is shown in Fig. 8.1a, with electrode widths, w = 100 μm, channel height, h = 100 μm, and channel depth (distance between channel walls perpendicular to flow direction), d = 1 mm, and distance between the midpoint of the upstream and downstream electrodes, l = 200 μm.

8.2.2 Electrochemistry

The experimental preparation was the same as in our earlier work [60], and used a Gamry Ref. 600 potentiostat. The first electrode upstream (of a total of four) is the reference electrode (RE), the second electrode is used as the working electrode (WE), the third electrode is the sensing electrode (SE) and the fourth electrode is the counter electrode (CE), as described in Fig. 8.1a. The measurements were then run by setting a galvanostatic electrochemical impedance spectroscopy (GEIS) experiment with a 100 nA amplitude

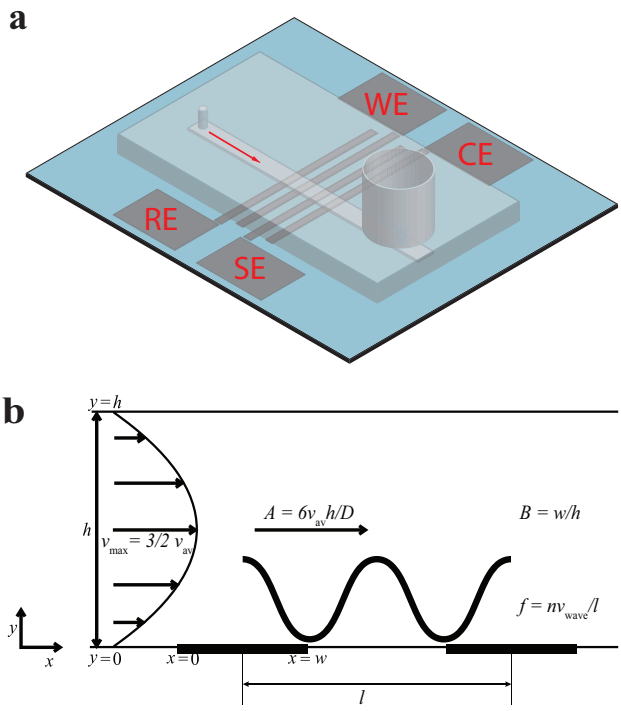

Figure 8.1: Figure showing a model of the cell (a), and the geometry modeled in this work (b). In (a), the arrow indicates the flow direction in the channel and the electrodes are marked as reference electrode (RE), working electrode (WE), sensing electrode (SE), and counter electrode (CE). In (b), flow is from left to right, with two electrodes (bold) in the bottom of the channel. The parabolic velocity profile is also shown, with the relationship between the average and maximum velocities. A sine wave is shown above the electrodes to illustrate the concentration downstream as a wave propagation. The formula, $f = nv_{\text{wave}}/l$, illustrates the origin of the frequency of the in-phase concentration response (phase angle = 0) in the simple theory discussed in the text.

(rms) at the working electrode where the working connection wire was connected in the Gamry setup. At the downstream sensing electrode, the working sense wire is connected to measure the potential vs RE, which gives a response that depends on the galvanostatic stimulus at the working electrode. The impedance measurements were done under varying flow conditions from 30 μL min^{-1} to 300 μL min^{-1}. The resulting experimental data was corrected to follow the criterion that $Z(\omega \to \infty) = 0$ if that was not met already.

8.2.3 Numerical modeling

The channel geometry is described by the 2D convective-diffusion equation (Eq. (8.2)), and shown in Fig. 8.1b, with the flow rate being the fully developed flow $v(y) = 6v_{\mathrm{av}}y(h-y)/h^2$.

$$\frac{\partial c_i}{\partial t} = D_i\frac{\partial^2 c_i}{\partial x^2} + D_i\frac{\partial^2 c_i}{\partial y^2} - v(y)\frac{\partial c_i}{\partial x} \tag{8.2}$$

Here, v_{av} is the average velocity in the channel, h is the full channel height, D_i is the diffusivity of species i, c_i the concentration of species i, t the time, and x and y are the directions parallel to the channel flow and perpendicular to the channel flow direction, respectively. Eq. (8.2) has to be solved in the electrolyte volume for an applied current perturbation at the working electrode. This makes it possible to find the average concentrations on the sensing electrode, which can then be used to calculate the potential perturbation.

A finite element method solver (COMSOL Multiphysics®[56]) was used to find the solution of the problem described above without further simplifications. Comsol only solves ac potential perturbations and not current perturbations. To circumvent this, linear current-potential kinetics were set at the WE with a fake ac potential that corresponded to the applied ac current. The software uses the ac current to determine the ac fluxes, and solves for the ac concentration profile. The ac potential at the downstream electrode was then calculated from the linearized Nernst equation (Eq. (8.3)), which was averaged over the electrode surface, and was finally used to calculate the impedance according to Eq. (8.1).

$$\widetilde{E}_{\mathrm{SE}} = \frac{RT}{F}\frac{\widetilde{c}_{\mathrm{Ru^{III}}}}{c_{\mathrm{Ru^{III},ss}}} - \frac{RT}{F}\frac{\widetilde{c}_{\mathrm{Ru^{II}}}}{c_{\mathrm{Ru^{II},ss}}} \tag{8.3}$$

8.3 Results and discussion

The experimental downstream impedance, Z_{dn}, for the flow rates of 30 μL min^{-1} to 300 μL min^{-1} are shown in Fig. 8.2. The flow rate clearly influence the resulting downstream impedance, Z_{dn}, but the features are generally the same. For the Nyquist representation, Fig. 8.2a, the impedance changes from a real positive impedance at low frequencies and changes in a spiraling fashion to 0 at high frequencies. From the development of the

phase angle, Fig. 8.2b, this spiraling goes on for approximately 1.5 full rounds, and the whole change in magnitude, Fig. 8.2c, is occurring in about one decade of frequencies. This is exemplified by the highest flow rate, 300 μL min^{-1}, where the whole change in magnitude is occurring between 5 Hz and 100 Hz in Fig. 8.2c. For an increase in flow rate, a decrease of the magnitude of the impedance is observed at low frequencies, as has been observed for electrochemical impedance spectroscopy at one electrode [60, 171].

Comsol can be used to model the response downstream impedance, Z_{dn}, and the resulting numerical simulation with the experimental data for 100 μL min^{-1} is shown in Fig. 8.3. From the Nyquist representation, Fig. 8.3a, and the magnitude plot, Fig. 8.3c, it is clear that at low frequencies, the Comsol model overestimates the magnitude. However, the features are all described by the model, and, as expected, the convective-diffusion equation, Eq. (8.2), describes the system well. The difference between the model and the experimental data at low frequencies may be due to uncertainties in the experimental input data, for example, there is an uncertainty about what the real concentration are in the solution [60]. At low frequencies, an offset is expected as the model does not include double-layer charging. This effect will matter more as the frequency is increased as is visible both for the phase angle, Fig. 8.3b, and the magnitude, Fig. 8.3c.

8.3.1 Establishing the parameter dependencies

From the analytical and modeled result of impedance at one electrode, the result is found to be dependent on a Péclet number, $6v_{\mathrm{av}}h/D$, and a geometry factor, w/h [60]. For downstream impedance, Z_{dn}, an additional dependency is expected to be the distance between the electrodes and the relative electrode sizes. This work focuses on constant electrode sizes and constant distance, and only the dependency on flow rate is explored. Normalization of the impedance spectra can be helpful in defining these dependencies and from the derivation of the collection efficiency [54] and from the solution of the impedance at one electrode [171, 190], a scaling of the impedance by the cube root of the flow rate is expected. This is done in Fig. 8.4a, where the real and imaginary impedance is scaled by using parameter $\zeta = ZV^{1/3}$, where V is the volumetric flow rate. Fig. 8.4a indicates that firstly, the numerically calculated data is consistent meaning that they overlap well, while for the experimental data, overlap is except at the lowest flow rate (30 μL min^{-1}) for the lowest frequencies. This illustrates the challenge of running these experiments and getting consistent data for a series of flow rates, as the result is very sensitive to concentration changes and to the experiment being run around a stable open-circuit potential. However, the internal consistency in the Comsol modeled data indicates that as the Lévêque approximation and no axial diffusion is used in the derivation of the $V^{-1/3}$ dependency, this is also a valid assumption for these flow rates and the type of experiment used here, as was confirmed for these flow rates for regular impedance experiments [60].

In a similar fashion, one can look at the magnitude. In Fig. 8.4b, the magnitude is scaled through the ζ parameter while the frequency is scaled as $F = f^{1/2}V_{\mathrm{av}}^{-1/3}$. While the scaling of the magnitude confirms the findings indicated by Fig. 8.4a, the scaling of

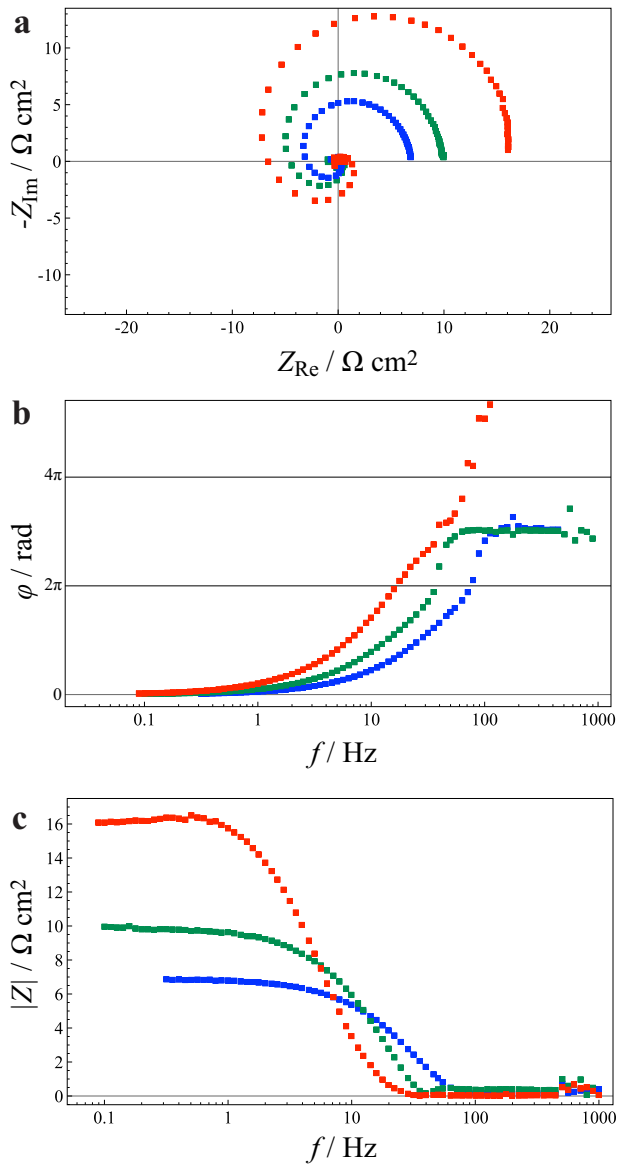

Figure 8.2: Experimental data collected in a microfluidic flow cell. Flow rates of 30 μL min^{-1}(red), 100 μL min^{-1}(brown), and 300 μL min^{-1}(blue). Insert shows the angle in the impedance spectra vs frequency for the 10 μL min^{-1} (blue) and 300μL min^{-1}(red) results.

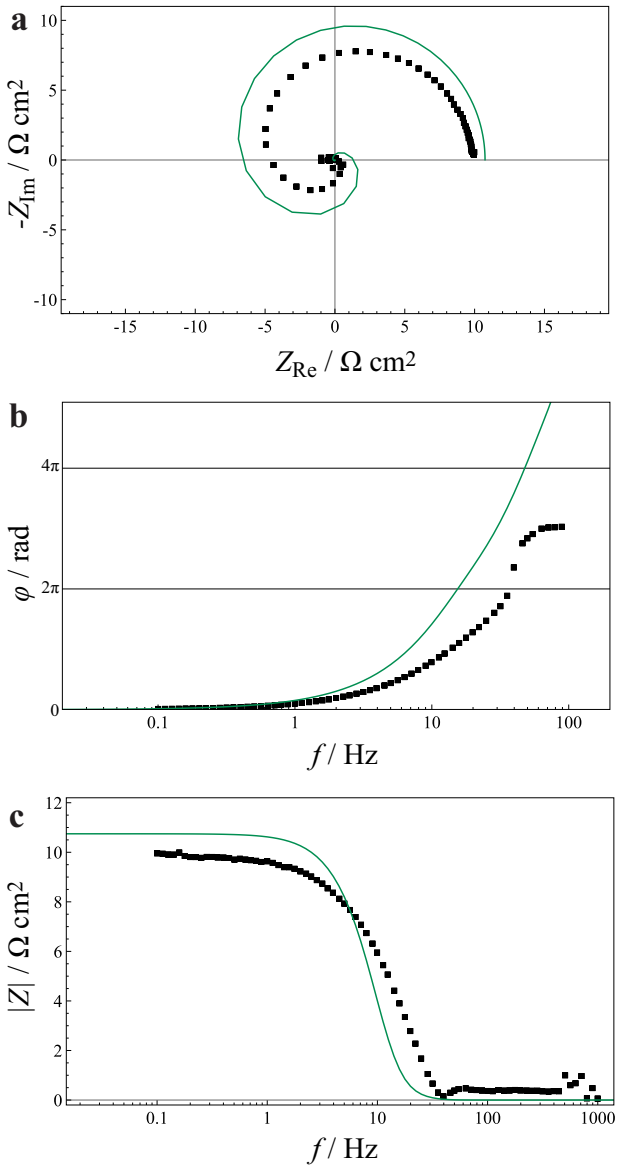

Figure 8.3: Experimental and numerically calculated data for the 100 μL min^{-1} flow rate. The experimental values are shown as black boxes, while the numerical results calculated using Comsol are shown as green lines. The figure shows the Nyquist plot (a), angle vs the logarithm of the frequency (b), and magnitude vs the logarithm of the frequency (c).

the frequency indicates that the diffusion length of an ac perturbation for high frequencies is expected to spread proportionally to $\sqrt{D/f}$ giving a dependency on $f^{1/2}$. On the other hand, the normalization of the frequency by the cube root of the flow rate $V^{1/3}$ indicates that as the frequency is increased, the diffusion layer thickness is determined by the flow rate as given for steady-state systems. Therefore, a dependency on the cube root of the flow rate is seen both for the magnitude and the frequencies. This gives a similar trend as for the Nyquist normalization in Fig. 8.4a, meaning that the experimental results overlap except for the lowest flow rate (30 μL min^{-1}) at low frequencies, and the numerical simulation overlap well at all flow rates.

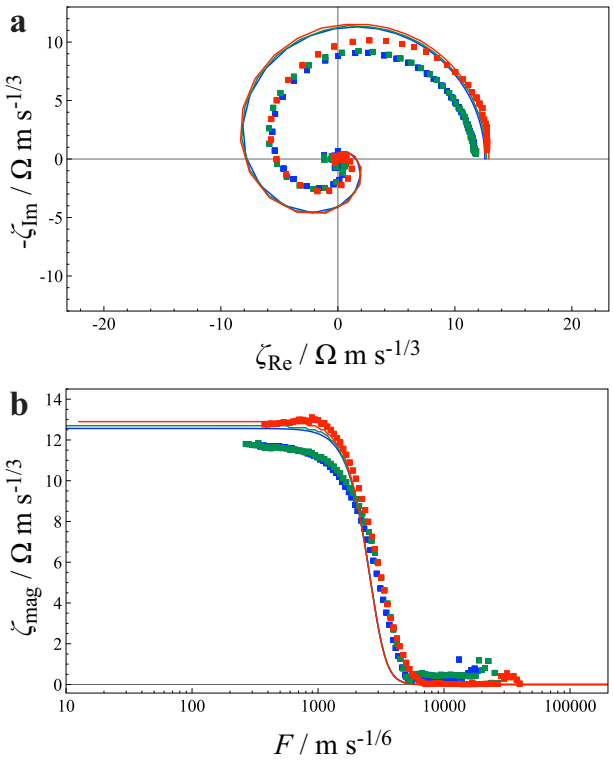

Figure 8.4: Experimental and numerically calculated data for all flow rates shown as normalized impedance, $\zeta = ZV_{\text{av}}^{1/3}$. The data is shown as a Nyquist representation (a), and as a normalized magnitude vs normalized frequency, $F = f^{1/2}V_{\text{av}}^{-1/3}$ (b). The experimental values are shown as boxes, while the numerical result calculated using Comsol is shown as full lines. The flow rates are 30 μL min^{-1} (red), 100 μL min^{-1} (green), and 300 μL min^{-1} (blue).

All the data from numerical simulation is the result of averaging over the downstream electrode. This works well when the concentrations at the electrode are fairly constant. However, when the frequency of the current perturbation increases, the flow rate can lead to several wavelengths being present at the electrode simultaneously. This would lead to

potential distributions on the electrode surface, but a real metal electrode can not have a distributed potential without currents actually running between the different points on the electrode, effectively averaging any potential distribution. Such an effect leads to a noise at high frequencies. This is seen in Fig. 8.2b where the angle plot levels out at $3\pi/2$, while the numerical model continues to higher angles. However, while electrode averaging certainly can be a problem at very high frequencies, the normalization method in Fig. 8.4 seems to indicate that although the flow rates varies by one order of magnitude, there is very little difference between the normalized impedances indicating that electrode averaging is a secondary effect.

8.3.2 An approximate treatment

The rest of the paper offers qualitative explanations of the above results. The simplifying assumption is made that the diffusivities are equal, so only one convective diffusion problem needs to be considered. In this case, the principle of total unchanging concentration [145, 191] applies so that $\widetilde{c}_{\mathrm{Ru^{III}}} = -\widetilde{c}_{\mathrm{Ru^{II}}}$, which will simply be referred to as $\widetilde{c}$. This simplifies the linearized Nernst equation, Eq. (8.3), and reduces it to Eq. (8.4). This implies that the potential at the SE is a scaled version of the ac concentration at its surface and is in phase with it.

$$\widetilde{E}_{\mathrm{SE}} = \frac{2RT}{Fc_{\mathrm{ss}}}\widetilde{c}_{\mathrm{SE}} \tag{8.4}$$

The same relationship between ac potential and concentration applies at the WE, but there, the ac current is proportional to the ac flux. Since the conventional impedance defines a relation between ac concentration and ac flux, the relationship between the downstream impedance, Z_{dn}, and the impedance at the working electrode can be defined as given in Eq. (8.5). Here, Z_{dn} is proportional to $\widetilde{c}_{\mathrm{SE}}/\widetilde{j}_{\mathrm{WE}}$, and conventional impedance, Z, is proportional to $\widetilde{c}_{\mathrm{WE}}/\widetilde{j}_{\mathrm{WE}}$. Observing in previous work on the electrochemical impedance at a channel electrode [60, 171], the resulting phase angles are bounded by 0 and $\pi/4$ meaning that the majority of the resulting phase angles in the downstream impedance, Z_{dn}, is from the ratio of the ac concentrations at the working and the sensing electrode, $\widetilde{c}_{\mathrm{SE}}/\widetilde{c}_{\mathrm{WE}}$.

$$\frac{\widetilde{c}_{\mathrm{SE}}}{\widetilde{c}_{\mathrm{WE}}} \times \frac{\widetilde{c}_{\mathrm{WE}}}{\widetilde{j}_{\mathrm{WE}}} = \frac{\widetilde{c}_{\mathrm{SE}}}{\widetilde{j}_{\mathrm{WE}}} \tag{8.5}$$

Assuming that the phase angles can be found from the concentrations, a simplified treatment can be done. First, the electrodes are viewed as a sensor of the concentration at their midpoints. Such a case is illustrated by Fig. 8.5. An ac concentration change occurs at the WE and is then traveling downstream with a fixed frequency and some averaged velocity, v_{wave}. This is then sensed at the downstream electrode and depending on if the midpoint at the SE is in phase or out of phase with the WE electrode, one gets the phase relationship at that frequency. Three cases are given in Fig. 8.5, where two of them, (a) and (c), are examples of cases where the resulting impedance is in-phase and represents

two full or 4 full wavelengths between the electrodes. The last case (b) is a case where 2.5 full wavelengths are between the electrode midpoints resulting in a completely out-of-phase response. Based on such an explanation, a simple criteria for in-phase response can be derived and is given in Eq. (8.6).

$$f = \frac{n v_{\text{wave}}}{l} \tag{8.6}$$

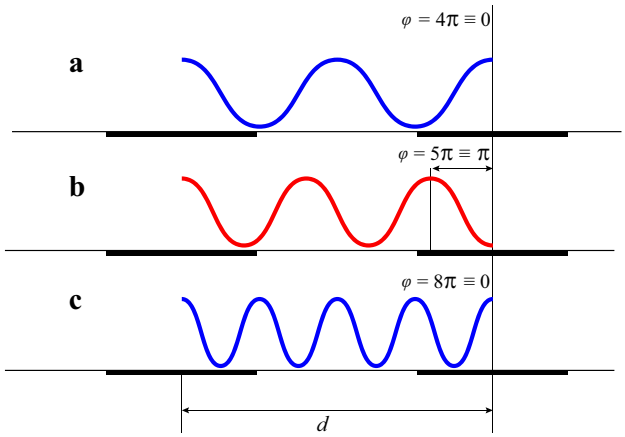

Figure 8.5: Figure demonstrating the principle of in-phase and out of phase concentrations. The examples given are for in-phase concentration with $n = 2$ (a), out-of-phase concentration with $n = 2.5$ (b), and in-phase concentration with $n = 4$ (c). Example a and c results in a positive real impedance, while example b results in a negative real impedance.

In this case, n is the number of full rotations. This result can be derived mathematically if one ignores the diffusion terms in the convective-diffusion equation, Eq. (8.2), and approximates the velocity as independent of y, i.e., $v(y) = v_{\text{wave}}$. The simplified equation is then linearized, Eq. (8.7), and solved to find that the phase delay changes linearly with x, Eq. (8.8).

$$\mathrm{i}\,\omega \widetilde{c}(x) = v_{\text{wave}} \frac{\mathrm{d}\,\widetilde{c}(x)}{\mathrm{d}\,x} \tag{8.7}$$

$$\widetilde{c}(x) = \widetilde{c}(0) \exp\left(\frac{i\omega x}{v_{\text{wave}}}\right) \tag{8.8}$$

For an electrode separation of $x = l$, the phase of $\widetilde{c}_{\text{SE}}/\widetilde{c}_{\text{WE}}$ is therefore $\varphi = \omega d/v_{\text{wave}}$, which reaches $2\pi n$ at frequencies given by Eq. (8.6). A prediction of this model is that the phase is linear with the frequency, which is approximately true, Fig. 8.6. From the slope the slope in Fig. 8.6, one has to make an estimate of v_{wave}. Here, a useful first approximation is that the distance from the electrodes that is actually influenced by diffusion is proportional to $v_{\text{av}}^{1/3}$ as confirmed by the overlap in Fig. 8.4.

Therefore, v_{wave} can be estimated as some velocity inside this diffusion layer. At the endpoint of the WE, the dc diffusion layer thickness for a flow of 100 μL min^{-1}, is given as $\delta = 3^{-1/3}\Gamma(1/3)(Dh^2bx/6V_0)^{1/3} \approx 19$ μm [63], and the experimental concentration velocity, v_{wave}, must be a flow rate well inside this layer. The experimental result giving a phase angle of 2π is about 40 Hz for the 100 μL min^{-1} data. Using the v_{wave} estimated from Eq. (8.6), the position of the calculated v_{wave} is 8.7 μm from the electrode based on the parabolic flow ($v(y) = 6v_{\text{av}}y(h-y)/h^2$). Therefore, this approximate treatment is suitable to explain the qualitative features, but it does not give any method to actually estimate v_{wave} as a function of the flow rate. Comparing the experimental slope of 0.025 rad Hz^{-1} and using the v_{wave} found for the first full round at 40 Hz, one finds a slope of 0.157, i.e., slightly below the one estimated from the slope in Fig. 8.6. This indicates that Eq. (8.6) is a good qualitatively way to understand the phenomena, but full description of the non-linear experimental phase behavior will require a better model.

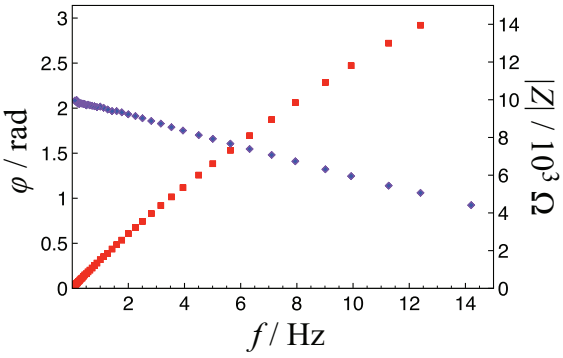

Figure 8.6: Figure showing the angle (blue diamonds) and magnitude (red rectangles) vs the frequency for the frequencies in the first half round of the spiral for the 100 μL min^{-1} experimental data.

Considering now the magnitude, there are two effects that are operating. Firstly, the electrodes have finite extent, so that at higher frequencies, they average the waves, as would be significant for the waves depicted in Fig. 8.5 and especially for the last case. From experimental data in Fig. 8.2, one can say that for phases above 4π, the signal degrades to zero. The wavelength is less than the electrode width for wavelengths of $v_{\text{wave}}/f \lesssim d/2 = w$ or above about 80 Hz for when the flow rate is 100 μL min^{-1}. The second effect that decreases the magnitude with frequency, is that as the concentration wave moves downstream, diffusion across the channel reduces the magnitude. This effect would be enhanced further for small wavelengths as the distance between the concentration "peaks" are small and this reduces the necessary diffusion length. In addition, a smaller fraction of the current contributes to double layer charging at high frequencies, which is an effect that does not produce a large concentration change, and this further reduces the concentration response at the downstream electrode.

It is interesting to compare the phase and magnitude changes in Fig. 8.6 with the

theory developed by Albery and co-workers [192] for the ac collection efficiency at the analogous RRDE, defined as in Eq. (8.9).

$$N_\omega = -\frac{\widetilde{i}_\mathrm{R}}{\widetilde{i}_\mathrm{D}} \tag{8.9}$$

Here $\widetilde{i}_\mathrm{R}$ is the current amplitude of the response at the ring electrode, and $\widetilde{i}_\mathrm{D}$ is the current amplitude at the disc electrode. The setup behind the development of the theory here, involves an ac perturbation at the disc electrode and detection of the ac current at a constant potential at the ring electrode. Obviously, our experimental method is different from this method, but the general features are similar. Fig. 8.6 is similar to the plot shown in Fig. 1 in Albery and co-workers paper [192]: there is decrease in magnitude and an increase in phase angle as the frequency is increased. However, their magnitude decreases approximately exponentially, in contrast to our linear decrease. Our phase rise is also more linear than for N_ω.

From the discussion including Fig. 8.6, it is clear that a separate analytical channel electrode theory would be helpful. The relationship between the channel and RRDE solutions would ideally resemble that of the steady-state collection efficiencies described by Brett and Oliveira Brett [54]. Here, the dependencies on geometry factors are cubed in rotating ring-disc geometry, while it is linear in channel electrodes, and this is useful to explain the difference in Fig. 8.6.

8.4 Conclusion

A new measurement technique, downstream electrochemical impedance spectroscopy, Z_dn, is described. This technique modulates the current at an upstream electrode and senses the resulting modulation in the concentration at a downstream high-impedance sensor electrode. It offers new possibilities of in terms of detection of soluble intermediates in microfluidic electrochemical devices.

This technique is described and experimentally tested for the case of a reversible redox couple in solution. The Nyquist plots show beautiful spirals. Numerical simulations were used to verify the results, and a simple qualitative analysis is given for the phase dependence. Analytical approaches show that this is the correct first-order explanation of the phase. An exact solution for the ac concentration dependence between electrodes is given, under the assumption that axial diffusion may be neglected. Despite being an upstream-generation/downstream-detection method, it was implemented using only one potentiostat. The method is most useful for relatively small electrodes compared to the distance between them, and for higher flow rates ($A > 100$).

8.5 Acknowledgments

Financial support from the Natural Sciences and Engineering Research Council of Canada (discovery grant 37035), the Research Council of Norway (project 221899), the Univer-

sity of Victoria, and the Norwegian University of Science and Technology is gratefully acknowledged. The Research Council of Norway is also acknowledged for the support to the Norwegian Micro and NanoFabrication Facility, NorFab (197411/V30). Thomas Holm thanks the Faculty of Natural Sciences and Technology at Norwegian University of Science and Technology for the award of a scholarship. We thank Rhonda Stoddard for synthesis of some ruthenium (II) hexaammine chloride.

Appendix A: Supplementary material

A detailed description of the Comsol setup and procedure is given in Appendix D.

9 Conclusions and further work

This thesis aims at providing new methodology and measurements of Pt electrochemistry in acidic electrolytes. The experimental activity is based on the observation that due to sluggish kinetics, most relevant liquid fuels were not economically viable. Therefore, a more thorough knowledge of the reaction mechanism is paramount to making progress in this field. Two approaches were identified that shows promise: (1) to develop a method using a self-pressurized autoclave to run high temperature aqueous electrochemical experiments, (2) to develop microfluidic flow cells that can be characterized and ultimately be used as an electroanalytical tool. The conclusions and suggestions for further work are summarized below.

9.1 Conclusions

The new aspects not previously observed due to the work in part I:

- A method using a self-pressurized autoclave was developed and issues with reproducibility and solution resistance related to high temperature aqueous electrochemistry were discussed and solved.
- The mechanism and rate-determining step for methanol oxidation does not seem to change as a function of temperature up to 140°C, and it was either the dissociative adsorption of water or the dissociative adsorption of methanol at all temperatures.
- The rate-determining mechanism for glycerol oxidation in acidic solution seem to change with an increase in temperature. Oxidation to glyceraldehyde was suggested as the main product at temperatures above 110°C and at low overpotentials.
- An increase in temperature improves the kinetics for platinum oxidation in acidic solution. Charge-transfer coefficient of 1 suggests that platinum oxidation either does not involve an OH intermediate or that this reaction step is very fast compared to the subsequent oxidation in the early stages of platinum oxide growth.
- Fitted dEIS parameters for platinum oxidation in acidic solution suggests that at all potentials, the influence of surface oxide charge density is much larger than the influence of the temperature.

And for part II:

- Soft lithography methods were used to produce microfluidic flow cells including several channel electrodes.
- An eigenfunction method was used to calculate the limiting current and collection efficiency at channel electrodes and demonstrated that this method can solve the convective-diffusion equation without including the Lévêque approximation.
- The validity zones for the common approximations to the convective-diffusion equation were found through numerical modeling of mass-transport impedance at channel electrodes.
- A new method, downstream electrochemical impedance spectroscopy, is demonstrated and characterized. This method results in ideal spirals in the Nyquist representation, and a qualitative explanation of the features were given based on a numerical modeling of the phenomena.

9.2 Further work

There are numerous ways that further work can be based on the results obtained in this study. Below are a few suggestions for studies that can greatly benefit from and build on the methods developed in this work.

- The self-pressurized autoclave for high temperature aqueous electrochemistry has potential to be used for many electrochemical systems. For example, a study of temperature dependence on formic acid and glucose oxidation can be relevant.
- In a similar fashion, the study of possibly selective oxidation of glycerol to a more valuable oxidation product can be an important process that can combine a fuel cell utilizing glycerol with the benefit of actually producing a product that is more valuable.
- With the recent development of stable alkaline membranes, a natural expansion would be to study and characterize anode processes in alkaline environment.
- The combination of dEIS with cyclic voltammetry is still a relatively new experimental procedure. The dEIS method may be combined with techniques such as chronoamperometry to expand the current knowledge and lay the foundation for a more complete theory of platinum oxidation and platinum oxide reduction.
- A natural development of dEIS characterization is to expand the method to be used efficiently on more complicated systems such as methanol oxidation and glycerol oxidation. The simultaneous measurement of conventional voltammetry and dynamic impedance can provide important insights into the reaction and the rate-determining steps.

- The now well-characterized microfluidic flow cells has potential as an electroanalytical tool and can be used in the study of methanol oxidation. For example, detection of formic acid on a palladium electrode has been suggested as a potential system for product detection.
- A natural development of the microfluidic system would be to incorporate supported nanoparticle catalysts for kinetic investigations.
- The microfluidic flow cells can be combined with spectroscopic techniques like EQCM, DEMS, and FTIR to provide a controlled study of flow and geometry influence on the reactions such as methanol oxidation.

Bibliography

[1] J. Twidell and J. Weir, *Renewable Energy Resources*, Routledge London and New York, 2015.

[2] E. M. Erickson, C. Ghanty, and D. Aurbach, New Horizons for Conventional Lithium Ion Battery Technology, *The Journal of Physical Chemistry Letter*, 5, (2014), pp. 3313–3324.

[3] C. K. Dyer, Fuel cells for portable applications, *Journal of Power Sources*, 106, (2002), pp. 31–34.

[4] H. Corti and E. R. Gonzales (eds.), *Direct Alcohol Fuel Cells*, Springer Dordrecht Heidelberg New York London, 2014.

[5] H. Nonaka and Y. Matsumura, Electrochemical oxidation of carbon monoxide, methanol, formic acid, ethanol, and acetic acid on a platinum electrode under hot aqueous conditions, *Journal of Electroanalytical Chemistry*, 520(1-2), (2002), pp. 101–110.

[6] T. Iwasita, Electrocatalysis of methanol oxidation, *Electrochimica Acta*, 47(22-23), (2002), pp. 3663–3674.

[7] J. L. Cohen, D. J. Volpe, and H. D. Abruna, Electrochemical determination of activation energies for methanol oxidation on polycrystalline platinum in acidic and alkaline electrolytes, *Phys. Chem. Chem. Phys.*, 9, (2007), pp. 49–77.

[8] M. Chojak-Halseid, Z. Jusys, and R. J. Behm, Methanol Oxidation Over a Pt/C Catalyst at High Temperatures and Pressure: An Online Electrochemical Mass Spectrometry Study, *The Journal of Physical Chemistry C*, 114(51), (2010), pp. 22573–22581.

[9] E. Antolini and E. Gonzalez, Alkaline direct alcohol fuel cells, *Journal of Power Sources*, 195, (2010), pp. 3431–3450.

[10] P. K. Dahlstrøm, D. A. Harrington, and F. Seland, Kinetic study of CO oxidation on clean and oxidized Pt, *Electrochimica Acta*, 82, (2012), pp. 550–557.

[11] O. Petry, B. Podlovchenko, A. Frumkin, and H. Lal, The behaviour of platinized-platinum and platinum-ruthenium electrodes in methanol solutions, *Journal of Electroanalytical Chemistry (1959)*, 10(4), (1965), pp. 253–269.

[12] H. A. Gasteiger, N. Marković, P. N. Ross, and E. J. Cairns, Temperature-Dependent Methanol Electro-Oxidation on Well-Characterized Pt-Ru Alloys, *Journal of The Electrochemical Society*, 141(7), (1994), pp. 1795–1803.

[13] A. N. Kuznetsov, P. A. Simonov, V. I. Zaikovskii, V. N. Parmon, and E. R. Savinova, Temperature effects in carbon monoxide and methanol electrooxidation on platinum–ruthenium: influence of grain boundaries, *Journal of Solid State Electrochemistry*, 17, (2013), pp. 1903–1912.

[14] H. Baltruschat, Differential electrochemical mass spectrometry, *Journal of the American Society for Mass Spectrometry*, 15(12), (2004), pp. 1693–1706.

[15] S. Sun, M. Chojak-Halseid, M. Heinen, Z. Jusys, and R. J. Behm, Ethanol electrooxidation on a carbon-supported Pt catalyst at elevated temperature and pressure: A high-temperature/high-pressure DEMS study, *Journal of Power Sources*, 190(1), (2009), pp. 2–13.

[16] Y. Kwon, K. J. P. Schouten, and M. T. M. Koper, Mechanism of the Catalytic Oxidation of Glycerol on Polycrystalline Gold and Platinum Electrodes, *ChemCatChem*, 3, (2011), pp. 1176–1185.

[17] B. Beden, M. C. Morin, F. Hahn, and C. Lamy, Insitu Analysis by Infrared Reflectance Spectroscopy of the Adsorbed Species Resulting from the Electrosorption of Ethanol on Platinum in Acid-Medium, *Journal of Electroanalytical Chemistry*, 229(1-2), (1987), pp. 353–366.

[18] B. Beden, F. Hahn, S. Juanto, C. Lamy, and J.-M. Leger, Infrared spectroscopic study of the methanol adsorbates at a platinum electrode: Part I. Influence of the bulk concentration of methanol upon the nature of the adsorbates, *Journal of Electroanalytical Chemistry and Interfacial Electrochemistry*, 225(1-2), (1987), pp. 215–225.

[19] J. Schnaidt, M. Heinen, D. Denot, Z. Jusys, and R. Behm, Electrooxidation of glycerol studied by combined in situ IR sepctroscopy and online mass spectrometry under continuous flow conditions, *Journal of Electroanalytical Chemistry*, 661, (2011), pp. 250–264.

[20] G. Graham, W. Weber, J. McBride, and C. Peters, Raman investigation of simple and complex oxides of platinum, *Journal of Raman Spectroscopy*, 22, (1991), pp. 1–9.

[21] T. J. Schmidt, M. Noeske, H. A. Gasteiger, R. J. Behm, P. Britz, and H. Bönnemann, PtRu Alloy Colloids as Precursors for Fuel Cell Catalysts: A Combined XPS, AFM, HRTEM, and RDE Study, *Journal of The Electrochemical Society*, 145(3), (1998), pp. 925–931.

[22] A. S. Aricò, A. Shukla, H. Kim, S. Park, M. Min, and V. Antonucci, An XPS study on oxidation states of Pt and its alloys with Co and Cr and its relevance to electroreduction of oxygen, *Applied Surface Science*, 172, (2001), pp. 33–40.

[23] C. P. Wilde and M. Zhang, Chemisorption and oxidation of methanol at polycrystalline Pt in acid solutions, *Electrochimica Acta*, 39(3), (1994), pp. 347–354.

[24] G. Jerkiewicz, G. Vatankhah, J. Lessard, M. P. Soriaga, and Y.-S. Park, Surface-oxide growth at platinum electrodes in aqueous H2SO4: Reexamination of its mechanism through combined cyclic-voltammetry, electrochemical quartz-crystal nanobalance, and Auger electron spectroscopy measurements, *Electrochimica Acta*, 49, (2004), pp. 1451–1459.

[25] D. A. Harrington, Ac voltammetry for measurement of surface kinetics, *Journal of Electroanalytical Chemistry*, 355, (1993), pp. 21–35.

[26] M. E. van der Geest, N. J. Dangerfield, and D. A. Harrington, An ac voltammetry study of Pt oxide growth, *Journal of Electroanalytical Chemistry*, 420, (1997), pp. 89–100.

[27] R. L. Sacci, *Electrooxidation of carbon monoxide and formic acid on polycrystalline palladium p. 48*, Ph.D. thesis, University of Victoria, 2006.

[28] A. Sun, J. Franc, and D. D. Macdonald, Growth and Properties of Oxide Films on Platinum I. EIS and X-Ray Photoelectron Spectroscopy Studies, *Journal of The Electrochemical Society*, 153, (2006), pp. B260–B277.

[29] F. Seland, R. Tunold, and D. A. Harrington, Impedance study of formic acid oxidation on platinum electrodes, *Electrochimica Acta*, 53(23), (2008), pp. 6851–6864.

[30] J.-B. Park and S.-M. Park, Fourier transform electrochemical impedance spectroscopy studies on platinum electrodes in an acidic medium, *Journal of Electroanalytical Chemistry*, 656, (2011), pp. 243–251.

[31] J.-M. Leger, B. Beden, C. Lamy, and S. Bilmes, Carbon monoxide electrosorption on low index platinum single crystal electrodes, *Journal of Electroanalytical Chemistry and Interfacial Electrochemistry*, 170(1-2), (1984), pp. 305–317.

[32] M. Markovic, T. J. Schmidt, B. N. Grgur, H. A. Gasteiger, R. J. Behm, and P. N. Ross, Effect of Temperature on Surface Processes at the Pt(111) - Liquid Interface: Hydrogen Adsorption, Oxide Formation, and CO Oxidation, *The Journal of Physical Chemistry B*, 103(40), (1999), pp. 8568–8577.

[33] N. Tian, Z.-Y. Zhou, S.-G. Sun, Y. Ding, and Z. L. Wang, Synthesis of Tetrahexahedral Platinum Nanocrystals with High-Index Facets and High Electro-Oxidation Activity, *Science*, 316(5825), (2007), pp. 732–735.

[34] S. W. Lee, S. Chen, W. Sheng, N. Yabuuchi, Y.-T. Kim, T. Mitani, E. Vescovo, and Y. Shao-Horn, Roles of Surface Steps on Pt Nanoparticles in Electro-oxidation of Carbon Monoxide and Methanol, *Journal of the American Chemical Society*, 131(43), (2009), pp. 15669–15677.

[35] M. Neurock, M. Janik, and A. Wieckowski, A first principles comparison of the mechanism and site requirements for the electrocatalytic oxidation of methanol and formic acid over Pt, *Faraday Discuss.*, 140, (2009), pp. 363–378.

[36] M. Alsabet, M. Grden, and G. Jerkiewicz, Comprehensive study of the growth of thin oxide layers on Pt electrodes under well-defined temperature, potential, and time conditions, *Journal of Electroanalytical Chemistry*, 589(1), (2006), pp. 120–127.

[37] R. Cowan and A. Kaznoff, Electrochemical Measurements of Corrosion Processes in a Boiling Water Nuclear Reactor, *Corrosion (Houston, TX, United States)*, 29, (1973), pp. 123–132.

[38] B. Case and G. Bignold, The mercury/mercuric oxide electrode in high temperature aqueous solutions, *Journal of Applied Electrochemistry*, 1, (1971), pp. 141–146.

[39] D. D. Macdonald, Reference Electrodes for High Temperature Aqueous Systems - A Review and Assessment, *Corrosion (Houston, TX, United States)*, 34, (1978), pp. 75–84.

[40] D. D. Macdonald, A. Scott, and P. Wentrcek, External Reference Electrodes for Use in High Temperature Aqueous Systems, *Journal of The Electrochemical Society*, 126, (1979), pp. 908–911.

[41] S. Hettiarachchi, P. Kedzierawski, and D. D. Macdonald, pH Measurements of High Temperature Aqueous Environments with Stabilized-Zirconia Membranes, *Journal of The Electrochemical Society*, 132, (1985), pp. 1866–1870.

[42] D. Midgley, A review of pH measurement at high temperatures, *Talanta*, 37, (1990), pp. 767–781.

[43] W. Bogaerts and A. Van Haute, Determination of Activity Coefficients for KCl Elevated Temperatures, *Journal of The Electrochemical Society*, 131, (1984), pp. 68–72.

[44] A. McDonald, F.-R. Fan, and A. J. Bard, Electrochemistry in near-critical and supercritical fluids. 2. Water. Experimental techniques and the copper(II) system, *Journal of Physical Chemistry*, 90, (1986), pp. 196–202.

[45] L. Trevani, E. Calvo, and H. Corti, Diffusion coefficients of iodide in high temperature aqueous solutions, *Electrochemistry Communications*, 2, (2000), pp. 312–316.

[46] Y. Chen, M. Urquidi-Macdonald, and D. D. Macdonald, The electrochemistry of zirconium in aqueous solutions at elevated temperatures and pressures, *Journal of Nuclear Materials*, 348, (2006), pp. 133–147.

[47] A. J. Bard, W. Flarsheim, and K. Johnston, High-Pressure Electrochemical Oxidation of Benzene at a Lead Dioxide Electrode in Aqueous Bisulfate Solutions at 25°C to 250°C, *Journal of The Electrochemical Society*, 135, (1988), pp. 1939–1944.

[48] D. Bokach, J. L. G. de la Fuente, M. Tsypkin, P. Ochal, I. C. Endsjø, R. Tunold, S. Sunde, and F. Seland, High-Temperature Electrochemical Characterization of Ru Core Pt Shell Fuel Cell Catalyst, *Fuel Cells*, 11(6), (2011), pp. 735–744.

[49] A. P. M. Camargo, B. A. F. Previdello, H. Varela, and E. R. Gonzales, Effect of temperature on the electro-oxidation of ethanol on platinum, *Quimica Nova*, 33, (2010), pp. 2143–2147.

[50] R. Sacci and D. Harrington, Dynamic Electrochemical Impedance Spectroscopy, *ECS Transactions*, 19, (2009), pp. 31–42.

[51] R. Sacci, F. Seland, and D. Harrington, Dynamic electrochemical impedance spectroscopy, for electrocatalytic reactions, *Electrochimica Acta*, 131, (2014), pp. 13–19.

[52] P. N. Nge, C. I. Rogers, and A. T. Woolley, Advances in Microfluidic Materials, Functions, Integration, and Applications, *Chemical Reviews*, 113, (2013), pp. 2550–2583.

[53] E. Kjeang, N. Djilali, and D. Sinton, Microfluidic fuel cells: A review, *Journal of Power Sources*, 186(2), (2009), pp. 353–369.

[54] C. Brett, A. Oliveira-Brett, E. C. Bamford, and E. R. Compton, *Comprehensive Chemical Kinetics*, vol. 26, chap. Hydrodynamic electrodes, pp. 355–441, Elsevier, 1986.

[55] J. Cooper and R. Compton, Channel Electrodes: A Review, *Electroanalysis*, 10(3), (1998), pp. 141–155.

[56] Comsol Inc, COMSOL Multiphysics v 5.1 http://www.comsol.com, 2015, burlington, MA.

[57] Maple v 18.01, Maplesoft, a division of Waterloo Maple Inc., Waterloo, Ontario http://www.maplesoft.com, 2014.

[58] T. Holm, S. Sunde, F. Seland, and D. A. Harrington, A semianalytical method for simulating mass transport at channel electrodes, *Journal of Electroanalytical Chemistry*, 745, (2015), pp. 72–79.

[59] Comsol Inc, COMSOL Multiphysics v 5.0 http://www.comsol.com, 2014, burlington, MA.

[60] T. Holm, M. Ingdal, E. V. Fanavoll, S. Sunde, F. Seland, and D. A. Harrington, Mass-transport impedance at channel electrodes: accurate and approximate solutions, *Electrochimica Acta*, 202, (2016), pp. 84–89.

[61] M. Ingdal, *Micro-fluidic flow cells for studies of electrochemical reactions*, Master's thesis, Norwegian University of Science and Technology, NTNU, 2014.

[62] D. Pletcher, R. Greff, R. Peat, L. Peter, and J. Robinson, *Instrumental Methods in Electrochemistry*, Woodhead Publishing, Philadelphia, PA, 2011.

[63] R. G. Compton and C. Banks, *Understanding Voltammetry*, World Scientific Publishing, Singapore, 2nd edn., 2011.

[64] M. E. Orazem and B. Tribollet, *Electrochemical impedance spectroscopy*, vol. 48, John Wiley & Sons, 2011.

[65] A. Lasia, *Electrochemical Impedance Spectroscopy and its Applications*, Springer London, 2014.

[66] G. Popkirov and R. Schindler, Effect of sample nonnonlinear on the performance of time domain electrochemical impedance spectroscopy, *Electrochimica Acta*, 40, (1995), pp. 2511–2517.

[67] G. Popkirov, Fast time-resolved electrochemical impedance spectroscopy for investigations under nonstationary conditions, *Electrochimica Acta*, 41, (1996), pp. 1023–1027.

[68] D. D. Macdonald, The Electrochemistry of Metals in Aqueous Systems at Elevated Temperatures, *Modern Aspects of Electrochemistry*, 11, (1975), pp. 141–197.

[69] G. Wildgoose, D. Giovanelli, N. Lawrence, and R. Compton, High-Temperature Electrochemistry: A Review, *Electroanalysis*, 16, (2004), pp. 421–433.

[70] P. Gründler, A. Kirbs, and L. Dunsch, Modern Thermoelectrochemistry, *ChemPhysChem*, 10(11), (2009), pp. 1722–1746.

[71] P. Gründler, *In-situ Thermoelectrochemistry*, Springer Heidelberg New York Dordrecht London, 2015.

[72] P. K. Dahlstrøm, *Electro-oxidation of small organic molecules*, Ph.D. thesis, Norwegian University of Science and Technology, 2012.

[73] M. Umeda, H. Sugii, and I. Uchida, Alcohol electrooxidation at Pt and Pt-Ru sputtered electrodes under elevated temperature and pressurized conditions, *Journal of Power Sources*, 179, (2008), pp. 489–496.

[74] H. Liu, C. Song, L. Zhang, J. Zhang, H. Wang, and D. P. Wilkinson, A review of anode catalysis in the direct methanol fuel cell, *Journal of Power Sources*, 155, (2006), pp. 95–110.

[75] R. Behm and Z. Jusys, The potential of model studies for the understanding of catalyst poisoning and temperature effects in polymer electrolyte fuel cell reactions, *Journal of Power Sources*, 154(2), (2006), pp. 327–342.

[76] A. S. Aricò, V. Baglio, A. Di Blasi, V. Antonucci, L. Cirillo, G. A., and V. Arcella, Proton exchange membranes based on the short-side-chain perfluorinated ionomer for high temperature direct methanol fuel cells, *Desalination*, 199, (2006), pp. 271–273.

[77] H. Xu, Y. Song, H. Kunz, and J. Fenton, Operation of PEM fuel cells at 120-150C to improve CO tolerance, *Journal of Power Sources*, 159, (2006), pp. 979–986.

[78] A. Pitois, A. Pilenga, and G. Tsotridis, CO desorption kinetics at concentrations and temperatures relevant to PEM fuel cells operating with reformate gas and PtRu/C anodes, *Applied Catalysis A: General*, 374, (2010), pp. 95–102.

[79] S.-H. Yang, C.-Y. Chen, and W.-J. Wang, An impedance study of an operating direct methanol fuel cell, *Journal of Power Sources*, 195, (2010), pp. 2319–2330.

[80] J. Zhang, Z. Xie, J. Zhang, Y. Tang, C. Song, T. Navessin, Z. Shi, D. Song, H. Wang, D. P. Wilkinson, Z.-S. Liu, and S. Holdcroft, High temperature PEM fuel cells, *Journal of Power Sources*, 160, (2006), pp. 872–891.

[81] M. Khandelwal and M. M. Mench, Direct measurement of through-plane thermal conductivity and contact resistance in fuel cell materials, *Journal of Power Sources*, 161, (2006), pp. 1106–1115.

[82] A. Chandan, M. Hattenberger, A. El-kharouf, S. Du, A. Dhir, V. Self, B. G. Pollet, A. Ingram, and W. Bujalsko, High temperature (HT) polymer electrolyte membrane fuel cells (PEMFC) - A review, *Journal of Power Sources*, 231, (2013), pp. 264–278.

[83] C. Yang, P. Costamagna, S. Srinivasan, J. Benzinger, and A. Bocarsly, Approaches and technical challenges to high temperature operation of proton exchange membrane fuel cells, *Journal of Power Sources*, 103, (2001), pp. 1–9.

[84] N. Djilali and D. Lu, Influence of heat transfer on gas and water transport in fuel cells, *International Journal of Thermal Sciences*, 41, (2002), pp. 29–40.

[85] C. Quispe, C. Coronado, and J. A. Carvalho Jr., Glycerol: Production, consumption, prices, characterization and new trends in combustion, *Renewable and Sustainable Energy Reviews*, 27, (2013), pp. 475–493.

[86] V. Protsenko and F. Danilov, Activation energy of electrochemical reaction measured at a constant value of electrode potential, *Journal of Electroanalytical Chemistry*, 651, (2011), pp. 105–110.

[87] B. E. Conway and D. P. Wilkinson, Non-isothermal cell potentials and evaluation of entropies of ions and of activation for single electrode processes in non-aqueous media, *Electrochimica Acta*, 38, (1993), pp. 997–1013.

[88] B. Conway, Electrochemical oxide film formation at noble metals as a surface-chemical process, *Progress in Surface Science*, 49(4), (1995), pp. 331–452.

[89] R. Parsons and T. VanderNoot, The oxidation of small organic molecules: A survey of recent fuel cell related research, *Journal of Electroanalytical Chemistry and Interfacial Electrochemistry*, 257(1-2), (1988), pp. 9–45.

[90] S. Wasmus and A. Küver, Methanol oxidation and direct methanol fuel cells: a selective review, *Journal of Electroanalytical Chemistry*, 461(1-2), (1999), pp. 14–31.

[91] E. Herrero, W. Chrzanowski, and A. Wieckowski, Dual Path Mechanism in Methanol Electrooxidation on a Platinum Electrode, *The Journal of Physical Chemistry*, 99(25), (1995), pp. 10423–10424.

[92] S. Liu, L. Liao, Q. Tao, Y. Chen, and S. Ye, The kinetics of CO pathway in methanol oxidaiton at Pt electrodes, a quantitative study by ATR-FTIRS spectroscopy, *Phys. Chem. Chem. Phys.*, 13, (2011), pp. 9725–9735.

[93] H. Wang, T. Löffler, and H. Baltruschat, Formation of intermediates during methanol oxidation: A quantitative DEMS study, *Journal of Applied Electrochemistry*, 31(7), (2001), pp. 759–765.

[94] T. H. M. Housmans, A. H. Wonders, and M. T. M. Koper, Structure Sensitivity of Methanol Electrooxidation Pathways on Platinum: An On-Line Electrochemical Mass Spectrometry Study, *The Journal of Physical Chemistry B*, 110(20), (2006), pp. 10021–10031.

[95] S. Celik and M. D. Mat, Measurement and estimation of species distribution in a direct methanol fuel cell, *International Journal of Hydrogen Energy*, 35(5), (2010), pp. 2151–2159.

[96] F. Seland, R. Tunold, and D. A. Harrington, Impedance study of methanol oxidation on platinum electrodes, *Electrochimica Acta*, 51(18), (2006), pp. 3827–3840.

[97] F. Seland, R. Tunold, and D. A. Harrington, Activating and deactivating mass transport effects in methanol and formic acid oxidation on platinum electrodes, *Electrochimica Acta*, 55(9), (2010), pp. 3384–3391.

[98] D. Kardash, J. Huang, and C. Korzeniewski, Surface Electrochemistry of CO and Methanol at 25-75 °C Probed in Situ by Infrared Spectroscopy, *Langmuir*, 16(4), (2000), pp. 2019–2023.

[99] B. Beden, I. Cetin, A. Kahyaoglu, D. Takky, and C. Lamy, Electrocatalytic oxidation of saturated oxygenated compounds on gold electrodes, *Journal of Catalysis*, 104(1), (1987), pp. 37–46.

[100] F. Seland, D. A. Harrington, and R. Tunold, Fast methanol oxidation on polycrystalline Pt, *Electrochimica Acta*, 52(3), (2006), pp. 773–779.

[101] H. A. Gasteiger, N. Markovic, P. N. Ross, and E. J. Cairns, Methanol electrooxidation on well-characterized platinum-ruthenium bulk alloys, *The Journal of Physical Chemistry*, 97(46), (1993), pp. 12020–12029.

[102] A. Cuesta, At Least Three Contiguous Atoms Are Necessary for CO Formation during Methanol Oxidation on Platinum, *Journal of the American Chemical Society*, 128, (2006), pp. 13332–13333.

[103] N. Wakabayashi, H. Uchida, and M. Watanabe, Temperature-Dependence of Methanol Oxidation Rates at PtRu and Pt Electrodes, *Electrochemical and Solid-State Letters*, 5(11), (2002), pp. E62–E65.

[104] T. Iwasita and Z. Xia, Adsorption of water at Pt(111) electrode in $HClO_4$ solutions. The potential of zero charge, *Journal of Electroanalytical Chemistry*, 411, (1996), pp. 95–102.

[105] A. B. Anderson and T. Albu, Catalytic Effect of Platinum on Oxygen Reduction - An Ab Initio Model Including Electrode Potential Dependence, *Journal of The Electrochemical Society*, 147, (2000), pp. 4229–4238.

[106] J. Rossmeisl, J. Nørskov, C. Taylor, M. Janik, and M. Neurock, Calculated Phase Diagrams for the Electrochemical Oxidation and Reduction of Water over Pt(111), *Journal of Physical Chemistry B*, 110, (2006), pp. 21833–21839.

[107] V. Viswanathan, H. Hansen, J. Rossmeisl, T. Jaramillo, H. Pitsch, and J. Nørskov, Simulating Linear Sweep Voltammetry from First-Principles: Application to Electrochemical Oxidation of Water on Pt(111) and Pt3Ni(111), *The Journal of Physical Chemistry C*, 116, (2012), pp. 4698–4704.

[108] Y. Chen, A. Miki, S. Ye, H. Sakai, and M. Osawa, Formate, an Active Intermediate for Direct Oxidation of Methanol on Pt Electrode, *Journal of the American Chemical Society*, 125, (2003), pp. 3680–3681.

[109] J. F. Gomes and G. Tremiliosi-Filho, Spectroscopic Studies of the Glycerol Electro-Oxidation on Polycrystalline Au and Pt Surfaces in Acidic and Alkaline Media, *Electrocatalysis*, 2, (2011), pp. 96–105.

[110] P. Fernández, C. Martins, M. Martins, and G. Camara, Electrooxidation of glycerol on platinum nanoparticles: Deciphering how the position of each carbon affects the oxidation pathways, *Electrochimica Acta*, 112, (2013), pp. 686–691.

[111] J. F. Gomes, F. B. C. de Paula, L. H. S. Gasparotto, and G. Tremiliosi-Filho, The influence of the Pt crystalline surface orientation on the glycerol electro-oxdiation in acidic media, *Electrochimica Acta*, 76, (2012), pp. 88–93.

[112] J. F. Gomes, C. Marins, M. Janete Giz, G. Tremiliosi-Filho, and G. Camara, Insights into the adsorption and electro-oxidation of glycerol: Self-inhibition and concentration effects, *Journal of Catalysis*, 301, (2013), pp. 154–161.

[113] J. F. Gomes, L. H. S. Gasparotto, and G. Tremiliosi-Filho, Glycerol electrooxidation over glassy-carbon-supported Au nanoparticles: direct influence of the carbon support on the electrode catalytic activity, *Physical Chemistry Chemical Physics*, 15, (2013), pp. 10339–10349.

[114] L. Roquet, E. M. Belgsir, J.-M. Leger, and C. Lamy, Kinetics and mechanism of the electrocatalytic oxidation of glycerol as investigated by chromatographic analysis of the reaction products: Potential and pH effects, *Electrochimica Acta*, 39, (1994), pp. 2387–2394.

[115] J.-H. Zhang, Y.-J. Liang, N. Li, Z.-Y. Li, and C.-W. Zu, A remarkable activity of glycerol electrooxidation on gold in alkaline medium, *Electrochimica Acta*, 59, (2012), pp. 156–159.

[116] L.-W. H. Leung and M. J. Weaver, Influence of Adsorbed Carbon Monoxide on the Electrocatalytic Oxidation of Simple Organic Molecules at Platinum and Palladium Electrodes in Acidic Solutions: A Survey Using Real-Time FTIR Spectroscopy, *Langmuir*, 6, (1990), pp. 323–333.

[117] C. Martins, M. Janete Giz, and G. Camara, Generation of carbon dioxide from glycerol: Evidences of massive production on polycrystalline platinum, *Electrochimica Acta*, 56, (2011), pp. 4549–4553.

[118] P. Fernández, M. Martins, and G. Camara, New insights about the electrooxidation of glycerol on platinum nanoparticles supported on multi-walled carbon nanotubes, *Electrochimica Acta*, 66, (2012), pp. 180–187.

[119] C. Martins, P. Fernández, H. Troiani, M. Martins, and G. Camara, Ethanol vs. glycerol: Understanding the lack of correlation between the oxidation currents and the production of CO_2 on Pt nanoparticles, *Journal of Electroanalytical Chemistry*, 717-718, (2015), pp. 231–236.

[120] K. Ishiyama, F. Kosaka, I. Shimada, Y. Oshima, and J. Otomo, Glycerol electrooxidation on a carbon-supported platinum catalyst at intermediate temperatures, *Journal of Power Sources*, 225, (2013), pp. 141–149.

[121] W. Chrzanowski and A. Wieckowski, Surface Structure Effects in Platinum/Ruthenium Methanol Oxidation Electrocatalysis, *Langmuir*, 14(8), (1998), pp. 1967–1970.

[122] T. H. Madden and E. M. Stuve, II. Mechanisms of Elevated Temperature Methanol Electro-oxidation and Poisoning on Pt/C-Nafion Catalyst Layers, *Journal of The Electrochemical Society*, 150(11), (2003), pp. E571–E577.

[123] M. Breiter, Comparative oxidation of chemisorbed carbon monoxide, reduced carbon dioxide and species formed during the methanol oxidation, *Journal of Electroanalytical Chemistry and Interfacial Electrochemistry*, 19(1-2), (1968), pp. 131–136.

[124] D. Chu and S. Gilman, Methanol Electro-Oxidation on Unsupported Pt-Ru Alloys at Different Temperatures, *Journal of The Electrochemical Society*, 143(5), (1996), pp. 1685–1690.

[125] J. B. Day, P.-A. Vuissoz, E. Oldfield, A. Wieckowski, and J.-P. Ansermet, Nuclear Magnetic Resonance Spectroscopic Study of the Electrochemical Oxidation Product of Methanol on Platinum Blass, *Journal of the American Chemical Society*, 118(51), (1996), pp. 13046–13050.

[126] N. M. Marković, B. N. Grgur, and P. N. Ross, Temperature-Dependent Hydrogen Electrochemistry on Platinum Low-Index Single-Crystal Surfaces in Acid Solutions, *The Journal of Physical Chemistry B*, 101(27), (1997), pp. 5405–5413.

[127] A. B. Anderson, N. Neshev, R. Sidik, and P. Shiller, Mechanism for the electrooxidation of water to OH and O bonded to platinum: quantum chemical theory, *Electrochimica Acta*, 47, (2002), pp. 2999–3008.

[128] T. Kobayashi, P. Babu, J. Chung, E. Oldfield, and A. Wieckowski, Coverage Dependence of CO Surface Diffusion on Pt Nanoparticles: An EC-NMR Study, *Journal of Physical Chemistry C*, 111, (2007), pp. 7078–7083.

[129] B. E. Conway and T. C. Liu, Examination of Electrocatalysis in the Anodic O2 Evolution Reaction at Pt through Evaluation of the Adsorption Behaviour of Kinetically Involved Intermediate States, *Proceedings of the Royal Society of London. A. Mathematical and Physical Sciences*, 429(1877), (1990), pp. 375–397.

[130] W. Visscher and M. A. V. Devanathan, Anodic behavior of platinum electrodes in oxygen-saturated acid solutions, *Journal of Electroanalytical Chemistry*, 8, (1964), pp. 127–138.

[131] G. Ragoisha, N. P. Osipovich, A. S. Bondarenko, J. Zhang, S. Kocha, and A. Iiyama, Characterisation of the electrochemical redox behaviour of Pt electrodes by potentiodynamic electrochemical impedance spectroscopy, *Journal of Solid State Electrochemistry*, 14, (2010), pp. 531–542.

[132] G. S. Popkirov and R. N. Schindler, Optimization of the perturbation signal for electrochemical impedance spectroscopy in the time domain, *Review of Scientific Instruments*, 64, (1993), pp. 3111–3115.

[133] J. B. Benziger, F. A. Pascal, S. L. Bernasek, M. P. Soriaga, and A. T. Hubbard, Characterization of platinum electrodes by infrared spectroscopy, *Journal of Electroanalytical Chemistry and Interfacial Electrochemistry*, 198, (1986), pp. 65–80.

[134] M. W. Breiter, Impedance on platinum from voltammetry with superimposed alternating voltage, *Journal of Electroanalytical Chemistry (1959)*, 7, (1964), pp. 38–49.

[135] S. Gilman, Electrochemical surface oxidation of platinum, *Electrochimica Acta*, 9, (1964), pp. 1025–1046.

[136] D. V. Heyd and D. A. Harrington, Platinum oxide growth kinetics for cyclic voltammetry, *Journal of Electroanalytical Chemistry*, 335(1-2), (1992), pp. 19–31.

[137] G. Brug, A. van den Eeden, M. Sluyters-Rehbach, and J. Sluyters, The analysis of electrode impedances complicated by the presence of a constant phase element, *Journal of Electroanalytical Chemistry and Interfacial Electrochemistry*, 176, (1984), pp. 275–295.

[138] B. Hirschorn, M. E. Orazem, B. Tribollet, V. Vivier, I. Frateur, and M. Musiani, Determination of effective capacitance and film thickness from constant-phase-element parameters, *Electrochimica Acta*, 55, (2010), pp. 6218–6227.

[139] W. Pell, A. Zolfaghari, and B. E. Conway, Capacitance of the double-layer at polycrystalline Pt electrodes bearing a surface-oxide film, *Journal of Electroanalytical Chemistry*, 532, (2002), pp. 13–23.

[140] J. Newman and E. A. Bard, *Electroanalytical Chemistry*, vol. 6, chap. Sec. XVII, p. 187, Marcel Dekker NY, 1973.

[141] S. Moldoveanu and J. Anderson, Amperometric response of a rectangular channel electrode, *Journal of Electroanalytical Chemistry and Interfacial Electrochemistry*, 175, (1984), pp. 67–77.

[142] S. Schmächtel and K. K. Kontturi, Transient solutions of potential steps at the rotating disc electrode with steady state initial concentration profiles for one electron transfer reactions, *Electrochimica Acta*, 56(19), (2011), pp. 6812–6823.

[143] J. L. Troutman and M. Bautista, *Boundary value problem of applied mathematics*, PWS Publishing Company, 1994.

[144] Comsol Inc, COMSOL Multiphysics v 4.4 http://www.comsol.com, 2013, burlington, MA.

[145] K. B. Oldham and S. W. Feldberg, Principle of Unchanging Total Concentration and Its Implications for Modeling Unsupported Transient Voltammetry, *Journal of Physical Chemistry B*, 103, (1999), pp. 1699–1704.

[146] D. A. Harrington, Rules to transform concentrations and currents for irreversible reactions to those of quasireversible reactions, *Electrochim. Acta*, 152, (2015), pp. 308–314.

[147] R. Braun, Mass transport on a double electrode in flow channel walls, *Journal of Electroanalytical Chemistry*, 19, (1968), p. 23.

[148] K. Aoki, K. Tokuda, and H. Matsuda, Hydrodynamic voltammetry at channel electrodes: Part IX. Edge effects at rectangular channel flow microelectrodes, *Journal of Electroanalytical Chemistry and Interfacial Electrochemistry*, 217(1), (1987), pp. 33–47.

[149] R. G. Compton, A. C. Fisher, R. G. Wellington, P. J. Dobson, and P. A. Leigh, Hydrodynamic voltammetry with microelectrodes: channel microband electrodes; theory and experiment, *The Journal of Physical Chemistry*, 97(40), (1993), pp. 10410–10415.

[150] J. A. Alden and R. G. Compton, Microband Electrodes of Ideal and Nonideal Geometries: AC Impedance Spectroscopy, *Electroanalysis*, 8(1), (1996), pp. 30–33.

[151] C. Amatore, N. Da Mota, C. Sella, and L. Thouin, Theory and Experiments of Transport at Channel Microband Electrodes under Laminar Flows. 1. Steady-State Regimes at a Single Electrode, *Analytical Chemistry*, 79(22), (2007), pp. 8502–8510.

[152] J. Oldham, J. Myland, and A. Bond, *Electrochemical Science and Technology: Fundamental and Applications*, Wiley, Chichester, UK, 2012.

[153] D. Zwillinger, *Handbook of Differential Equations*, Academic Press, San Diego, 2nd edn., 1992.

[154] F. Olver, D. Lozier, R. Boisvert, and C. Clark, *NIST Handbook of Mathematical Functions*, NIST and Cambridge University Press, NY, Sec. 13.14, 2010.

[155] A. Gencoglu and A. R. Minerick, Electrochemical detection techniques in micro- and nanofluidic devices, *Microfluidics and Nanofluidics*, 17, (2014), pp. 781–807.

[156] E. J. F. Dickinson, H. Ekström, and E. Fontes, COMSOL Multiphysics®: Finite element software for electrochemical analysis. A mini-review, *Electrochemistry Communications*, 40, (2014), pp. 71–74.

[157] L. K. Bieniasz, Theory of Potential Step Chronoamperometry at a Microband Electrode: Complete Explicit Semi-Analytical Formulae for the Faradaic Current Density and the Faradaic Current, *Electrochimica Acta*, 178, (2015), pp. 25–33.

[158] L. K. Bieniasz, Highly accurate, inexpensive procedures for computing theoretical chronoamperometric ccurrent at single straight electrode edges and at single microband electrodes, *Journal of Electroanalytical Chemistry*, 760, (2016), pp. 71–79.

[159] R. V. Homsy and J. Newman, An Asymptotic Solution for the Warburg Impedance of a Rotating Disk Electrode, *Journal of The Electrochemical Society*, 121(4), (1974), pp. 521–523.

[160] E. Levart and D. Schuhmann, Comparison of Some Solutions for the Warburg Impedance of a Rotating Disk Electrode, *Journal of The Electrochemical Society*, 122(8), (1975), pp. 1082–1083.

[161] E. Levart and J. Newman, Discussion of "The Warburg Impedance in the Presence of Convective Flow", *Journal of the Electrochemical Society*, 127(12), (1980), pp. 2649–2650.

[162] D. A. Scherson and J. Newman, The Warburg Impedance in the Presence of Convective Flow, *Journal of the Electrochemical Society*, 127(1), (1980), pp. 110–113.

[163] C. Deslouis, C. Gabrielli, and B. Tribollet, An Analytical Solution of the Nonsteady Convective Diffusion Equation for Rotating Electrodes, *Journal of The Electrochemical Society*, 130(10), (1983), pp. 2044–2046.

[164] B. Tribollet and J. Newman, Analytic Expression of the Warburg Imepdance for a Rotating Disk Electrode, *Journal of the Electrochemical Society*, 130(4), (1983), pp. 822–824.

[165] E. Levart and D. Schuhmann, Sur la determination generale du comportement transitoire d'une electrode a disque tournant soumise a une perturbation electrique de faible amplitude, *Journal of Electroanalytical Chemistry and Interfacial Electrochemistry*, 28(1), (1970), pp. 45–56.

[166] R. Morris and W. Smyrl, Rigorous Treatment of Rotating Disk Electrode Impedance Data Over the Entire Frequency Range, *Journal of The Electrochemical Society*, 137(2), (1990), pp. 406–411.

[167] B. A. Coles and R. G. Compton, The theory of EC reactions at tubular electrodes, *Journal of Electroanalytical Chemistry and Interfacial Electrochemistry*, 127, (1981), pp. 37–42.

[168] R. G. Compton and G. R. Sealy, The theory of the ac voltammetry of reversible electrode processes at tubular electrodes, *Journal of Electroanalytical Chemistry and Interfacial Electrochemistry*, 145(1), (1983), pp. 35–41.

[169] R. G. Compton, M. E. Laing, and P. R. Unwin, AC Impedance measurements at channel electrodes the effect of convection, *Journal of Electroanalytical Chemistry and Interfacial Electrochemistry*, 207, (1986), pp. 309–314.

[170] J. Alden and R. Compton, Hydrodynamic voltammetry with channel microband electrodes: axial diffusion effects, *Journal of Electroanalytical Chemistry*, 404(1), (1996), pp. 27–35.

[171] R. G. Compton and J. Winkler, Hydrodynamic Voltammetry with Channel Microband Electrodes: Alternating Current Impedance Measurements, *Journal of Physical Chemistry*, 99(14), (1995), pp. 5029–5034.

[172] S. M. Matthews, M. J. A. Shiddiky, K. Yunus, D. M. Elton, N. W. Duffy, Y. Gu, A. C. Fisher, and A. M. Bond, Attributes of Direct Current Aperiodic and Alternating Current Harmonic Components Derived From Large Amplitude Fourier Transformed Voltammetry Under Microfluidic Control in a Channel Electrode, *Analytical Chemistry*, 84, (2012), pp. 6686–6692.

[173] Y. Hoshi, M. Ohya, I. Shitanda, and M. Itagaki, Diffusion Impedance of Microband Electrode Array By FEM, in *224th ECS Meeting (October 27-November 1, 2013)*, Ecs, 2013.

[174] C. Gabrielli, M. Keddam, N. Portail, P. Rousseau, H. Takenouti, and V. Vivier, Electrochemical Impedance Spectroscopy Investigations of a Microelectrode Behavior in a Thin-Layer Cell: Experimental and Theoretical Studies, *The Journal of Physical Chemistry B*, 110(41), (2006), pp. 20478–20485.

[175] E. Kjeang, B. Roesch, J. McKechnie, D. A. Harrington, N. Djilali, and D. Sinton, Integrated electrochemical velocimetry for microfluidic devices, *Microfluidics and Nanofluidics*, 3(4), (2007), pp. 403–416.

[176] T. Jacobsen and K. West, Diffusion impedance in planar, cylindrical and spherical symmetry, *Electrochimica Acta*, 40(2), (1995), pp. 255 – 262.

[177] M. E. Orazem and B. Tribollet, *Electrochemical impedance spectroscopy, p. 185-186*, John Wiley & Sons, 2011.

[178] Y. Wang, J. G. Limon-Petersen, and R. G. Compton, Measurement of the diffusion coefficients of [Ru(NH3)6]3+ and [Ru(NH3)6]2+ in aqueous solution using microelectrode double potential step chronoamperometry, *Journal of Electroanalytical Chemistry*, 652(1-2), (2011), pp. 13–17.

[179] The MathWorks Inc, MATLAB R2013b http://mathworks.com/products/matlab, 2013, natick, MA.

[180] S. M. H. Hashemi, M. A. Modestino, and D. Psaltis, A membrane-less electrolyzer for hydrogen production across the pH scale, *Energy & Environmental Science*, 8, (2015), pp. 2003–2009.

[181] D. G. Rackus, M. H. Shamsi, and A. R. Wheeler, Electrochemistry, biosensors and microfluidics: a convergence of fields, *Chemical Society Reviews*, 44, (2015), pp. 5320–5340.

[182] J. Anderson and S. Moldoveanu, Numerical simulation of convective diffusion at a rectangular channel flow electrode, *Journal of Electroanalytical Chemistry and Interfacial Electrochemistry*, 179, (1984), pp. 107–117.

[183] S. Moldoveanu and J. Anderson, Numerical simulation of convective diffusion at a microarray channel electrode, *Journal of Electroanalytical Chemistry and Interfacial Electrochemistry*, 185(2), (1985), pp. 239–252.

[184] D. K. Cope, C. H. Scott, V. Kalapathy, and D. E. Tallman, Transient behavior at planar microelectrodes: Diffusion current at a band electrode by an integral equation method. Part {II}, *Journal of Electroanalytical Chemistry and Interfacial Electrochemistry*, 280(1), (1990), pp. 27–35.

[185] C. Deslouis, B. Tribollet, and M. A. Vorotyntsev, Diffusion-Convection Impedance at Small Electrodes, *Journal of The Electrochemical Society*, 138(9), (1991), pp. 2651–2657.

[186] K. Aoki, K. Tokuda, and H. Matsuda, Hydrodynamic voltammetry at channel electrodes. Part II. Theory of first-order kinetic collection efficiencies, *Journal of Electroanalytical Chemistry*, 79, (1977), pp. 49–78.

[187] A. C. Fisher and R. G. Compton, Double-channel electrodes: Homogeneous kinetics and collection efficiency measurements, *Journal of Applied Electrochemistry*, 21, (1991), pp. 208–212.

[188] W. J. Albery, J. S. Drury, and M. L. Hitchman, Ring-Disc Electrodes - Part 12. - Application to Ring Current Transients, *Transactions of the Faraday Society*, 67, (1971), pp. 161–165.

[189] W. J. Albery, A. H. Davis, and A. J. Mason, Alternating Current and Ring-Disc Electrodes, *Faraday Discussions of the Chemical Society*, 56, (1973), pp. 317–329.

[190] D. A. Harrington, Simple relationship between limiting current and mass-transport impedance at zero frequency - submitted, *Journal of the Electrochemical Society*, -, (2016), pp. –.

[191] P. A. Kottke and A. G. Fedorov, Generalized Principles of Unchanging Total Concentration, *Journal of Physical Chemistry B*, 109, (2005), pp. 16811–16818.

[192] W. J. Albery, J. S. Drury, and A. P. Hutchinson, Ring-Disc Electrodes - Part 15. - Alternating Current Measurements, *Transactions of the Faraday Society*, 67, (1971), pp. 2414–2418.

List of Figures

List of Tables

A Maple documentation for Chapter 6

This appendix consists of the Maple worksheet used in Chapter 6. This worksheet was supplementary material for the published paper from Chapter 6 [60], and that should be consulted for the output, which was omitted here for brevity. The worksheet is divided into a setup and different parts solving the relevant problems. The parts are “Concentration profile for an irreversible reaction”, “Limiting current as a function of flow rate”, “A multisegment example”, “Collection efficiency calculation”, “Steady-state current vs potential for a quasireversible reaction - no product initially”, and “Steady-state current vs potential for a quasireversible reaction - with product initially”.

This worksheet is Supplementary material for T. Holm, S. Sunde, F. Seland and D.A. Harrington, "Simulation for channel electrodes", J. Electroanal. Chem., 2014.
Execute by entering "enter" on successive execution groups (indicated by the > prompt), or execute the entire worksheet with the "!!!" icon.
Run the Setup section first, and then the other sections can be run in any order.
This was produced in Maple 18, but should work in recent earlier versions.

Setup

This section needs to be run before any of the others. It specifies the accuracy required and defines the channel solving routine *chsolve*.

```
> restart; with(plots):
```

Find number of hardware digits on this machine. (For a 32-bit machine this will return 15)

```
> evalhf(Digits);
```

Maple can do calculations utilizing the computer hardware, with accuracy approximately the number of digits above. This is the faster way. Specifying a value for Digits less than this will automatically utilize the hardware option, and give answers approximately accurate to the number of Digits you request below. The floating-point evaluation of the integrals requires a few guard digits, so the Digits you request should be, say, 5 less than the number above. Maple can also work at arbitrary precision, and specifying Digits higher than the above value will give more accuracy, but will run much more slowly. In general, for the eigenfunction methods here, the accuracy is limited by the number of terms chosen in the series, and for most purposes hardware accuracy is sufficient.

```
> Digits := 10;
```

Now define the procedure *chsolve* for steady-state solution of a flow channel with no axial diffusion.
chsolve works in non-dimensionalized units. There are two modes:
1. The multisegment mode requires the specification of the boundary conditions at the *Y*=0 surface for successive downstream segments, such as electrode 1, gap, electrode 2, etc.
In this mode, the boundary conditions are specified as a piecewise function for the non-dimensionalized rate constant for the various segments, and a numerical value of the Peclet number has to be specified.
2. The single segment mode solves only a single segment (the electrode) of arbitrary length. This mode is detected by presenting only the value of the rate constant (possibly infinity) as the first parameter,
rather than a piecewise function. In this mode a name can be given for the Peclet number. This then allows plots as a function of the Peclet number to be generated easily.
Parameters:
1. *fK* is the non-dimensionalized rate constant. For multisegment calculation, it is given as a piecewise function of *X*, starting at the inlet, which can be at any value of *X*.
This specifies the boundary conditions at the electrode side (*Y*=0) of the channel. e.g., *X*->piecewise($0 \le X$ and $X < 2$, 10, $2 \le X$ and $X \le 3$,0, infinity) means *K*=10 at the electrode between *X*=0 and *X*=2,
K=0 (zero flux) between 2 and 3 (without an electrode), *K*=infinity (concentration zero) for $X \ge 3$ (last number is the "otherwise" value).
Be careful not to leave out a value, as in *X*<3, 27, *X*>3, 23 which makes the value at *X*=3 equal to the "otherwise" value, which defaults to zero.
If a simple number *K* is entered, only a single segment is calculated and this is the *K* value for X≥0, with the inlet assumed to be at *X*=0.
2. *f0* is a function specifying the initial concentration across the channel (*Y* direction) at the inlet, given as a function of the *Y*, running from 0 (electrode side) to 1 (top)
e.g., Y->1 for flat or Y->2*sin(Pi*Y) for a more interesting profile.
3. Nondimensionalized flow rate $A = 4v_{max}h/D$ where v_{max} is the velocity in the middle of the

channel, *h* is the channel height and *D* is the diffusivity. For multisegment calculations a number must be given,

but for single segment mode (if the rate *fK* is a number), a name such as *A* can be given, and this will be a variable in the output.

4. *N* is a positive integer specifying the number of terms to calculate in the eigenfunction expansion.

The output is a function (Maple procedure) that takes two arguments representing *X* and *Y* and gives the concentration as a (piecewise) function of *X* (distance along the electrode) and *Y* (distance away from electrode).

In single segment mode, the returned function is not in piecewise form.

A error message is given if the integrals could not be accurately numerically evaluated. In this case, increasing the setting of Digits may lead to success.

Note that although *X* and *Y* are used here to denote along and across the channel respectively, the arguments to *fK*, *f0* and the output function can be given any names.

To output a message at the beginning of every segment, set *infolevel*[*chsolve*] := 2 : before running the routine.

```
> chsolve := proc(fK, f0 :: procedure, A :: {numeric, symbol}, N :: posint)
    local b, X, Y, GY, G0, G1, G2, dG1, dG2, dG1at1, dG2at1, den, g1, g2, NormInt,
    bapprox0, bapprox1, bapproxhalf, bK, a, bc, pwise, i, pwfn, Xstart, K, fin, CXY, n, oneseg,
    intmethod, st;
     oneseg := type(fK, extended_numeric);
    if type(A, symbol) and not oneseg then error "A must be a number for multisegments"
    end if;
     if oneseg then pwise := [0, 0, fK]
    elif type(fK, procedure) and op(0, fK(X)) = piecewise then pwise := convert(fK(X),
    'pwlist')
    else error "K must be a number, infinity, or a piecewise function"
     end if;
     st := time( );  # start time for CPU clock
     if Digits > floor(evalhf(Digits)) then intmethod :='_Gquad' else intmethod :=
    '_d01akc' end if;
    userinfo(2, chsolve, cat("Using integration method ", intmethod));
    # Solution for G(Y) with G'(1)=0 and G(1)=1
     G1 := Hypergeom([1/4-(1/16)*b], [1/2], (1/4)*b*(-1+2*Y)^2)*exp(-(1
    /2)*b*Y*(-1+Y));
     G2 := Hypergeom([3/4-(1/16)*b], [3/2], (1/4)*b*(-1+2*Y)^2)*(-1+2
    *Y)*exp(-(1/2)*b*Y*(-1+Y));
    dG1 := diff(G1, Y);
    dG1at1 := eval(dG1, Y=1);
    dG2 := map(simplify, collect(diff(G2, Y), Hypergeom));
    dG2at1 := eval(dG2, Y=1);
    den := eval(dG2at1*G1-dG1at1*G2, Y=1);
    g1 := dG2at1/den;
    g2 := -dG1at1/den;
    GY := convert(collect((g1*G1+g2*G2), exp), hypergeom);
    # Normalization integral
    NormInt := Int(Y*(1-Y)*simplify(GY^2, exp), Y=0..1,'method'=intmethod);
```

```
    # Various approximations to the b values
    bapprox0 := [seq(evalf(8*n), n=1..N)];
    bapprox1 := [seq(evalf((n-1)*8), n=1..N)];
    bapproxhalf := [seq(evalf((n-1/2)*8), n=1..N)];
    # now iterate over the piecewise regions. i=1 is up to the first specified X value - ignore it
     pwfn := NULL :    # start to assemble the piecewise function
     fin := f0;                # initial concentration profile
    for i from 2 to nops(pwise) by 2 do
        Xstart := pwise[i];
        K := pwise[i+1];
        userinfo(2, chsolve,
    sprintf("Evaluating segment %d with K = %a at CPU time %.3f s", i/2, K, time() - st))
    ;
        if i+2 > nops(pwise) then pwfn := pwfn, X >= Xstart else pwfn := pwfn, `and`(X
    >= Xstart, X <= pwise[i+2]) end if;
        # Generate the list of b values for this segment
        if K = infinity then
            G0 := eval(GY, Y=0);
            bK := [seq(fsolve(G0, b=bapprox1[n]..bapproxhalf[n]), n=1..N)]
        elif K = 0 then
            bK := [seq(fsolve(eval(diff(GY, Y), Y=0), b=bapprox1[n]
    ..bapproxhalf[n]), n=1..N)]
        elif K > 0 then
            bc := eval(diff(GY, Y), Y=0) - K*(eval(GY, Y=0));
            bK := [seq(fsolve(bc, b=bapprox1[n]..bapproxhalf[n]), n=1..N)]
        else bc := eval(diff(GY, Y), Y=0) - K*(eval(GY, Y=0));    # negative K
            bK := [seq(fsolve(bc, b=bapproxhalf[n]..bapprox0[n]), n=1..N)]
         end if;
        # Generate the list of a values for this segment
        a := map(evalf@unapply(Int(Y*(1-Y)*fin(Y)*GY, Y=0..1,'method'
    =intmethod)/NormInt, b), bK);
        # and now CXY, the concentration for this segement
        CXY := add(evalf(collect(exp(-(bK[n])^2*(X-Xstart)/A)*a[n]*eval(GY,
    b=bK[n]), exp)), n=1..N);
        if has(CXY, Int) then error "Not all integrals could be evaluated" end if;
        if i+2 <= nops(pwise) then fin := unapply(eval(CXY, X=pwise[i+2]), Y) end
    if;  # find profile for next segment
        pwfn := pwfn, CXY;
      end do;
      userinfo(2, chsolve, sprintf("Completing calculation at CPU time %.3f s", time()
     - st));
      if oneseg then
        unapply(CXY, X, Y);
      else
        unapply(piecewise(pwfn), X, Y);
      end if;
  end proc:
```

Set infolevel to 2 or higher to print out information messages.

```
> infolevel[chsolve] := 2 :
```

Concentration profile for an irreversible reaction

This generates Fig. 2.
Run chsolve in single segment mode with nondimensionalized forward rate constant K=10 (evaluating 40 terms), and A = 100.

```
> C := chsolve(10, Y ↦ 1, 100, 40) :
> plot3d(C(X, Y), X = 0 ..2, Y = 0 ..1, orientation = [ -50, 80 ], scaling = constrained, shading
      = zhue, thickness = 2, tickmarks = [ 6, 4, 3 ], labels = [ "X", "Y", "C" ] );
> unassign('C'); #clean up for later
```

Limiting current as a function of flow rate

Run chsolve in single segment mode with infinite rate constant (evaluating 40 terms). Leave A unspecified so that the current can be plotted as a function of A.

```
> A := 'A': #forget any previous value A may have had
  C := chsolve(infinity, Y -> 1, A, 40):
```

The current density is a function of electrode width W and A in the combination A/W. This is the same as the current for W=1 as a function of A.

```
> Ilim := int(eval(diff(C(X, Y), Y) = 0), X = 0 .. 1):
```

For comparison, the Levich result using the Leveque approximation is

```
> IlimLev := 3/4 * A^(1/3) * 3^(5/6) * GAMMA(2/3) / Pi;
```

$$IlimLev := \frac{3}{4}\,\frac{A^{(1/3)}\,3^{5/6}\,\Gamma\left(\frac{2}{3}\right)}{\pi}$$

Plot the limiting current vs $A^{\frac{1}{3}}$ by using a parametric plot with A as parameter. The blue curve is the Levich result using the Leveque approximation.

```
> p1 := plot([A^(1/3), Ilim, A = 0 .. 100], colour = red):
  p2 := plot([A^(1/3), IlimLev, A = 0 .. 100], colour = blue): display(p1, p2)
> unassign('p1','IlimLev','p2','Ilim','C');
```

A multisegment example

A = 100. Electrode between X=0 and X=1 with nondimensionalized rate constant K=10, then a gap (no-flux boundary condition, K=0) to X=3, then a second electrode at limiting current (K=infinity). Note that we do not need to define the end of the last segment - it goes to wherever we want to calculate it to.

```
> fK := x→piecewise(x ≥ 0 and x < 1, 10, x ≥ 1 and x ≤ 3, 0, infinity);
```

```
> C := chsolve(fK, Y ↦ 1, 100, 40) :
```

```
> plot3d(C(X, Y), X = 0..4, Y = 0..1, axes = boxed, orientation = [-90, 0], scaling
      = constrained, style = surfacecontour, shading = zhue, grid = [120, 30]);
```

Plot of the concentration along Y=0 as a function of X.

```
> plot(C(X, 0), X = 0..4);
```

Now plot the current density at Y=0 as a function of X. D[2](C) means differentiate C with respect to the second variable (here Y), and then (X,0) means evaluate it at Y=0 (and any X).

```
> plot(D[2](C)(X, 0), X = 0..4);
```

Integrate to find to total current at each of the two electrodes

```
> evalf(Int(D[2](C)(X, 0), X = 0..1)); evalf(Int(D[2](C)(X, 0), X = 3..4));
```

```
> unassign('C','fK');
```

Collection efficiency calculation

Collection efficiency calculation. Start with only reactant (nondimensionalized concentration denoted by C) in solution. Then limiting current production of product of concentration S at electrode 1, then a gap, then limiting current removal of S at electrode 2. Electrode 1 ends at $X1$, gap ends at $X2$ and electrode 2 ends at $X3$.

```
> A := 100.; X1 := 1; X2 := 2; X3 := 3; Terms := 40;
```

Start by calculating the concentration C for the first two segments, i.e., electrode 1 and the gap. Rate constant for segment 1 is infinity (concentration $C = 0$) and for segment 2 is zero (no-flux condition)

```
> fK := x→piecewise(x ≥ 0 and x ≤ X1, infinity, 0);
  C12 := chsolve(fK, Y ↦ 1, A, Terms) :
```

Plot the concentration for the first two segments

```
> plot3d(C12(X, Y), X = 0 ..X2, Y = 0 ..1, axes = boxed, orientation = [ -60, 80 ], scaling
      = constrained, style = surfacecontour, shading = zhue);
```

For equal diffusivities, the concentration S is just 1-C. Plot of concentration S for the first two segments is therefore

```
> p12 := plot3d(1 - C12(X, Y), X = 0 ..X2, Y = 0 ..1, axes = boxed, orientation = [ -60, 80 ],
      scaling = constrained, style = surfacecontour, shading = zhue) : display(p12);
```

For electrode 2 we will calculate the concentration S, not C, so we first calculate the concentration profile as a function of Y at the end of the second segment, so we can use it as the inlet profile for electrode 2.

Make a function for the concentration S at $X2$.

```
> f2 := Y→1 - C12(X2, Y);
```

A plot of $f2$ across the channel shows that for low flow rates (small A) the concentration may be non-zero at the top of the channel

```
> plot(f2(Y), Y = 0 ..1, S = 0 ..0.5);
```

Now calculate the limiting current removal of the species with concentration S at electrode 2.

```
> S3 := chsolve(x→piecewise(x ≥ X2, infinity), f2, A, Terms) :
```

For large A the above can be a slow calculation, which can be speeded up by "digitizing" f2, which otherwise contains a large number of hypergeometric function calls, called multiple times in evaluating the integrals. For example, fit the values of this function at 101 points to a degree 10 polynomial

```
> Npts := 100 : ptsx := Vector([seq(y/evalf(Npts), y = 0 ..Npts)]) : ptsy
      := Vector([seq(f2(y/Npts), y = 0 ..Npts)]) :

  poly := Statistics:-PolynomialFit(10, ptsx, ptsy, Y) :
  f2num := unapply(poly, Y);
```

This simpler function is indistinguishable from the original data when plotted.

```
> plot([f2(Y), f2num(Y)], Y = 0 ..1, S = 0 ..0.5);
```

Chsolve now evaluates faster, but it is now hard to show that the error will diminish as the number of terms increases.

```
> S3num := chsolve(x→piecewise(x ≥ X2, infinity), f2num, A, Terms) :
```

Returning to the original concentration S at the second electrode $S3$,

```
> p3 := plot3d(S3(X, Y), X = X2..X3, Y = 0..1, axes = boxed, orientation = [-60, 80], scaling
      = constrained, style = surfacecontour, shading = zhue) : display(p3);
```

Now we stitch the concentration *S* in the three segments together into a single piecewise function: between 0 and *X2* we have 1-*C12* and between *X2* and *X3* we have *S3*

```
> S := (X, Y) → simplify(piecewise(0 ≤ X and X ≤ X2, 1 − C12(X, Y), X > X2, S3(X, Y)),
      piecewise) :
```

So that now it is easy to plot the concentration *S* for all three segments.

```
> plot3d(S(X, Y), X = 0..X3, Y = 0..1, axes = boxed, orientation = [-90, 0], scaling
      = constrained, style = surfacecontour, shading = zhue);
```

Work out the current density at *Y*=0 as a function of position along the channel.

```
> J := -eval(diff(S(X, Y), Y), Y = 0) :
> plot(J, X = 0..X3);
```

Integrate the current density over the two electrodes and then find their ratio, which is the collection efficiency.

```
> I1 := evalf(int(J, X = 0..X1));
  I2 := evalf(int(J, X = X2..X3));
  N := -I2/I1;
```

For comparison, the collection efficiency assuming the Leveque approximation (to which ours should tend at large A) may be calculated as given in C.M.A Brett and A.M.C.F. Oliveira-Brett, Hydrodynamic Electrodes, in Comprehensive Chemical Kinetics, Eds. C.H. Bamford and R.G. Compton, Elsevier, Amsterdam, 1986, v 26, p. 355.

```
> α := X2/X1 − 1; β := X3/X1 − X2/X1;
```

$$\mathrm{F} := \theta \rightarrow \frac{3^{\frac{1}{2}}}{4\cdot\pi}\cdot\ln\left(\frac{\left(1+\theta^{\frac{1}{3}}\right)^{3}}{1+\theta}\right)+\frac{3}{2\cdot\pi}\cdot\arctan\left(\frac{2\cdot\theta^{\frac{1}{3}}-1}{3^{\frac{1}{2}}}\right)+\frac{1}{4};$$

$$N0 := 1-F\left(\frac{\alpha}{\beta}\right)+\beta^{\frac{2}{3}}\cdot\left(1-F(\alpha)\right)-\left(1+\alpha+\beta\right)^{\frac{2}{3}}\cdot\left(1-F\left(\frac{\alpha}{\beta}\cdot\left(1+\alpha+\beta\right)\right)\right);$$

```
> evalf(N0);
> unassign('A','X1','X2','X3','C12','f2','S3','S','I1','I2','J','N','Terms','N0','α','β','F','p12','p3','fK',
      'Npts','ptsx','ptsy','poly','S3num','f2num');
```

Steady-state current vs potential for a quasireversible reaction - no product initially

Start with only reactant (nondimensionalized concentration denoted by C) in solution. Reference rate constants and potentials to E^o (strictly to the formal potential). $K0$ = standard nondimensionalized rate constant. Let $e = F(E - E^o)/RT$

Illustrate the method at a single potential, and then later run it in a loop to generate the current vs potential curve.

```
> e := 1.; K0 := 1; β := 0.5; A := 100; Terms := 40;
```

```
> Kf := K0·exp((1 − β)·e); Kb := K0·exp(−β·e); K := Kf + Kb;
```

Start by calculating the concentration profile for the irreversible case, but with rate constant $K = Kf + Kb$

```
> Cir := chsolve(K, Y ↦ 1, A, Terms) :
```

The quasireversible concentration may be found by the rule:

```
> CQ := (X, Y) → (Cir(X, Y)·Kf + Kb)/K;
```

The product concentration is 1-CQ. Check that the electrode boundary condition holds by plotting the flux and the rate expression, which should be equal. The two plots are on top of each other.

```
> plot([eval(∂/∂Y CQ(X, Y), Y = 0), Kf·CQ(X, 0) − Kb·(1 − CQ(X, 0))], X = 0..0.2);
```

Plot the two concentration profiles together.

```
> plot3d([CQ(X, Y), 1 − CQ(X, Y)], X = 0..2, Y = 0..1, orientation = [−50, 80], view
      = [DEFAULT, DEFAULT, 0..1], scaling = constrained, style = surfacecontour, shading
      = zhue, thickness = 2, tickmarks = [6, 4, 3], labels = ["X", "Y", "C, S"]);
```

Now put it in a loop to calculate the steady-state current potential curve. Choose electrode width W= 1 to integrate over to get the total current. ei and ef are the initial and final potentials (units of RT/F) and de is the potential increment. Choose the parameters

```
> K0 := 10.; β := 0.5; A := 100.; Terms := 40; W := 1.;
  ei := −4.; ef := 8.; de := 1;
```

And loop around. Setting infolevel[chsolve] to 1 suppresses information messages from chsolve. forget(hypergeom) clears out memory used for remembering the results of hypergeom calls in case they are repeated.

```
> infolevel[chsolve] := 1 :
  IQ := NULL : E := NULL :
  for e from ei to ef by de do
    print(e);
    Kf := K0·exp((1 − β)·e); Kb := K0·exp(−β·e); K := Kf + Kb;
    Cir := chsolve(K, Y ↦ 1, A, Terms);
    CQ := (X, Y) → (Cir(X, Y)·Kf + Kb)/K;
    IQ := IQ, evalf(int(eval(diff(CQ(X, Y), Y), Y = 0), X = 0 .. W));
    E := E, e;
    forget(hypergeom);
  end do:
  E := [E] : IQ := [IQ] :
```

```
infolevel[chsolve] := 2 :

plot(E, IQ, style=point);
unassign('E','IQ','e','ei','ef','de','β','W','A','K0','Kf','Kb','K','Cir','CQ','Terms');
```

Steady-state current vs potential for a quasireversible reaction - with product initially

Let $C = c/(c^b + s^b)$ and $S = s/(c^b + s^b)$, where c^b and s^b are bulk concentrations. Let $f=c^b/(c^b + s^b)$ be the fraction of the initial concentration that is reactant. Keq=exp(F($Erev$-$E0$)/RT))=s^b/c^b (Nernst equation) . Let $E=\eta F/RT$. Let veq be the exchange rate,
so $veq = kfeq*c^b=kbeq*s^b$ or $V'eq=Kfeq*c^b=Kbeq*s^b$ or $Veq=V'eq/(c^b + s^b)=Kfeq*f=Kbeq*(1-f)$

```
> A := 100.; E := -3.; f := 0.6; Veq := 1; β := 0.5; Terms := 40;
```

```
> Keq := (1 - f)/f; Kfeq := Veq/f; Kf := Kfeq·exp((1 - β)·E); Kbeq := Veq/(1 - f); Kb := Kbeq
      ·exp(-β·E); K := Kf + Kb;
```

Solve with the irreversible Robin boundary condition with $K = Kf + Kb$

```
> Cir := chsolve(K, Y ↦ 1, A, Terms) :
```

The irreversible concentration can be converted to the quasireversible concentration by the following rule.

```
> CQ := (X, Y) → (Cir(X, Y)·(f·Kf - (1 - f)·Kb) + Kb)/K;
```

The product concentration is $SQ = 1 - CQ$. The quasireversible current density calculated from the flux should agree with that from the rate expression.

```
> plot([eval(∂/∂Y CQ(X, Y), Y = 0), Kf·CQ(X, 0) - Kb·(1 - CQ(X, 0))], X = 0 .. 1);
```

Plot the reactant and product concentrations

```
> plot3d([CQ(X, Y), 1 - CQ(X, Y)], X = 0 .. 2, Y = 0 .. 1, orientation = [-50, 80], view
      = [DEFAULT, DEFAULT, 0 .. 1], scaling = constrained, style = surfacecontour, shading
      = zhue, thickness = 2, font = [Times, normal, 10], tickmarks = [6, 4, 3], labels = ["X",
      "Y", "C,S"]);
```

Now work out the steady-state current potential curve. Choose parameters on the next line.

```
> Veq := 1; f := 0.6; β := 0.5; A := 100; W := 1; Terms := 40;
  ei := -6; ef := 6; de := 1;
```

And loop around. Setting infolevel[chsolve] to 1 suppresses information messages from chsolve. forget(hypergeom) clears out memory used for remembering the results of hypergeom calls in case they are repeated.

```
> infolevel[chsolve] := 1 :
  Keq := (1 - f)/f; Kfeq := Veq/f; Kbeq := Veq/(1 - f);
  IQ := NULL : E := NULL :
  for e from ei to ef by de do
    print(e);
    Kf := Kfeq·exp((1 - β)·e); Kb := Kbeq·exp(-β·e); K := Kf + Kb;
    Cir := chsolve(K, Y ↦ 1, A, Terms);
    CQ := (X, Y) → (Cir(X, Y)·(f·Kf - (1 - f)·Kb) + Kb)/K;
    IQ := IQ, evalf(int(eval(diff(CQ(X, Y), Y), Y = 0), X = 0 .. W));
    E := E, e;
```

```
    forget(hypergeom);
  end do:
  E := [E] : IQ := [IQ] :
  infolevel[chsolve] := 2 :

> plot(E, IQ, style=point);
> unassign('Keq','Kb','f','A','Cir','E','Kbeq','ef','CQ','W','Kf','Veq','IQ','K','Terms','beta','Kfeq','ei',
      'de');
```

B Comsol documentation for Chapter 6

B.1 Introduction to the numerical solutions

This appendix consists of three Comsol documentation files that are used as part of the work for Chapter 6. The different parts used here are similar in many respects and the appendix aims to present the reader with the most condensed summary of the calculations making it possible to duplicate the models using only the appendix. The relevant calculations are used to find the results shown in 8.3. All solutions were obtained using COMSOL Multiphysics 5.0 [59], and the module used was the Batteries & Fuel Cells Module.

B.1.1 Input parameters

The input parameters are given in Table B.1. In addition, one more parameter is determined, based on the input when running a parametric run in Comsol, this variable is the inlet velocity of the flow, and is defined in Eq. (B.1).

$$V_0 = AD_{\mathrm{y}}/(6Ch_{\mathrm{h}}) \tag{B.1}$$

B.1.2 Geometry

The geometry made has been described earlier in Chapter 6.2. When the geometry was built in Comsol, non-dimensionalization of the problem was done by choosing values for the geometry and physical parameters that was 1 unit. The geometry was then built using the geometry values in Table B.1. The full geometry is shown in Fig. B.1.

To explain where the boundary conditions are set and where the solution is calculated, the boundaries and domains are numbered and this is shown in Fig. B.2 and Fig. B.3. All values are in m for the geometry, and the numbering introduced in the figures are used to describe the setup further.

B.1.3 Material

The material selected for the flow channel is a propertyless material, as no properties are actually needed for the calculations done here. The flow is already assumed to be fully developed, and stated as such.

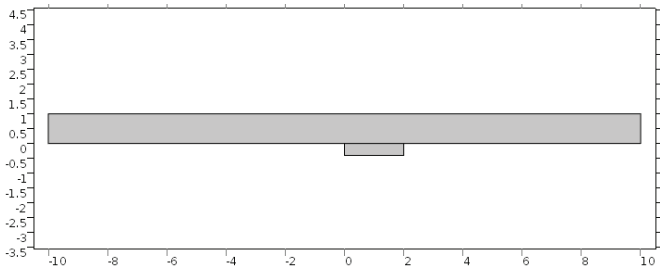

Figure B.1: The geometry built in Comsol, using unity of SI units as the parameters. The working electrode has a width shown in the lower side of the channel, but it has no calculations done on it.

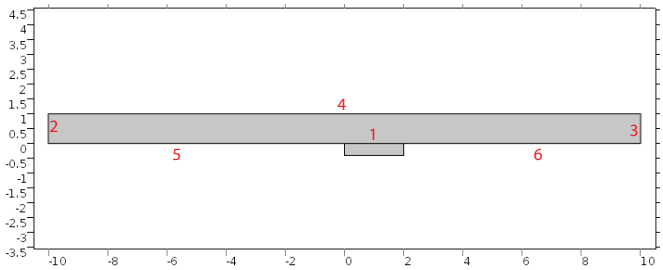

Figure B.2: Figure showing the geometry used including the numbering of the boundaries. These are used to set the boundary conditions, including (1) electrode, (2) inlet, (3) outlet, and (4) to (6) walls.

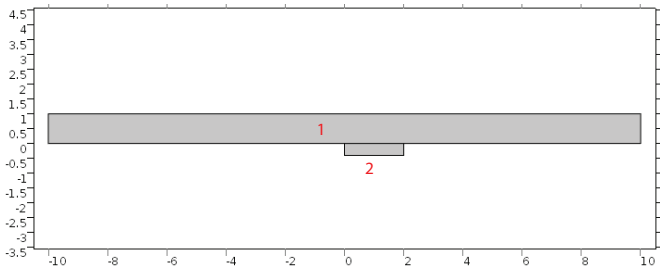

Figure B.3: Figure showing the geometry used including the numbering of the domains. Domain (1) is the channel where all the calculations are done, while (2) is the electrode.

Table B.1: The input parameters used for all Comsol calculations for this section

Name	Expression	Description
D_{y}	1 [m^2 s^{-1}]	Diffusion coefficient, y-direction
D_{x}	0 [m^2 s^{-1}]	Diffusion coefficient, x-direction
C_0	1 [mol m^{-3}]	Initial concentration (of species R)
K	10^{10} [m s^{-1}]	Rate constant
E_{w}	$2Ch_h$ [m]	Electrode width
Ch_{w}	$20Ch_h$ [m]	Channel width
Ch_{h}	1 [m]	Channel height
Ch_{d}	1 [m]	Channel depth
$Pe_{\max}$	10^5	Maximum Péclet number for diffusion layer thickness calcul
$x_{\mathrm{diff,min}}$	$(\frac{1}{0.925})(\frac{Pe_{\max}}{3})^{-1/3}$ []	Maximum Levich diffusion layer thickness
n	1 []	Chemical constant, number of electrons per atom reacted
R_{const}	8.3144621 [J mol^{-1} K^{-1}]	Gas constant
T_{const}	298.15 [K]	Temperature
F_{const}	96485.3365 [C mol^{-1}]	Faraday constant
A	1 []	Péclet number
$C1$	38.9221 []	Correction to get KC kinetics, used at electrode reaction

B.1.4 Physics

The physics chosen is the electroanalysis module under the Battery and Fuel Cells Module in the Comsol framework. This allows for a solution involving the full convective-diffusion equation. We chose to not look at current flow in the electrolyte, as this is assumed negligible in our work.

The physics is chosen to matter for only domain 1, and the governing equations that are solved are the following equations.

$$\nabla \cdot (-D_i \nabla c_i) + \mathbf{u} \cdot \nabla c_i = R_i \tag{B.2}$$

$$\mathbf{N}_i = -D_i \nabla c_i + \mathbf{u} c_i \tag{B.3}$$

$$\phi_l = 0 \tag{B.4}$$

The parameters introduced here include R_i, the reaction happening in solution ($= 0$), and ϕ_l, the potential in the solution ($= 0$).

Convection is turned on in the setting, and the diffusion coefficients are set to $D_{x,i}$ = D_x = 0 and $D_{y,i}$ = D_y = 1 m^2 s^{-1}, meaning that as we are solving the problem assuming no axial diffusion, the axial diffusion is set to zero.

Convection is set in domain 1, and the Poiseuille flow is stated fully developed, i.e. as in the Equation below.

$$V_x = 6V_0 y \frac{(Ch_{\mathrm{h}} - y)}{Ch_{\mathrm{h}}^2} \tag{B.5}$$

The boundary conditions are set at the boundaries, and the first one is the no flux (wall) boundary conditions. This is set on boundaries (4)-(6), and is stated below.

$$-\mathbf{n}\cdot\mathbf{N}_i = 0 \tag{B.6}$$

Inflow is set at boundary (2) and the equation governing this is stated below. This is simply a Dirichlet boundary condition stating the concentration at the inlet.

$$c_i = c_{0i} \tag{B.7}$$

At the outlet at boundary (3), a Neumann boundary condition is stated, where the concentration flux is set as zero. This is stated below.

$$-\mathbf{n}\cdot D_i\nabla c_i = 0 \tag{B.8}$$

The boundary conditions stated so far, the wall, inlet, and outlet are all standard boundary conditions where the equations are not chosen, but set by the type of boundary chosen.

The last boundary condition is at the electrode, boundary (1). At this boundary, several equations are valid, starting with the total equations first.

$$i_{\text{total}} = \sum_m i_{\text{loc},m} \tag{B.9}$$

$$-\mathbf{n}\cdot\mathbf{N}_i = R_{i,\text{tot}} \tag{B.10}$$

$$R_{i,\text{tot}} = \sum_m R_{i,m} \tag{B.11}$$

At the electrode, the only thing allowed to happen is the electrode reaction, and this is defined as an anodic Tafel equation, run at an overpotential defined as below.

$$\eta = \phi_{s,\text{ext}} - \phi_l - E_{\text{eq}} \tag{B.12}$$

The Tafel equation has a slope of 118 mV, and has the equation given below.

$$i_{i,\text{loc}} = KF_{\text{const}}c_{\text{Red}}10^{\eta/118} \tag{B.13}$$

This is run at an overpotential set at the electrode of 0.1 V. This setting ensures that the reaction is run either at a limiting current ($c_i = 0$) or that the correct kinetics is set.

B.1.5 Mesh

The mesh has in total 481650 quadrilateral elements, with 3950 Edge elements. This is a mesh set in x and y direction so that no axial diffusion is introduced.

The mesh is made by first making the edge and then mapping the whole volume. This is set so that at the boundaries on the electrode and the sides, the variables in Table B.2. This is grown out of the two electrode edge points and the corner points at the inlet and outlet at the $y = 0$ point.

The mesh is then mapped in Domain 1, and it is shown in Fig. B.4.

Table B.2: The meshing parameters used to make the mapped mesh used in this section

Description	Value
Maximum element size	$0.002x_{\mathrm{diff,min}}$
Minimum element size	$0.002x_{\mathrm{diff,min}}$
Curvature factor	0.3
Maximum element growth rate	1.02
Custom element size	Custom

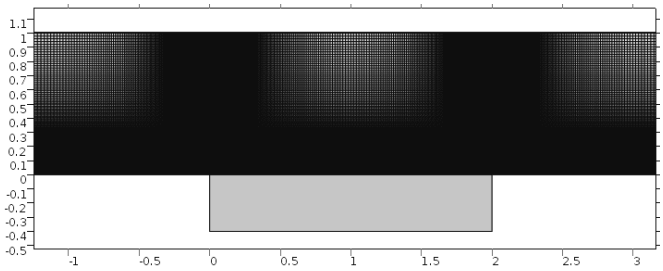

Figure B.4: Figure showing the mesh used focusing on the electrode surface.

B.1.6 Solver

The problem is solved in the given geometry (domain (1)) and using the physics stated. A stationary solver is used and two variables are solved for c_{Ox} and c_{Red}. The tolerance was set to 0.000001 and a direct solver was used with an initial damping of 0.01, a minimum damping of 10^{-6}, and a maximum number of iterations of 100. The solver used was the PARDISO solver.

B.2 Calculation of the dimensionless current at an example

Below is the description of the Comsol file for the calculation of the dimensionless current at the irreversible case in Section 6.4.1. For this case the K value was set to 10, to get the KC reaction kinetics. This was solved for one parameter, namely flow of an A value of 100. The initial value was set as 1 mol m^{-3} only for the reaction component and the reaction was run so that no oxidized product was made (i.e. unphysical reaction).

The results is shown as a concentration distribution of the reacting component, and is shown in Fig. B.5. This result is the basis for the calculation of the total current (dimensionless) as 2.1718.

B.3 Calculation of the collection efficiency

Below is the description of the Comsol file for the calculation of collection efficiency for the setup given in Section 6.4.4. This solution demands two separate electrodes, one

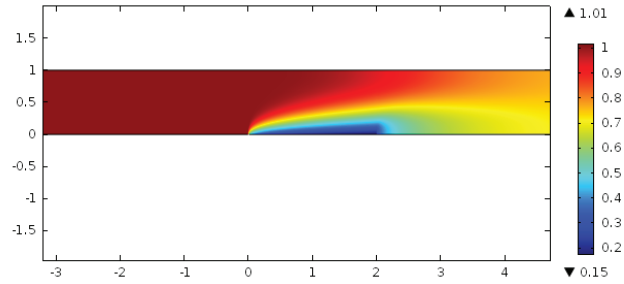

Figure B.5: Figure showing the resulting concentration for the irreversible reaction case.

where the reactant is oxidized and one where the product is reduced back to the reactant. These both have the width of $E_{\mathrm{w}} = 1$ m, and one electrode width between them. The geometry used is shown in Fig. B.6.

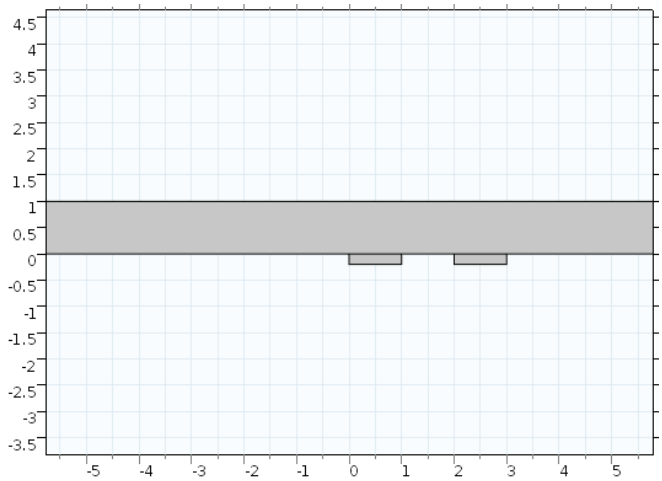

Figure B.6: Figure showing the geometry for the calculation of the collection efficiency.

B.3.1 Physics

For this case, the reaction at the upstream electrode features a production of oxidized species, while the reaction at the downstream electrode features production of reduced species. These are run at limiting current at both electrodes with opposite directions. So at the upstream electrode, the reaction is given below.

$$i_{\mathrm{loc}} = KF_{\mathrm{const}} c_{\mathrm{Red}} \exp(\eta/118)/C1 \tag{B.14}$$

The division by C1, is done to strictly get the correct value of the K value. There is a very large driving force for the reaction here, so the concentration at the electrode is zero for the reacting species. At the downstream electrode, the current is opposite due to

the opposite reaction occurring resulting in a negative current. The reaction equation is given below.

$$i_{\mathrm{loc}} = KF_{\mathrm{const}} c_{\mathrm{Ox}} \exp(\eta/(-118))/C1 \tag{B.15}$$

Now, the overpotential at the upstream electrode is 0.1 V, and the overpotential at the downstream electrode is -0.1 V, so the current gets very high if the concentration allows it, and efficiently gives a limiting current at both electrodes.

B.3.2 Mesh

The mesh in this case was refined to get as high resolution as possible with the used memory limitations (8 Gb). The meshing data is given in Table B.3, and this was done at all four electrode corners along with the down left corner at the inlet. The mapping was done from these points giving a high resolution.

Table B.3: The meshing parameters used to make the mapped mesh used in this section

Description	Value
Maximum element size	$0.001x_{\mathrm{diff,min}}$
Minimum element size	$0.001x_{\mathrm{diff,min}}$
Curvature factor	0.3
Maximum element growth rate	1.02
Custom element size	Custom

B.3.3 Result

The result was calculated by integrating the current (dimensionless) over the upstream and downstream electrode. These resulted in the values of 3.3153 at the upstream electrode and -1.0391 at the downstream electrode. Both these values are calculated at a A value of 100, and the resulting collection efficiency was 0.2956.

The concentration distribution for the reaction species is shown in Fig. B.7.

B.4 Calculation of the dimensionless current for several A values

Below is the description of the Comsol file for the calculation of numerous A values used in Fig. 6.3 and in Section 6.4.2. This result demands a lot of calculations for different A values and is best summarized by the figure in the paper (Fig. 6.3). This calculation takes several hours to execute. The geometry used for this case is a simple one electrode procedure where the value we look for is the dimensionless current at the electrode in order to compare this value to literature values using other approaches. The geometry is shown in Fig. B.8.

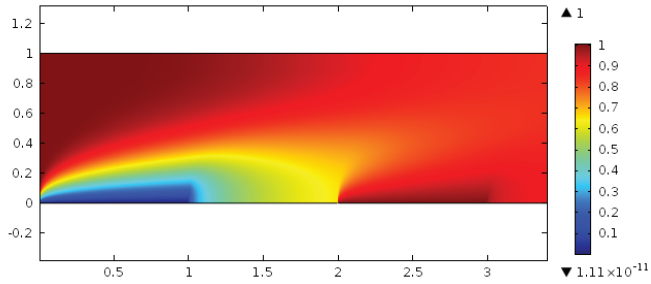

Figure B.7: Figure showing the concentration distribution of the reacting species for the collection efficiency case.

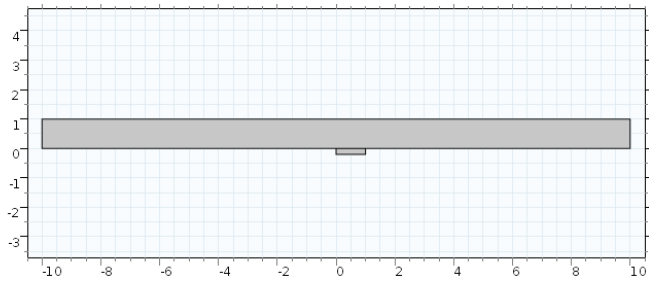

Figure B.8: Figure showing the one-electrode geometry used for finding the dimensionless current at different A values.

The mesh used for this case is the same as for the first case, the current at a irreversible kinetics and the parameters are shown in Table B.2.

B.4.1 Physics

For this case, the kinetics is set so that the current is diffusion limited, so the K value is high and the overpotential is high (1 V). This gives a very high driving force for the reaction and effectively a surface concentration of zero of the reacting species.

B.4.2 Results

The results are best summarized in Fig. 6.3. Table B.4 shows the numeric dimensionless currents used to create this figure.

Table B.4: A selection of A values and the resulting dimensionless currents.

A	$A^{1/3}$	Dimensionless current
0.10000	0.46416	0.016448
0.31623	0.68129	0.052437
1.000	1.0000	0.16645
3.1623	1.4678	0.52231
10	2.1544	1.3194
31.623	3.1623	2.2906
100	4.6416	3.5154
316.23	6.8129	5.2817
20	2.7144	1.8933
40	3.42	2.5085
60	3.9149	2.9192
80	4.3089	3.2431
120	4.9324	3.7529
140	5.3133	3.9649
160	5.4288	4.1574
180	5.6462	4.3342
200	5.848	4.4983

C Comsol documentation for Chapter 7

C.1 Introduction to the numerical solutions

This appendix consists of three Comsol documentation files that are used in the preparation of the work for Chapter 7. The appendix aims to present the reader with the most condensed summary of the calculations making it possible to duplicate the calculations using only the appendix. This appendix is separated in two sections where section C.2 summarizes the Comsol calculations comparing experimental data and using the real geometry and kinetic parameters, i.e. Fig. 7.4 and Fig. 7.6. The second section, Sec. C.4, summarizes the work done for Fig. 7.7 where a pure modeling framework was used and all dimensions are dimensionless in the framework of Comsol, i.e. that all units are 1 SI unit. The solution where all obtained in Comsol 5.0, and the used module was the Batteries & Fuel Cells Module.

C.2 Fig. 7.4, full unit solutions

C.2.1 Input parameters

The input parameters are given in Table C.1. The values used for Fig. 7.4 are given in the first column, and all parameters that are different for Fig. 7.6 are given in the second column.

C.2.2 Geometry

The geometry is built based on the input parameters. The electrode was made as wide as E_{w} and as high as $E_{\mathrm{w}}/5$. This was placed so that the upper left corner was at coordinates (0,0). The electrolyte volume was Ch_{w} wide and Ch_{h} high. This was placed so that the midpoint of the channel was at the electrode start, i.e. coordinates (0,0). The geometry build in such a way is given in Fig. C.1.

C.2.3 Materials

The materials set for this calculations are not central to the actual calculations. This is because the parameters that influence the result, i.e. concentrations and diffusion coefficients are set independent of the material in the solution. Therefore, the preset water

Table C.1: The input parameters used for all Comsol calculations in this section.

Name	Expression	Description
D_{Ru2}	8.8×10^{-10} [m^2 s^{-1}]	Diffusion coefficient of species 1
D_{Ru3}	5.71×10^{-10} [m^2 s^{-1}]	Diffusion coefficient of species 2
C_{Ru20}	4 [mol m^{-3}]	Initial concentration of species 1
C_{Ru30}	4 [mol m^{-3}]	Initial concentration of species 2
K	10^{10} [m s^{-1}]	Rate constant
k_0	$10^{10}/96485.3365$ [m s^{-1}]	Rate constant
E_{w}	Ch_{h} [m]	Electrode width
Ch_{w}	$20Ch_{\mathrm{h}}$ [m]	Channel width
Ch_{h}	100×10^{-6} [m]	Channel height
Ch_{d}	1 [mm]	Channel depth
n	1 []	Chemical constant, number of electrons per atom reacted
R_{const}	8.3144621 [J mol^{-1} K^{-1}]	Gas constant
T_{const}	294 [K]	Temperature
F_{const}	96485.3365 [C mol^{-1}]	Faraday constant
V_{app}	5 [mV]	Electrode potential perturbation
f_{max}	10000 [Hz]	Maximum frequency
$x_{\mathrm{diff,min}}$	$\sqrt{D_{\mathrm{Ru2}}/(\pi f_{\mathrm{max}})}$	Maximum diffusion length
A	1 []	Péclet number
B	1 []	Mixed dimensionless number ($E_{\mathrm{w}}/Ch_{\mathrm{h}}$)

material in the database was used for the electrolyte volume. The electrolyte volume that was set as water is marked as blue in Fig. C.2.

C.2.4 Physics setup

The physics in Comsol is setup so that a general equation to be solved in the area where the physics is set. In addition, each border of this area needs to have a boundary condition set. The boundary conditions set for this calculation are summarized in Fig. C.2 where each boundary is numbered from 1 to 6, and the area where the physics is valid is marked blue. This is the same area where water is set as the material.

The general equations solved in the volume (blue in Fig. C.2) are given in Eq. (C.1)-(C.3).

$$\nabla \cdot (-D_i \nabla c_i) + \mathbf{u} \cdot \nabla c_i = R_i \tag{C.1}$$

$$\mathbf{N}_i = -D_i \nabla c_i + \mathbf{u} c_i \tag{C.2}$$

$$\phi_l = 0 \tag{C.3}$$

Here, D_i is the diffusion coefficient of species i, c_i is the diffusion coefficient of species i, $\boldsymbol{u}$ is the convection, R_i is the total reactions happening in the volume (=1), N_i is the normal flux, and ϕ_l is the electrolyte potential.

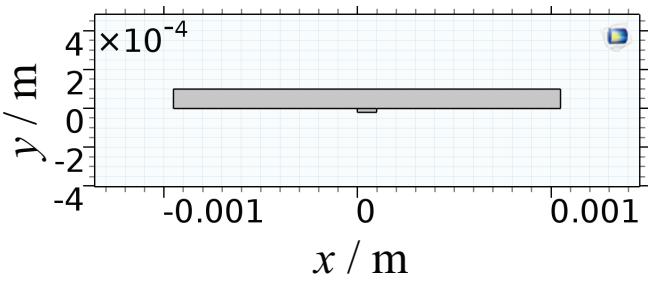

Figure C.1: The geometry built in Comsol for Fig. 7.4.

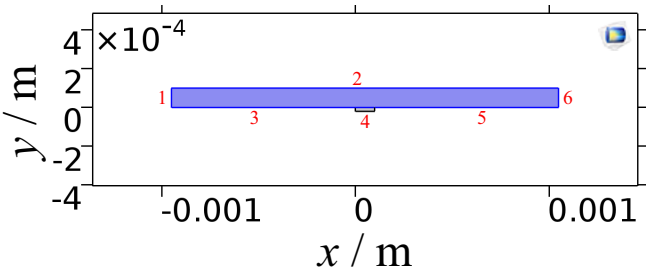

Figure C.2: The physics set to solve in in Comsol for Fig. 7.4. The numbers mark the boundaries, and the set conditions being inlet (1), outlet (6), walls (2,3 and 5), and the electrode (4).

Convection is turned on in the setting, and set to be valid in domain 1 as the where the physics is set. The convection is not calculated but stated as Poiseuille flow and given as in Eq. (C.4).

$$V_x = 6V_0 y(Ch_\mathrm{h} - y)/Ch_\mathrm{h}^2 \tag{C.4}$$

The boundary conditions are set at the boundaries, and the first one is the no flux (wall) boundary conditions. This is set on boundaries 2,3 and 5 as in Fig. C.2. The equation giving the no flux is given in Eq. (C.5). The n here is the normal parameter, i.e. that the flux normal to the wall is zero.

$$-\mathbf{n}\cdot\mathbf{N}_i = 0 \tag{C.5}$$

Inflow is set at boundary 1 in Fig. C.2 and the equation governing this is stated below in Eq. (C.6). This is simply a Dirichlet boundary condition stating the concentration at the inlet, and the concentrations used are C_{Ru20} and C_{Ru30} as given in Table C.1.

$$c_i = c_{0i} \tag{C.6}$$

At the outlet at boundary 6 in Fig. C.2, a Neumann boundary condition is stated, where the diffusion flux is set as zero meaning that only convection contributes to mass transport over this boundary. This is stated below in Eq. (C.7).

$$-\mathbf{n}\cdot D_i\nabla c_i = 0 \tag{C.7}$$

The boundary conditions stated so far, the wall, inlet, and outlet are all standard boundary conditions where the equations are not chosen, but set by the type of boundary chosen.

The last boundary condition is at the electrode, boundary 4 in Fig. C.1. This is where all reactions occur in the system influencing the concentration distribution calculated. At this boundary, several equations are valid, starting with the total equations given in Eq. (C.8)-(C.8).

$$i_\mathrm{total} = \sum_m i_{\mathrm{loc},m} \tag{C.8}$$

$$-\mathbf{n}\cdot\mathbf{N}_i = R_{i,\mathrm{tot}} \tag{C.9}$$

$$R_{i,\mathrm{tot}} = \sum_m R_{i,m} \tag{C.10}$$

Here, i_total is the total current, $i_{\mathrm{loc},m}$ is the local current for each reaction, $R_{i,\mathrm{tot}}$ is the total reaction flux occurring at the electrode, and $R_{i,m}$ is the reaction of step m.

At the electrode, the only thing allowed to happen is the electrode reaction, and this is defined as an anodic Tafel equation, run at an overpotential defined as below in Eq. (C.11).

$$\eta = \phi_{s,\text{ext}} - \phi_l - E_{\text{eq}} \tag{C.11}$$

Here, η is the overpotential, ϕ_s is the electrode potential, and E_{eq} is the equilibrium potential set to 0 V in our case.

The electrode reaction is then set as a Butler-Volmer equation as given in Eq. (C.12)

$$i_{i,\text{loc}} = nFk_0\Big(C_{\text{Ru2}}\exp(\frac{(n-\alpha_c)F\eta}{RT}) - C_{\text{Ru3}}\exp(\frac{-\alpha_c F\eta}{RT})\Big) \tag{C.12}$$

This equation gives a reversible reaction since the reaction constant, k_0, is very large as given in Table C.1. This is then modeled using a fluctuation potential, ϕ_s, with an amplitude of V_{app}.

C.2.5 Mesh

The mesh was a free triangle mesh with in total 806 016 triangular elements and 8644 edge elements. The values in Table C.2 where used to set the meshing parameters, where the values in column "Value, edge" are used for meshing the electrode surface, boundary 4 in Fig. C.2. The values in column "Value, volume" are used for the rest of the electrolyte volume.

Table C.2: The meshing parameters used to make the mapped mesh used in this section

Description	**Value, edge**	**Value, volume**
Maximum element size	$0.1x_{\text{diff,min}}$	$10x_{\text{diff,min}}$
Minimum element size	$0.1x_{\text{diff,min}}$	$0.1x_{\text{diff,min}}$
Curvature factor	0.3	0.3
Maximum element growth rate	1.03	1.05
Custom element size	Custom	Custom

The resulting mesh is shown in Fig. C.3 for the whole volume and in Fig. C.4 for a focus on the mesh at the electrode surface.

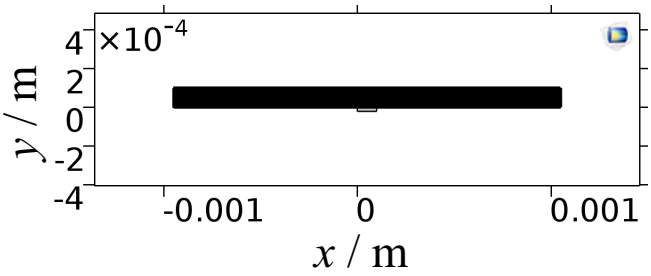

Figure C.3: The mesh for the whole volume built in Comsol.

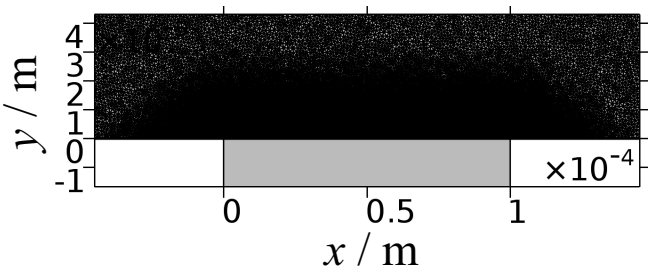

Figure C.4: Focus on the mesh at the electrode surface used in this section.

C.2.6 Solver

The problem is solved by doing a parametric study for the flow rates relevant in our case, i.e. from 10 μL min^{-1} to 300 μL min^{-1}, and for a wide range of frequencies from 10^{-3} Hz to 10^5 Hz. This was solved in a sequence where first the steady-state solution was done, and then the frequency was applied on top of this steady-state solution giving the individual frequency solutions. The solver is used in the volume that is marked blue in Fig. C.2.

The steady-state solution was found using a stationary solver solving for the variable C_{Ru2} and $\mathrm{C}_{\mathrm{Ru3}}$. A fully coupled direct solver was used and the initial damping factor was set to 0.01, the maximum damping factor was set to 10^{-6}, and the maximum number of iterations was set to 50. The PARDISO solver was used for this problem. The same type of solver and parameters was used for the frequency dependent problem, and the complex numbers were treated directly as such.

C.2.7 Results

The resulting impedance for each flow rate is found from an integration procedure for each frequency. This is done from the relation between the concentration at the electrode surface and the concentration gradient at the electrode surface. The equation that is integrated over the surface is given in Eq. (C.13).

$$Z_i = \frac{C_i(0)}{\frac{dC_i}{dy}|_{y=0} C h_{\mathrm{h}}} \tag{C.13}$$

To find the equivalent measured impedance, the impedance for each species are combined using Eq. (7.4). Subsequently, the calculated impedance values can be compared to the numerical impedance values.

C.3 Fig. 7.6, full unit solution

The treatment done to get the solution in Fig. 7.6 is very similar to the setup described above. Therefore, only the differences are summarized.

The main difference is that the geometry of the electrode and channel are different, and the input parameters used are given in Table C.3. The parameters different for the calculation in the previous section are marked as bold.

Table C.3: The input parameters used for all Comsol calculations in this section.

Name	Expression	Description
D_{Ru2}	2.3×10^{-9} [m^2 s^{-1}]	Diffusion coefficient of species 1
D_{Ru3}	2.3×10^{-9} [m^2 s^{-1}]	Diffusion coefficient of species 2
C_{Ru20}	1.01 [mol m^{-3}]	Initial concentration of species 1
C_{Ru30}	0 [mol m^{-3}]	Initial concentration of species 2
K	10^{10} [m s^{-1}]	Rate constant
k_0	$10^{10}/96485.3365$ [m s^{-1}]	Rate constant
E_{w}	6.5×10^{-6} [m]	Electrode width
Ch_{w}	$50Ch_{\mathrm{h}}$ [m]	Channel width
Ch_{h}	0.4 [mm]	Channel height
Ch_{d}	6 [mm]	Channel depth
n	1 []	Chemical constant, number of electrons per atom reacted
R_{const}	8.3144621 [J mol^{-1} K^{-1}]	Gas constant
T_{const}	298,15 [K]	Temperature
F_{const}	96485.3365 [C mol^{-1}]	Faraday constant
V_{app}	5 [mV]	Elecrode potential perturbation
f_{max}	10000 [Hz]	Maximum frequency
$x_{\mathrm{diff,min}}$	$\sqrt{D_{\mathrm{Ru2}}/(\pi f_{\mathrm{max}})}$	Maximum diffusion length
A	1 []	Péclet number
B	1 []	Mixed dimensionless number ($E_{\mathrm{w}}/Ch_{\mathrm{h}}$)

This changes a few parameters, so that the mesh was slightly refined to solve with the highest accuracy available. Therefore, the meshing data was as given in Table C.4. The mesh consisted of 115 680 triangular elements and 2256 edge elements and was meshed in a similar fashion as in the previous section.

Table C.4: The meshing parameters used to make the mapped mesh used in this section

Description	Value, edge	Value, volume
Maximum element size	$0.05x_{\mathrm{diff,min}}$	$100x_{\mathrm{diff,min}}$
Minimum element size	$0.05x_{\mathrm{diff,min}}$	$0.05x_{\mathrm{diff,min}}$
Curvature factor	0.3	0.25
Maximum element growth rate	1.03	1.05
Custom element size	Custom	Custom

Finally, the last difference is that for the Fig. 7.6, a flow rate of 2.9e-3 cm^3 s^{-1} was used and a frequency range from 10^{-3} to 10^4 was used for the solution. All other aspects of the solution were similar and the impedance was found in the same way.

C.4 Fig. 7.7, dimensionless solution

The solution used here was dimensionless on purpose and the parameters A and B was used to investigate the validity and usefulness of the analytical solutions previously derived in literature. The change in the B parameter, i.e. the relation between the electrode width, El_{w}, and the channel height, Ch_{h}, introduces some complications to the solving method. Most importantly, a meshing criteria might not be valid at all electrode widths and subsequently, the meshing criteria was stricter if the electrode was smaller. This also matters as a very fine mesh will use too much RAM when solving it numerically, and hence, a trade-off is necessary. Starting again with the input parameters, we will go through all the steps for making this solution as well.

C.4.1 Input parameters

The input parameters used are given in Table C.5. The geometric and diffusive parameters are given as 1 SI unit. This is the solution chosen for this problem to get a dimensionless solution in the end.

Table C.5: The input parameters used for all Comsol calculations in this section.

Name	Expression	Description
D_{Ru2}	1 [m^2 s^{-1}]	Diffusion coefficient of species 1
D_{Ru3}	1 [m^2 s^{-1}]	Diffusion coefficient of species 2
C_{Ru20}	1 [mol m^{-3}]	Initial concentration of species 1
C_{Ru30}	1 [mol m^{-3}]	Initial concentration of species 2
K	10^{10} [m s^{-1}]	Rate constant
k_0	$10^{10}/96485.3365$ [m s^{-1}]	Rate constant
E_{w}	BCh_{h} [m]	Electrode width
Ch_{w}	$100Ch_{\mathrm{h}}$ [m]	Channel width
Ch_{h}	1 [m]	Channel height
Ch_{d}	1 [m]	Channel depth
n	1 []	Chemical constant, number of electrons per atom reacted
R_{const}	8.3144621 [J mol^{-1} K^{-1}]	Gas constant
T_{const}	298.15 [K]	Temperature
F_{const}	96485.3365 [C mol^{-1}]	Faraday constant
V_{app}	5 [mV]	Electrode potential perturbation
f_{max}	1000 [Hz]	Maximum frequency
$x_{\mathrm{diff,min}}$	$\sqrt{D_{\mathrm{Ru2}}/(\pi f_{\mathrm{max}})}$	Maximum diffusion length
A	1 []	Péclet number
B	1 []	Mixed dimensionless number ($E_{\mathrm{w}}/Ch_{\mathrm{h}}$)

C.4.2 Geometry

The geometry is similar as in the previous sections using the parameters given in Table C.5. The difference is that the electrolyte volume was made very wide to make it possible to run $B = 10$. Only an example is therefore given for how the geometry looks, and that is given in Fig. C.5 for $B = 3$.

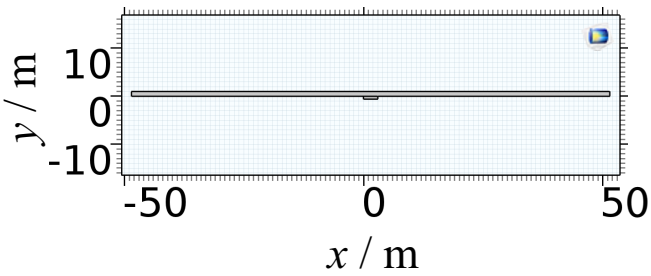

Figure C.5: Geometry for $B = 3$ as an example in this section.

C.4.3 Materials

Similar as previous sections.

C.4.4 Physics setup

Similar as previous sections.

C.4.5 Mesh

A B dependent meshing criteria was made so that when the electrode size was smaller, the meshing at the electrode surface was refined accordingly.

C.4.6 Solver

Similar as previous sections.

C.4.7 Results

Similar as previous sections.

D Comsol documentation for Chapter 8

D.1 Introduction to the numerical solutions

This appendix goes through the numerical solutions found through the use of COMSOL Multiphysics 5.0 [59] using the Batteries & Fuel Cells Module in Chapter 8. The appendix aims to present the reader with the most condensed summary of the calculations making it possible to duplicate the models using only the appendix. The relevant calculations are used to find the results shown in 8.3.

D.2 Fig. 8.3 solution

D.2.1 Solution philosophy

The problem is solved by making a geometry with several electrodes, where only the first electrode have an actual reaction occurring. As Comsol only allows for potential perturbation, a kinetic was designed on this electrode so that a given potential was proportional to the current and the resulting current was scaled to a realistic experimental parameter. This current was then decided to be the pure result of reaction from species 1 to 2 or opposite. The concentration distribution could then be found at different potentials. At the downstream electrodes, no boundary condition different from the wall boundary condition as there is no reaction occurring. Through the concentration relation at the downstream electrodes and the Nernst equation, the potential could be found and the downstream impedance could be defined by using this value.

D.2.2 Input parameters

The input parameters are given in Table D.1.

D.2.3 Geometry

The geometry is built based on the input parameters. In total five electrodes were built where the all electrodes were made as wide as E_{w} and as high as $E_{\mathrm{w}}/5$. The electrodes were placed equally spaced with one E_{w} between them. The first electrode was placed so that the upper left corner of the electrode was at coordinates (0,0), and the other four electrodes were downstream of this electrode. The electrolyte volume was Ch_{w} wide

Table D.1: The input parameters used for all Comsol calculations in this section.

Name	Expression	Description
D_{Ru2}	8.8×10^{-10} [m^2 s^{-1}]	Diffusion coefficient of species 1
D_{Ru3}	5.71×10^{-10} [m^2 s^{-1}]	Diffusion coefficient of species 2
C_{Ru20}	4 [mol m^{-3}]	Initial concentration of species 1
C_{Ru30}	4 [mol m^{-3}]	Initial concentration of species 2
E_{w}	Ch_{h} [m]	Electrode width
Ch_{w}	$20Ch_{\mathrm{h}}$ [m]	Channel width
Ch_{h}	100 [μm]	Channel height
Ch_{d}	1 [mm]	Channel depth
n	1 []	Chemical constant, number of electrons per atom reacted
R_{const}	8.3144621 [J mol^{-1} K^{-1}]	Gas constant
T_{const}	294 [K]	Temperature
F_{const}	96485.3365 [C mol^{-1}]	Faraday constant
V_{app}	$10\sqrt{2}$[V]	Elecrode potential perturbation
f_{max}	1000 [Hz]	Maximum frequency
$x_{\mathrm{diff,min}}$	$\sqrt{D_{\mathrm{Ru2}}/(\pi f_{\mathrm{max}})}$	Maximum diffusion length
$i_{\mathrm{0,start}}$	1 [A m^{-2}]	Limiting current constant
M1	$R_{\mathrm{const}}T_{\mathrm{const}}F_{\mathrm{const}}^{-1}$	Current correction constant
M	0.025693	Dimensionless value of current correction constant

and Ch_{h} high. This was placed so that the midpoint of the channel was at the electrode start, i.e. coordinates (0,0). The geometry build in such a way is given in Fig. D.1.

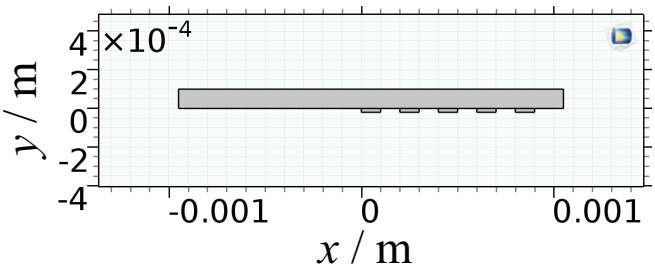

Figure D.1: The geometry built in Comsol for Fig. 8.3.

D.2.4 Materials

The materials set for this calculations are not central to the actual calculations. This is because the parameters that influence the result, i.e. concentrations and diffusion coefficients are set independent of the material in the solution. Therefore, the preset water material in the database was used for the electrolyte volume. The electrolyte volume that was set as water is marked as blue in Fig. D.2.

D.2.5 Physics setup

The physics in Comsol is setup so that a general equation to be solved in the area where the physics is set. In addition, each border of this area needs to have a boundary condition set. The boundary conditions set for this calculation are summarized in Fig. D.2 where each boundary is numbered from 1 to 6, and the area where the physics is valid is marked blue. This is the same area where water is set as the material.

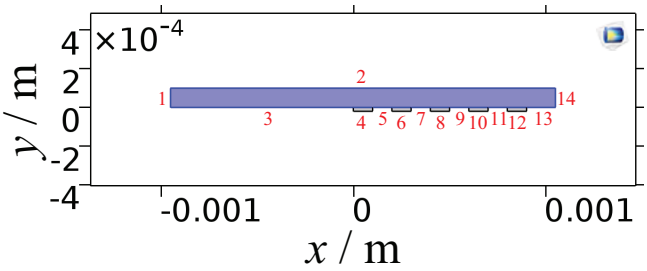

Figure D.2: The physics set to solve in in Comsol for Fig. 8.3. The numbers mark the boundaries, and the set conditions being inlet (1), outlet (14), walls (2,3 and 5-13), and the electrode (4).

The general equations solved in the volume (blue in Fig. D.2) are given in Eq. (D.1)-(D.3).

$$\nabla \cdot (-D_i \nabla c_i) + \mathbf{u} \cdot \nabla c_i = R_i \tag{D.1}$$

$$\mathbf{N}_i = -D_i \nabla c_i + \mathbf{u} c_i \tag{D.2}$$

$$\phi_l = 0 \tag{D.3}$$

Here, D_i is the diffusion coefficient of species i, c_i is the diffusion coefficient of species i, $\boldsymbol{u}$ is the convection, R_i is the total reactions happening in the volume (=1), N_i is the normal flux, and ϕ_l is the electrolyte potential.

Convection is turned on in the setting, and set to be valid in domain 1 as the where the physics is set. The convection is not calculated but stated as Poiseuille flow and given as in Eq. (D.4).

$$V_x = 6V_0 y(Ch_\mathrm{h} - y)/Ch_\mathrm{h}^2 \tag{D.4}$$

The boundary conditions are set at the boundaries, and the first one is the no flux (wall) boundary conditions. This is set on boundaries 2, 3, and 5-13 as in Fig. D.2. The equation giving the no flux is given in Eq. (D.5). The n here is the normal parameter, i.e. that the flux normal to the wall is zero.

$$-\mathbf{n} \cdot \mathbf{N}_i = 0 \tag{D.5}$$

Inflow is set at boundary 1 in Fig. D.2 and the equation governing this is stated below in Eq. (D.6). This is simply a Dirichlet boundary condition stating the concentration at the inlet, and the concentrations used are C_{Ru20} and C_{Ru30} as given in Table D.1.

$$c_i = c_{0i} \tag{D.6}$$

At the outlet at boundary 14 in Fig. D.2, a Neumann boundary condition is stated, where the diffusion flux is set as zero meaning that only convection contributes to mass transport over this boundary. This is stated below in Eq. (D.7).

$$-\mathbf{n} \cdot D_i \nabla c_i = 0 \tag{D.7}$$

The boundary conditions stated so far, the wall, inlet, and outlet are all standard boundary conditions where the equations are not chosen, but set by the type of boundary chosen.

The last boundary condition is at the electrode, boundary 4 in Fig. D.2. This is where all reactions occur in the system influencing the concentration distribution calculated. At this boundary, several equations are valid, starting with the total equations given in Eq. (D.8)-(D.8).

$$i_{\mathrm{total}} = \sum_m i_{\mathrm{loc},m} \tag{D.8}$$

$$-\mathbf{n} \cdot \mathbf{N}_i = R_{i,\mathrm{tot}} \tag{D.9}$$

$$R_{i,\mathrm{tot}} = \sum_m R_{i,m} \tag{D.10}$$

Here, i_{total} is the total current, $i_{\mathrm{loc},m}$ is the local current for each reaction, $R_{i,\mathrm{tot}}$ is the total reaction flux occurring at the electrode, and $R_{i,m}$ is the reaction of step m.

At the electrode, boundary 4 in Fig. D.2, a special type of kinetics is used to create the proportional relation between potential and current making a perturbing current instead of the perturbing potential that Comsol allows to be set. Firstly, the overpotential is defined and set as in Eq. (D.11).

$$\eta = \phi_{\mathrm{s,ext}} - \phi_l - E_{\mathrm{eq}} \tag{D.11}$$

Here, η is the overpotential, $\phi_{\mathrm{s,ext}}$ is the applied (over)potential, ϕ_l is the potential in the electrolyte (= 0), and E_{eq} is the equilibrium potential for the reaction which is set to 0 V.

A linearized Butler-Volmer equation, Eq. (D.12) is used to give the kinetics, but the choice of the equation is relatively arbitrary as the constants are modified to obtain the specific goal of a perturbing current.

$$i_{\mathrm{loc}} = i_0 \Big(\frac{(\alpha_a + \alpha_c)F}{RT} \Big) \eta \tag{D.12}$$

With our definition of $i_0 = i_{0,\text{start}} M/10$, and $\alpha_a = \alpha_c = 0.5$, the reaction occurring turns into $i_{\text{loc}} = k\eta$, where k is a constant that ensures that the proportionality between potential and current is where we want it to be. With the further definition that positive current gives a reaction from $Ru(NH_3)_6^{3+}$ to $Ru(NH_3)_6^{2+}$, and negative current gives the opposite reaction. No other current contributions such as double-layer charging are modeled in this setup.

D.2.6 Mesh

The mesh was a free triangle mesh with in total 504 528 triangular elements and 6556 edge elements. The values in Table D.2 where used to set the meshing parameters, where the values in column "Value, edge" are used for meshing the electrode surface from the first electrode to the end of the second electrode, i.e. boundaries 4-6 in Fig. D.2, and marked as blue in Fig. D.4. The values in column "Value, volume" are used for the rest of the electrolyte volume.

Table D.2: The meshing parameters used to make the mapped mesh used in this section

Description	Value, edge	Value, volume
Maximum element size	$0.1x_{\text{diff,min}}$	$10x_{\text{diff,min}}$
Minimum element size	$0.1x_{\text{diff,min}}$	$0.1x_{\text{diff,min}}$
Curvature factor	0.3	0.25
Maximum element growth rate	1.03	1.05
Custom element size	Custom	Custom

The resulting mesh is shown in Fig. D.3 for the whole volume and in Fig. D.4 for a focus on the mesh at the electrode surface.

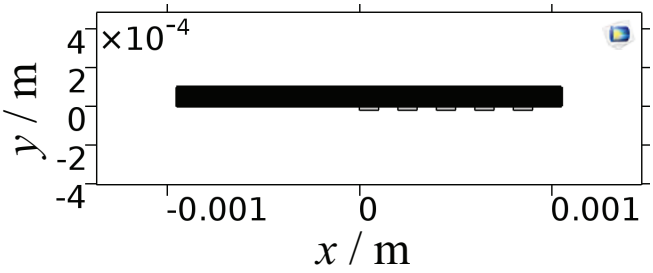

Figure D.3: The mesh for the whole volume built in Comsol.

D.2.7 Solver

The problem is solved by doing a parametric study for the flow rates relevant in our case, i.e. from 10 μL min^{-1} to 300 μL min^{-1}, and for a wide range of frequencies from 10^{-4} Hz to 10^7 Hz. This was solved in a sequence where first the steady-state solution was

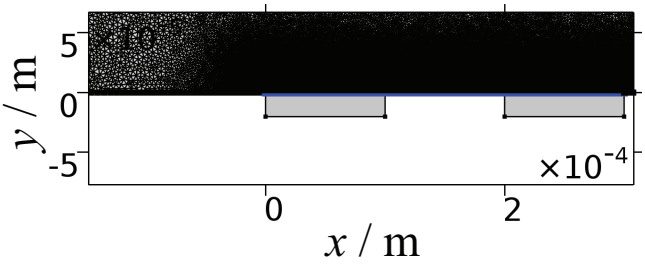

Figure D.4: Focus on the mesh at the electrode surface used in this section.

done, and then the frequency was applied on top of this steady-state solution giving the individual frequency solutions. The solver is used in the volume that is marked blue in Fig. D.2.

The steady-state solution was found using a stationary solver solving for the variable C_{Ru2} and $\mathrm{C}_{\mathrm{Ru3}}$. A fully coupled direct solver was used and the initial damping factor was set to 0.01, the maximum damping factor was set to 10^{-6}, and the maximum number of iterations was set to 50. The PARDISO solver was used for this problem. The same type of solver and parameters was used for the frequency dependent problem, and the complex numbers were treated directly as such.

D.2.8 Results

The resulting impedance for each flow rate is found from an integration procedure for each frequency. In the case of downstream impedance, first, the current perturbation was found at electrode 1, boundary 4 in Fig. D.2. This is found from the maximum current, and was for all cases equal to $\sqrt{2} \times 10^{-7}$ A when integrated and taken over the whole "volume", i.e. multiplied by the channel depth, Ch_{d}. The potential perturbation was found by integrating the Nernst equation on the downstream electrode, and this is given in Eq. (D.13).

$$\widetilde{E}_{\mathrm{SE}} = \frac{RT}{F}\frac{\widetilde{c}_{\mathrm{Ru^{III}}}}{c_{\mathrm{Ru^{III},ss}}} - \frac{RT}{F}\frac{\widetilde{c}_{\mathrm{Ru^{II}}}}{c_{\mathrm{Ru^{II},ss}}} \tag{D.13}$$

This assumed that $C_{\mathrm{Ru20}} = C_{\mathrm{Ru30}} = 1$, and resulted in a complex potential at the electrode which could then be used to find the impedance after $Z = \widetilde{E}_{\mathrm{SE}}/\widetilde{I}_{\mathrm{WE}}$. And after some normalization, the values found could be compared with the experimental data as in Fig. 8.3.